N-63-4-3

410547

PLASMA PROPERTIES IN THE PLUME OF SOLID-PROPELLANT MOTORS CONTAINING CsNO3 AND KNO3

Prepared by

K. Baldwin
J. Eckerman
R. Williamson
R. Buck

RESEARCH AND ADVANCED DEVELOPMENT DIVISION
AVCO CORPORATION
Wilmington, Massachusetts

Technical Memorandum

RAD-TM-63-14

Contract AF04(694)-239

15 July 1963

Prepared for

AIR FORCE BALLISTIC SYSTEMS DIVISION
AIR FORCE SYSTEMS COMMAND
UNITED STATES AIR FORCE
Norton Air Force Base, California

PLASMA PROPERTIES IN THE PLUME OF
SOLID-PROPELLANT MOTORS
CONTAINING CsNO3 AND KNO3

Prepared by

K. Baldwin
J. Eckerman
R. Williamson
R. Buck

RESEARCH AND ADVANCED DEVELOPMENT DIVISION
AVCO CORPORATION
Wilmington, Massachusetts

Technical Memorandum

RAD-TM-63-14

Contract AF04(694)-239

15 July 1963
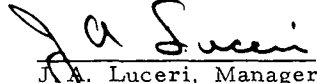
APPROVED

L. N. Smithline, Project Engineer
Mark 6, Mod 2 Decoy

J. A. Luceri, Manager
REST Project Office

Prepared for

AIR FORCE BALLISTIC SYSTEMS DIVISION
AIR FORCE SYSTEMS COMMAND
UNITED STATES AIR FORCE
Norton Air Force Base, California

ABSTRACT

Three series of tests were conducted at the Naval Research Laboratory high-altitude chamber to meausre the performance of $Al:CsNO_3$ and $Al:KNO_3$ solid-propellant rocket motors. Motor operating parameters were measured. The plume was probed with a microwave system to measure the electron density at an ambient pressure of 1 torr. The plume electron density profile as a function of radius and the recombination rate as a function of radius were determined. Electron densities of the order of 10^{12} cm^3 and recombination rates of the order of 10^{-8} cm^3 sec^{-1} were measured.

CONTENTS

ILLUSTRATIONS

ILLUSTRATIONS (Cont'd)

ILLUSTRATIONS (Cont'd)

TABLES

ACKNOWLEDGMENTS

I. INTRODUCTION

This report describes the operating characteristics of solid-propellant rocket motors using $Al:CsNO_3$ and $Al:KNO_3$ as the fuel. Three series of tests were conducted in a high-altitude chamber at the Naval Research Laboratory, Washington, D. C., during December 1961, June 1962, and July 1962. These tests were conducted for the purpose of evaluating the motor operation and the plume characteristics. The following objectives were investigated:

1. **Motor Operation at High Altitude**

    a. Test ignition reliability

    b. Observe smothness of burning

    c. Observe slagging and nozzle erosion

    d. Determine effect of grain binder on plume

    e. Measure thrust

    f. Measure weight of fuel consumed

    g. Measure burning time of motor.

2. **Plume Properties at High Altitude**

    a. Measure spatial electron-density distribution

    b. Measure electron-density recombination rate

    c. Record optical spectra

    d. Photograph plume configuration

    e. Determine particle size, composition, and emissivity of solids in plume

    f. Determine spatial distribution of particles in plume.

Motors for each of the three series of tests differed as engineering changes were made in the fuel and nozzle design. A large number of measuring techniques were utilized in an effort to gather as much information as possible. Not all were successful and some were abandoned. Other measurements were of particular value and were continued. A list of tests performed in each series is contained in table I.

TABLE I

TABLE OF TESTS

Test Item	Series I	Series II	Series III
Motor Type	6-$CsNO_3$ - No binder	3-$CsNO_3$ - No binder 6-$CsNO_3$ - binder 3-KNO_3 - binder	8-$CsNO_3$ - binder 11 KNO_3 - binder
Ambient Pressure	1 torr	1 torr	1 torr 20 torr 100 torr
Motor Pressure	90 psi	300 psi (Cs) 150 psi (K)	150 psi (both types)
Thrust	Yes	Yes	No
Microwaves	35 gc	35 gc 70 gc	23.5 gc
Transmission	Yes	Yes	Yes
Reflection	No	Yes	Yes
Oscillating Plume	No	No	Yes
Spectrograph	Yes	Yes	Yes
Drop Pendulum	No	Yes	Yes
Hi Speed Movies	No	Yes	Yes
IR Movies	Yes	Yes	Yes
UV Movies	Yes	No	No
Stereo Movies	No	Yes	No
Color Movies	Yes	Yes	Yes
Wire Grid	No	Yes	Yes
Particle Collectors	No	Yes	Yes
Optical Pyrometer	No	Yes	Yes

II. DESCRIPTION OF TEST FACILITY AND INSTRUMENTATION

The test chamber consists of a 10 by 6 by 7 foot stainless steel, high-altitude room. This room is connected to a steam ejector pump which can maintain a lower pressure of 1.0 torr. Pumping time is of the order of 5 minutes from atmospheric pressure to the lower limit. Except during motor ignition, the ambient pressure was maintained during motor firings.

Ambient chamber pressure is measured at the end of the chamber to one side of the exhaust vent in such a manner that the motor plume does not interfere with the measurement. Data are recorded continuously via a Statham 0 to 2-psi electrical transducer. The transducer is calibrated against a mercury manometer prior to the tests. Accuracy is approximately ± 0.1 torr.

Motor pressure is monitored via an electrical transducer connected to the pressure tap in the motor. An oil trap protects the guage from the hot gases. The gauge is calibrated against pressure gauge readings from a compressed nitrogen bottle. Accuracy is approximately ± 5 psi.

The rocket motor during the first two test series was mounted on a thrust-table at one end of the chamber (figure 1). The thrust-guage is an electrical transducer which is calibrated against weights with an estimated error of less than 1 pound. The thrust table is not critically damped, hence transients cause a certain amount of oscillation which damps within 1 second.

Mounted in the chamber is a rack for mechanically scanning focused microwave horns (figure 2), both axially and normal to the axis. The microwave horns scan axially at a rate of 1.0 in./sec and perpendicular to the axis at a rate of 0.5 in./sec. Figure 3 shows the traversing system. The low scanning speed of this system prevented obtaining complete data during the first two series. In order to obtain complete and redundant microwave data across the plume diameter, the rocket motor was mounted on an oscillating stand for the third test series. This stand consisted of a brass pipe,large enough to contain the motor, pivoted at one end and connected by a connecting rod to an electric-motor-driven eccentric. The rocket motor was thereby oscillated in a vertical plane through an angle of approximately 20 degrees. The period was of the order of 7 seconds. A microswitch connecting a timing mark to the recorder was closed once each cycle to permit correlating recording time with motor position. Because of this motor mount, thrust data were not obtained during this series. With this arrangement, the horns were located at a known distance from the motor and the plume moved past the horns. Figure 4 shows the motor oscillator.

Figure 1 ROCKET MOTOR MOUNTED ON THRUST TABLE IN HIGH-ALTITUDE CHAMBER
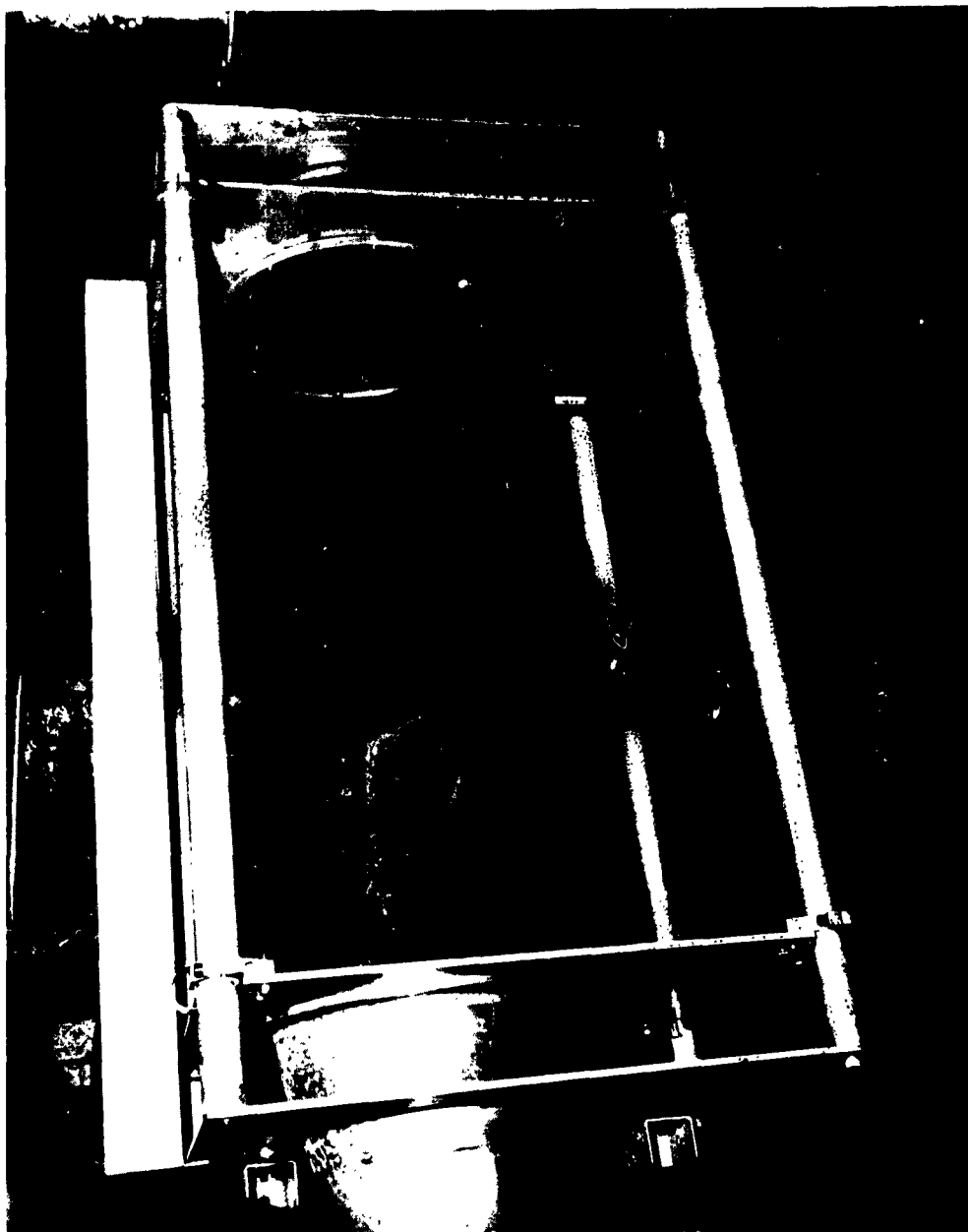
Figure 2 FOCUSED MICROWAVE HORNS FOR SCANNING PLUME

Figure 3 TRAVERSING SYSTEM FOR MICROWAVE HORNS
(Motor plume exhausts into exhaust baffle at
end of chamber. Optical Ports are
recessed in wall.)
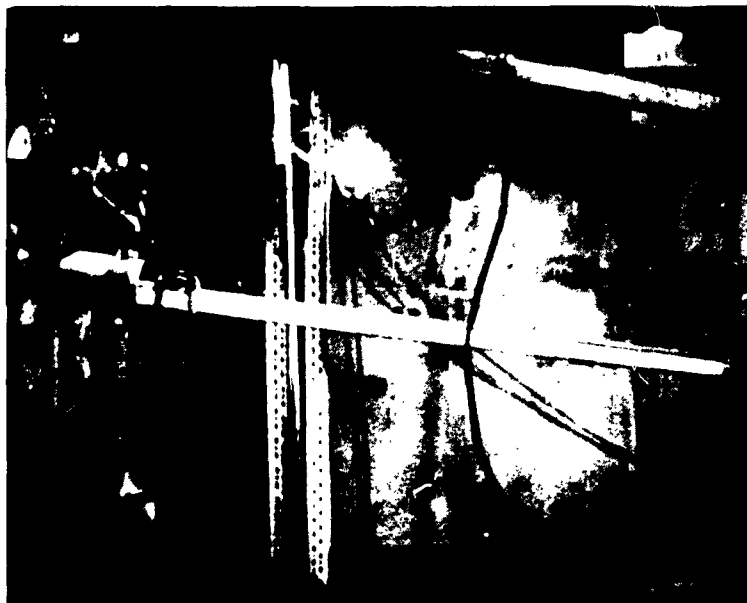
Figure 4 MOTOR OSCILLATOR IN HIGH-ALTITUDE CHAMBER
(Stadia rod permits calibration of
axial distance in plume.)

During the first test series, the microwave frequency utilized was 35 gc. However, frequency instability due to thermal drift, plus a desire to utilize as high a microwave frequency as possible, led to the use of 70 gc for the second test series. This system was even more unstable than the 35 gc system. Hence, for the third series, 23.5 gc was utilized, since it was known to be extremely stable.

The microwave system consisted of a klystron transmitting through a focused horn to a focused horn receiving antenna which was connected to a video detector. The klystron was modulated with a 1000 cps square wave. Adequate attenuation was included in the transmission line to prevent frequency pulling of the klystron. A 20-db directional coupler was used to sample the reflected power level. The output of the video detector was filtered to remove 60 cps hum plus other noise which may have been picked up. The output of the 1000 cps filter was rectified and the dc output was recorded. A similar system was used for the reflected signal. Calibration was achieved via a precision attenuator in the klyston-antenna line. The circuit is shown in figure 5. The focusing lenses were made of polystyrene and have a focal spot diameter of the order of 1.5λ. The complete microwave system was mounted in a pressurized container on the scanning rack, thereby permitting the necessary high voltages to be fed in at atmospheric pressure. The horns and lens system operated at ambient chamber pressure to avoid defocusing due to pressure distortion of the lens.

The recording system used for all data was a Midwest Industries recorder which utilizes a galvanometer-mirror combination for each channel to produce a trace on light-sensitive paper. The frequency response of the system is 40 cps for the galvanometers used. Because the recorded traces cannot be easily reproduced without special chemical treatment of the paper, in series II and series III a Sanborn recorder was used to record the microwave data.

A drop pendulum was used to obtain samples of solids in the plume. It was pivoted from the floor and raised to one side of the motor. It can be seen in the background of figure 4. Before the run, it was raised and latched in place with an electromagnet. During the run, the electro-magnet was turned off, releasing the pendulum to fall through the motor plume. Special collectors and microscope slides attached to the pendulum were used to collect the solid material in the plume.

In addition to the collectors fastened to the pendulum, a stainless-steel pipe elbow, closed at one end, was fastened to the exhaust vent at the rear of the chamber to collect additional material for analysis. An annealed copper deflector was placed in the pipe to examine particle impact pits.
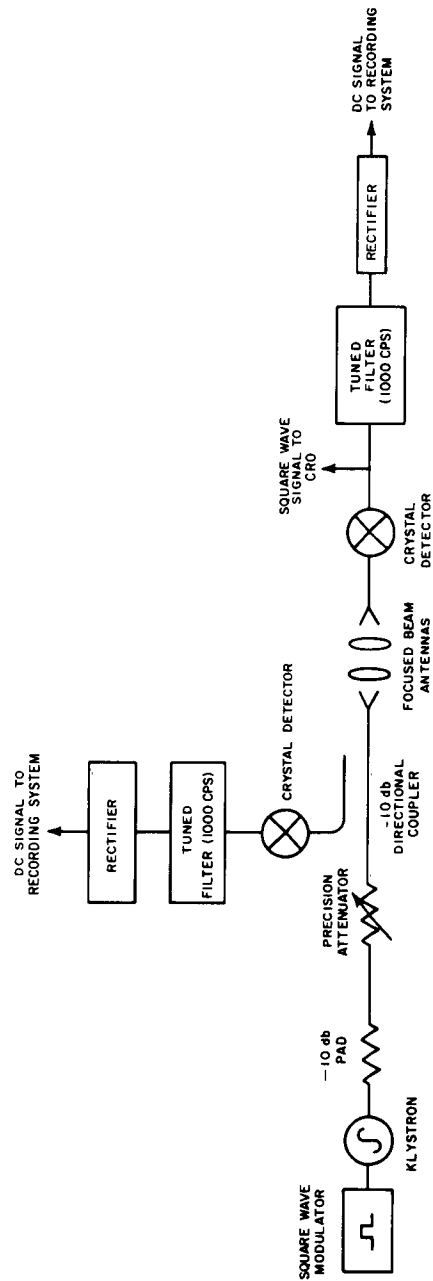
Figure 5 DIAGRAM OF MICROWAVE-FOCUSED BEAM SYSTEM
62-5779

Ports in the side of the chamber permitted observation of the plume with motion picture cameras, still cameras and spectrographs. On the first tests, movies were taken in three spectral ranges (figure 6). The second series used stereo movies, infrared movies (which show more shock structure detail), and high-speed movies (400 frames/sec). Only infrared and high speed movies were used on the third series. Color movies were taken on all tests. In addition, speed-graphic cameras were used to obtain both black and white and color stills. Camera ports can be seen in the background of figure 3.

Four different spectrographs were employed during the various tests. A crude laboratory unit was used during the first series. During the second series, a Bausch and Lomb medium quartz spectrograph was used together with a Jarrell-Ash scanning spectrometer. The third series utilized primarily a laboratory, grating spectrograph of much greater resolution and dispersion than those used before. A typical setup is shown in figure 7.

A manually adjusted optical pyrometer of the color matching type (Pyrometer Instrument Co.) was used during the last two series in an effort to measure temperature in the plume. It was focused on the core of the plume about 1 inch from the nozzle.

Wire grids were placed adjacent to the motor nozzle to study plume expansion on a few runs in the second and third test series. The gas flow impinging on the wires heats them to incandescence, thereby marking the plume contour. Copper grids were used in the second series, and an alternating wire weave of tungsten and molybdenum was used in the third series.

All of the motors tested at NRL were developmental models and were not identically the same from series to series. The general configuration is shown in figure 8. The casings for these test motors were made of heavy steel in order to provide a margin of safety in case of explosion. The design was such that should a runaway condition develop, the excess pressure would shear the nozzle out of its mounting and thereby provide a safety pressure release. The heavy wall ensured that fragmentation would not occur prior to nozzle failure. Table II lists the composition of the grains for the various series. The most important distinction in the latter two series was the addition of an organic binder to the grain which improved smoothness of the burning, reduced the amount of slagging, and prevented internal fractures of the grain which could lead to detonation. The grains were fabricated in two sections and sealed together. A total of 37 motors were fired in the three series.
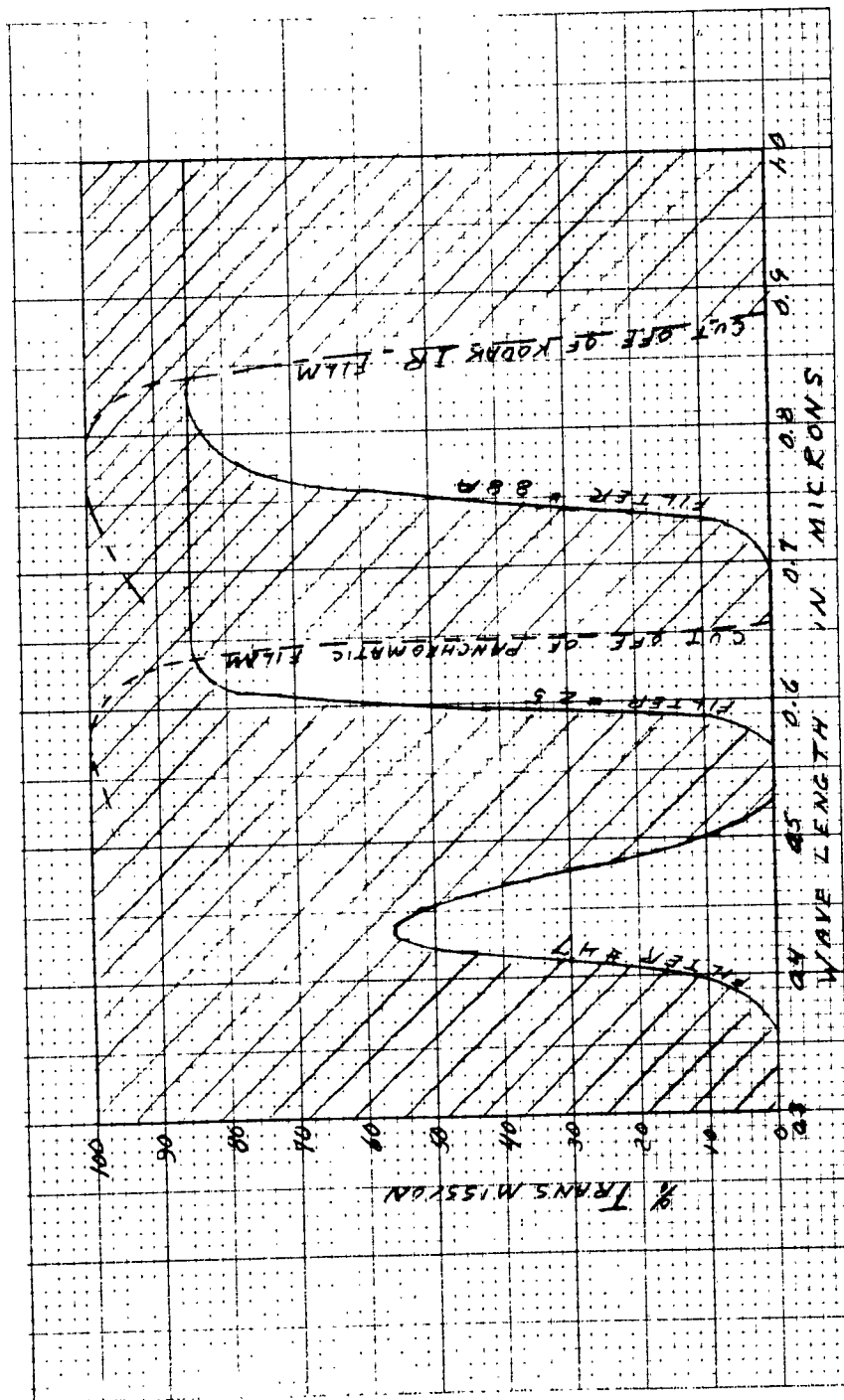
Figure 6 SPECTRAL SENSITIVITY OF 35 MM MOVIE CAMERAS USED IN SERIES I
63-953
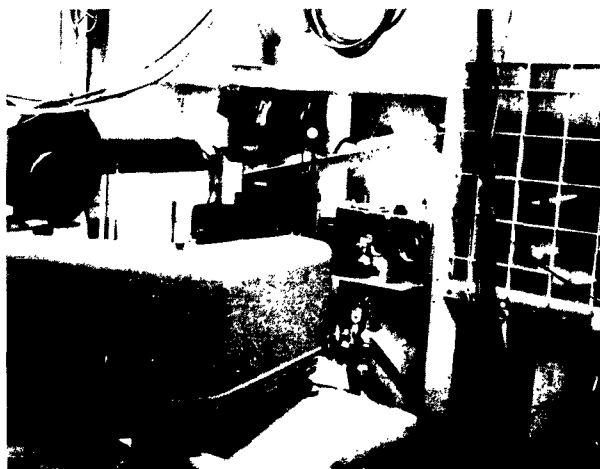
Figure 7 TYPICAL OPTICAL INSTRUMENTATION
In the foreground, a Bausch and Lomb Medium
Quartz Spectrograph shares image via reflecting
plate with Jarrell-Ashc Spectrometer (extreme
right). At upper ports (left to right) Speed
Graphic-color movies; lower ports (left to right)
high-speed B&W movies (400 fps); I. R. Movies;
Speed Graphic; reflecting plate for spectrographs.
63-954
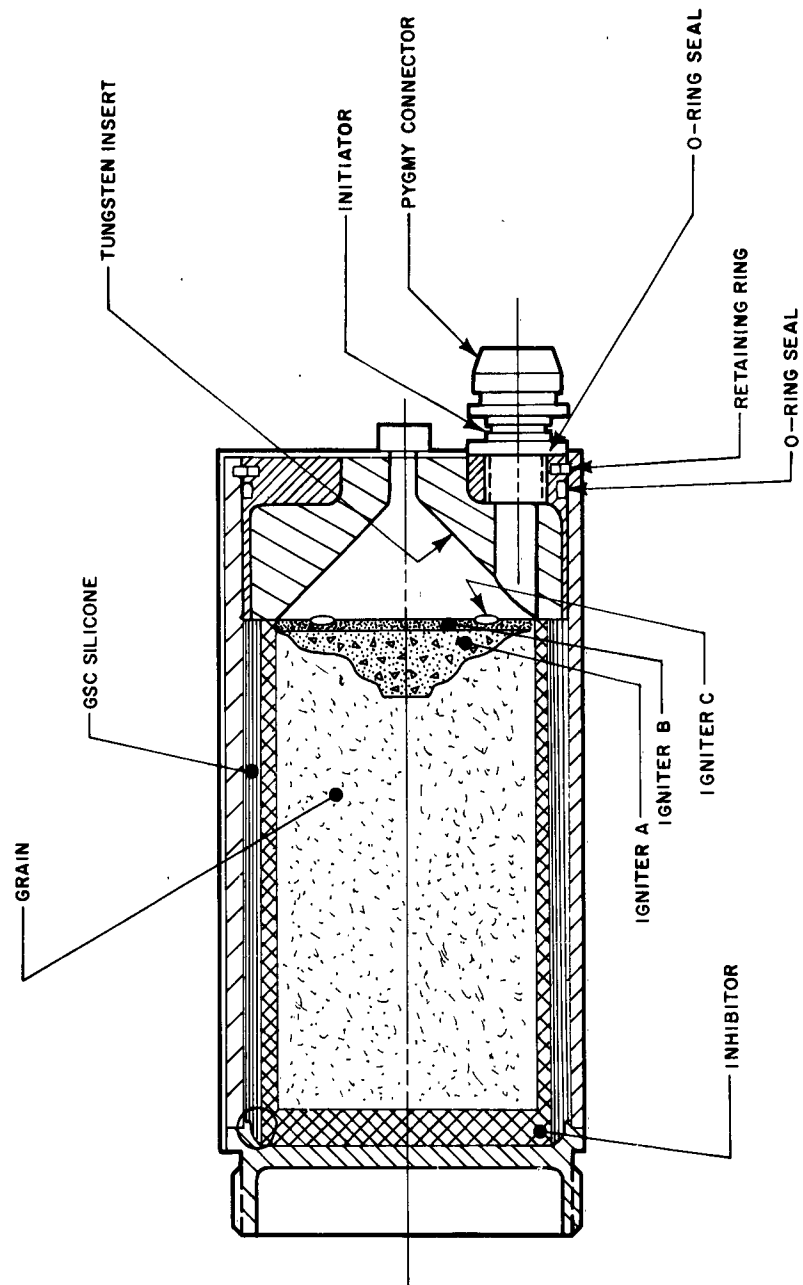
Figure 8 CROSS SECTION OF MOTOR CONFIGURATION
63-955

Labels on figure:

TUNGSTEN INSERT
INITIATOR
PYGMY CONNECTOR
O-RING SEAL
RETAINING RING
O-RING SEAL
GSC SILICONE
IGNITER A
IGNITER B
IGNITER C
GRAIN
INHIBITOR

TABLE II

SPECIFICATION OF MOTOR UNITS

	Grain Formulation			Test Series
1.	$CsNO_3$ Aluminum 50/50 Mg/Al alloy Lampblack	75 percent weight 22 percent weight 2 percent weight 1 percent weight		I, II
	Consolidation pressure Grain length Grain diameter	20,000 psi 3.72 inch 2.01 inch		
2.	$CsNO_3$ Aluminum Mg/Al alloy (65/35) Lampblack Binder	75 percent weight 22.5 percent weight 2.0 percent weight 0.5 percent weight 1.0 percent (of total)	total	II, III
	Consolidation pressure Grain length Grain diameter	28,800 psi 3.76 inch 2.02 inch		

3.	KNO_3
	Aluminum
	Binder
	    Laminac 4116
	    Pluronic
	    Lupersol DDM
		60 percent weight
		40 percent weight
		5 percent (of total)
			total	II, III

	Consolidation pressure Grain length Grain diameter	30,300 psi 3.80 inch 2.02 inch		

III. TEST RESULTS

A. IGNITION

Although the grains, nozzles, and operating characteristics of the motors
varied from series to series, the initiators were all of similar design (figure
9). They consist of a small unit which screws into the front of the motor and
connects via a hole to the burning chamber. The units were ignited with a 24-
volt dc source. Two types of failures were encountered: 1) in some cases,
the initiator failed to fire (no pressure pulse was observed in the burning cham-
ber); 2) and more commonly, a pressure pulse from the initiator was observed
followed by a failure of the motor to sustain burning. This latter failure re-
sulted in grain surface roughening, indicating that a small amount of burning
had taken place.

During the first series, no ignition failures were experienced. In the second
series, two failures of the second type (above) occurred involving $CsNO_3$ mo-
tors without binder. In the third series, one failure of the first type and two
of the second type were encountered. These two failures in the third series,
where initial burning was established, involved KNO_3 units which had been
stored in outdoor bunkers from the time of the second series (approximately 1
month). The temperature in these bunkers rises above the out-of-doors tem-
perature, which during the summer months may well have been in excees of
100° F. It is quite possible that there is an aging effect which leads to failure.
In support of this possibility is the experience that solid-propellant motors
of other types have been known to exhibit aging effects.

B. MOTOR PRESSURE

Following ignition, a rapid buildup of pressure occurred. Typically, the peak
pressure reached 2 to 4 times the average pressure and then subsided within
1. 5 to 2. 0 seconds to the operating value. • The pressure buildup is associated
with the burning of the ignitor which is pressed into the main body of the grain
(figure 8). Considerably more gas is evolved from this mixture than from the
nitrate mixtures. Average pressure traces for all motor types are shown in
figures 10 to 14. A very low average pressure of the order of 90 psi was ob-
tained during the first series. Photographic evidence indicates that erratic
burning plus sporadic nozzle blockage (due to slag buildup) caused severe
transient fluctuations in motor pressure which the transducer was unable to
follow.

In the second series, the potassium motors operated at about 150 psi average
pressure, but the cesium motors operated at about twice this value. The burn-
ing time was correspondingly short in the latter case. The high pressure re-
sulted from the fact that the nozzle orifice was somewhat undersized and did not

erode as much as anticipated. The pressure dip midway through the KNO_3 motor run in series II is due to the interface between the two-segment grain. This was overcome in series III as evidenced in figure 14.

Average pressures of the order of 150 psi were recorded for the third series for both types of motors. Examination of the cesium motor pressure traces shows that in all three series a generally declining pressure occurs, as contrasted with the relatively uniform average operating pressure exhibited by the potassium motors. This is undoubtedly due to the greater chemical activity of cesium which erodes the nozzle orifice more, thereby reducing the pressure.

An interesting failure occurred in motor 31. The plume exhibited violent pressure fluctuations (figure 15) which the transducer could not follow. The motor extinguished after 3.5 seconds. Figure 16 is a photograph of the remaining grain. Apparently, burning between the grain and the inhibitor increased the burning area, hence the motor pressure increased, finally resulting in nozzle failure.

Examination of high-speed motion picture data gives a qualitative idea of the burning characteristics of the grains. In general, addition of binder tended to improve burning characteristics; i.e., it reduced plume fluctuations. This is true for both cesium and potassium grains. Since drastically changed plume geometry was observed to occur within two successive frames of the high-speed data (400 frames/sec), this represents severe fluctuations with a periodicity of less than 2.5 msec--far too fast for the pen recorder to follow. The most violent of these fluctuations occurred with the $CsNO_3$ without binder. A double image appears in the low-speed movie frame as a result of this type of fluctuation (figure 17). Addition of 1 percent ethocell considerably reduced the fluctuation in the $CsNO_3$ plumes. In general, the KNO_3 motors appeared far smoother in operation with 5 percent binder.

C. MOTOR THRUST

Thrust data was obtained only during the first two series, the thrust table being eliminated in the third series in favor of the motor rocker. During the initial buildup of pressure, severe oscillations occurred in thrust due to the thrust table being underdamped. Figures 18, 19, and 20 are traces showing average thrust for the first two test series. The nozzles were designed to produce a minimum thrust. The higher motor pressure achieved in the series II $CsNO_3$ (binder) motors resulted in a shorter burning time and greater thrust. Figure 21 is a plot of average thrust versus mass flow-rate for motors in the first and second test series. Based on these data points, the predicted thrust for the motors of the third series has been placed on the graph. These values presuppose a constant exit velocity at the nozzle which is true within the limits of accuracy, imposed by taking average values for both thrust and mass flow rate.
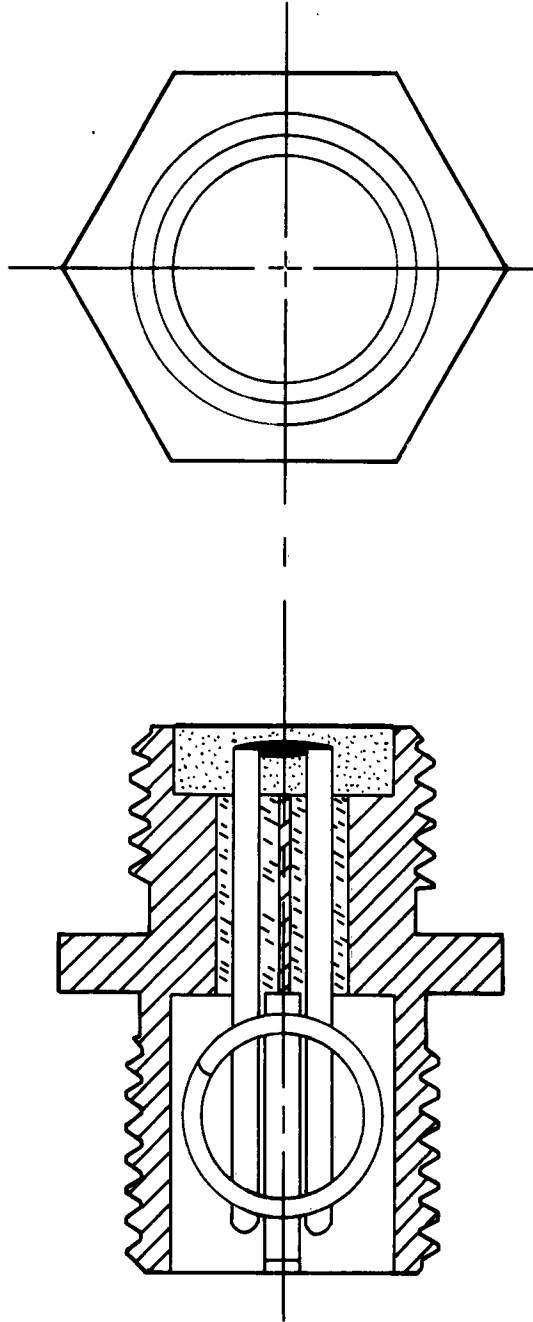
Figure 9 INITIATOR ASSEMBLY
63-2785
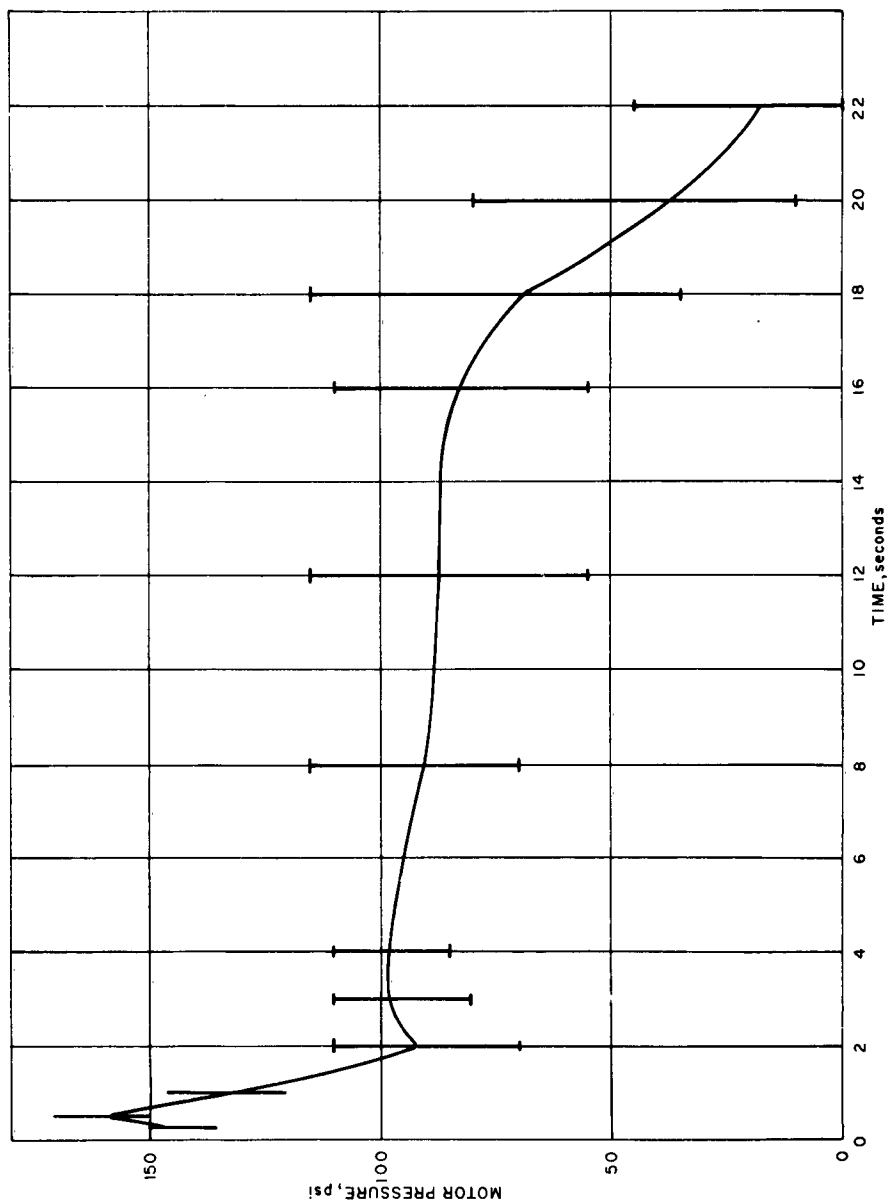
Figure 10 MOTOR PRESSURE VERSUS BURNING TIME, Al: $CsNO_3$
(SERIES I)
63-2784
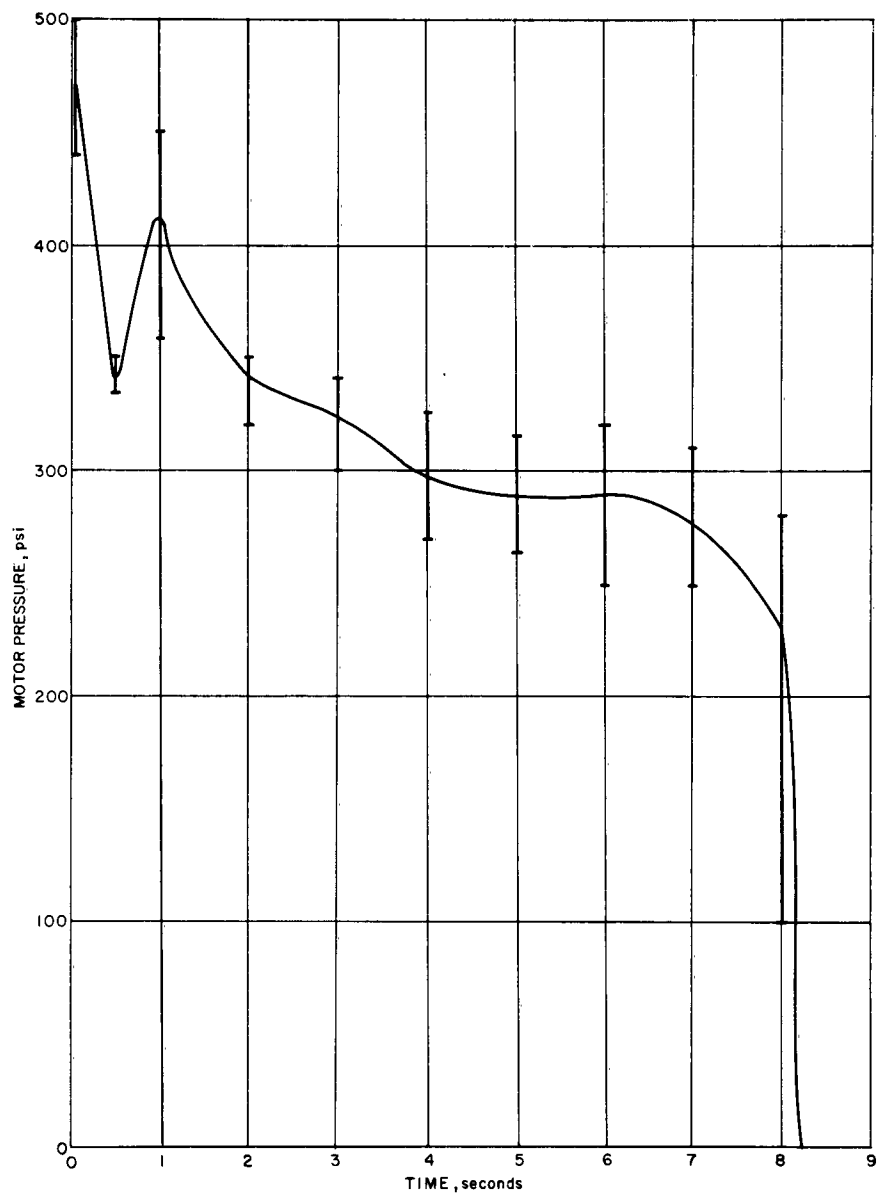
Figure 11 MOTOR PRESSURE VERSUS BURNING TIME, Al: $CsNO_3$
(SERIES II)
63-2783
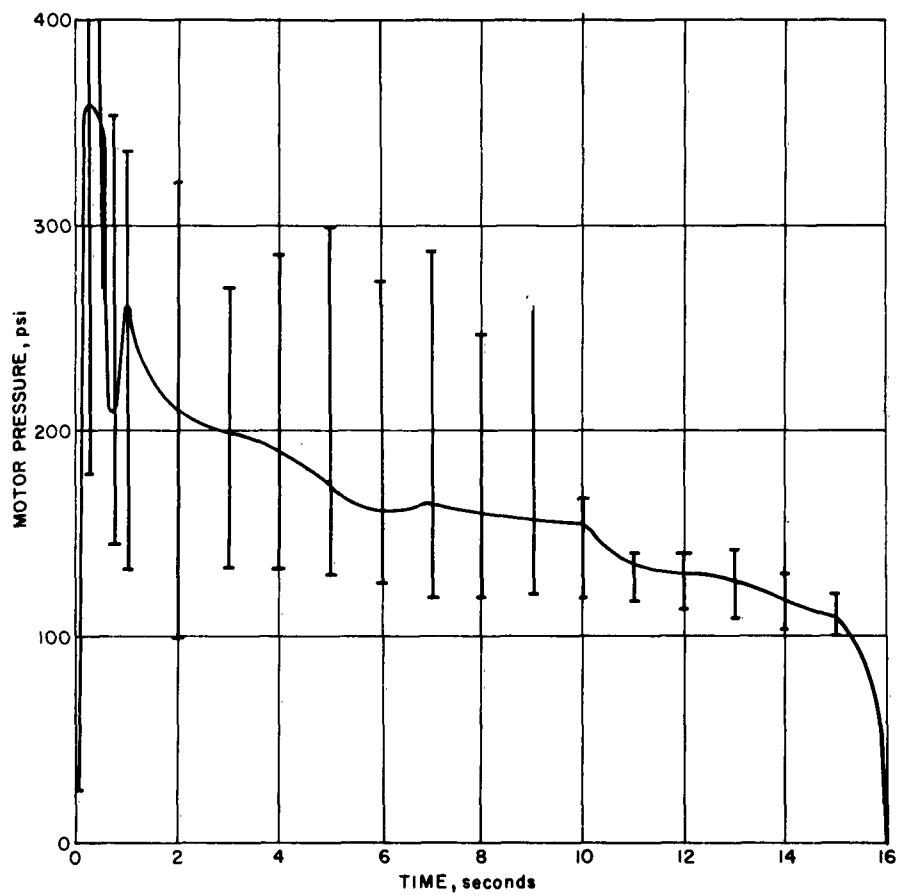
Figure 12 MOTOR PRESSURE VERSUS BURNING TIME, Al: CsNO$_3$
(SERIES III)
63-2782
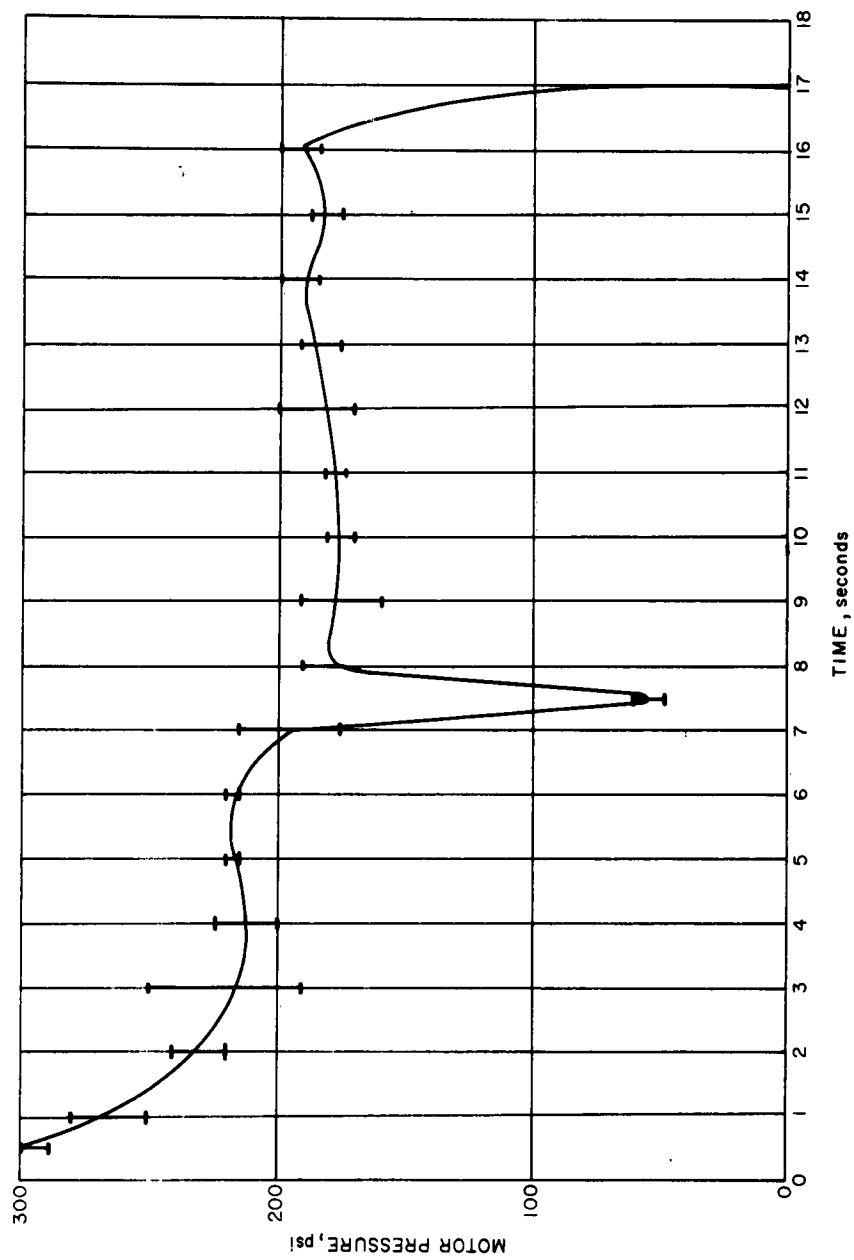
Figure 13 MOTOR PRESSURE VERSUS BURNING TIME, A1: KNO_3
(SERIES II)
63-2787

TIME , seconds
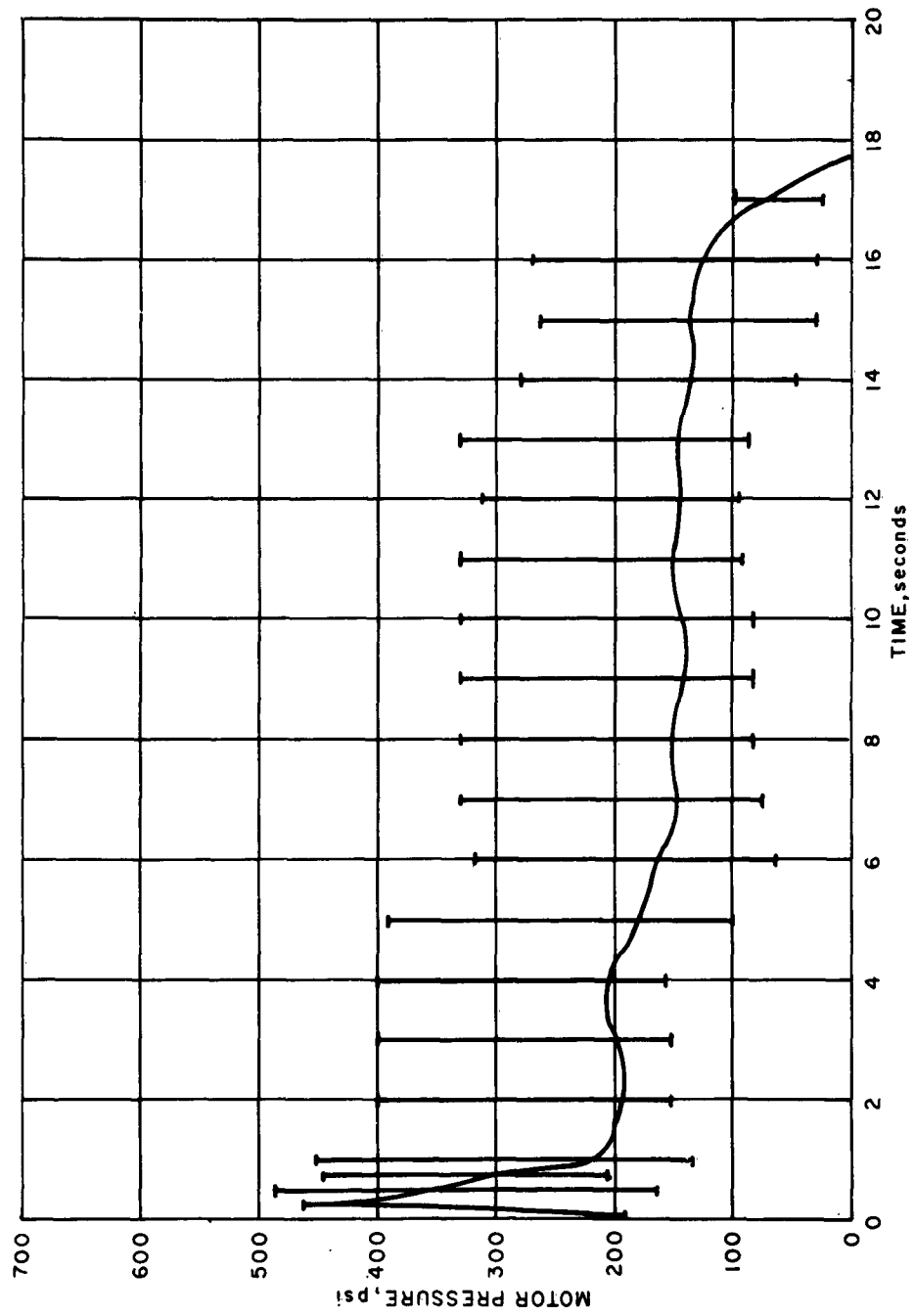
MOTOR PRESSURE, psi

Figure 14 MOTOR PRESSURE VERSUS BURNING TIME, Al: KNO_3
(SERIES III)
63-2780
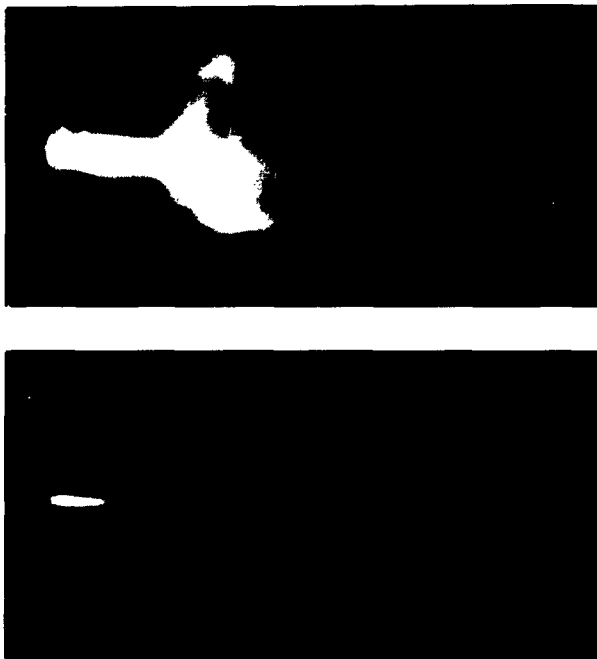
Figure 15 DRASTIC CHANGE IN PLUME CONFIGURATION WITHIN PERIODS OF
0. 1 SECONDS, DUE TO VIOLENT MOTOR PRESSURE FLUCTUATIONS
(This cycle was repeated several times before motor was
extinguished after 3. 5 seconds of operation.)
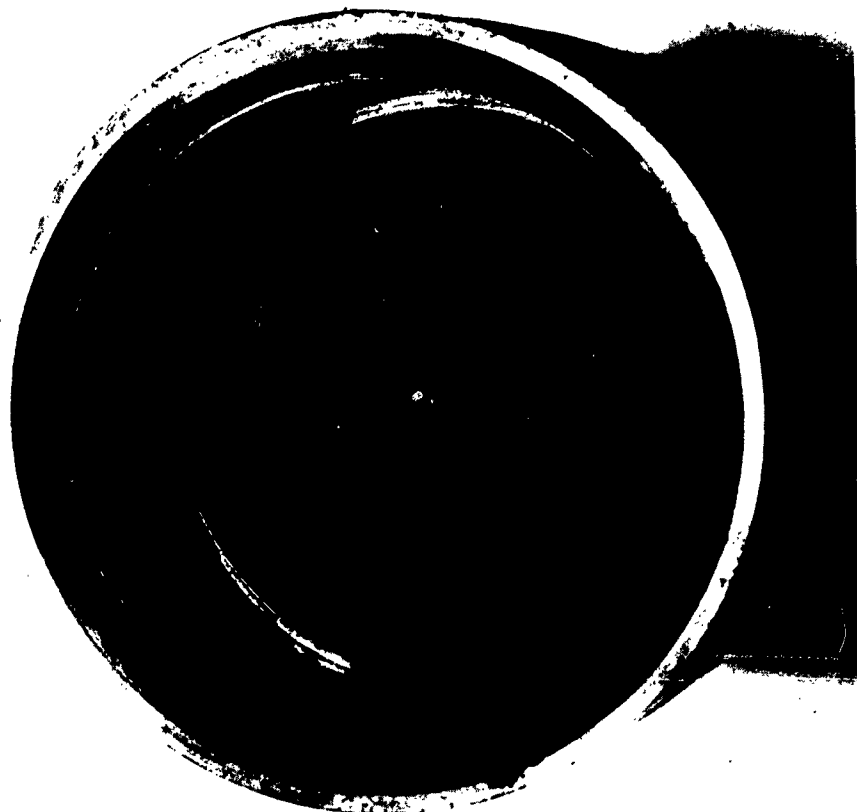
Figure 16 VIEW OF PARTIALLY BURNED GRAIN
(Grain burned along inhibitor, causing an
overpressure resulting in
nozzle failure.)
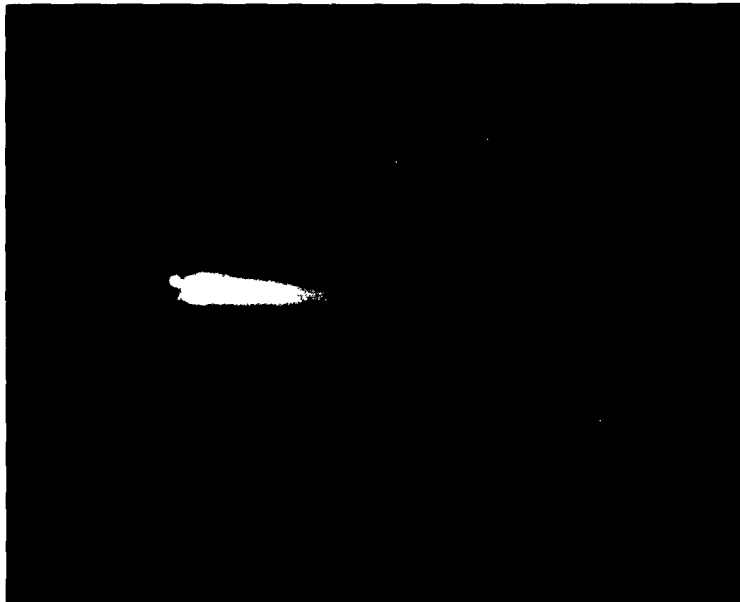
Figure 17 DOUBLE IMAGE OF PLUME SHOCK STRUCTURE
(Resulted from erratic burning of Al: CsNO₃ motor
without binder. This frame exposure was
approximately 0.01 seconds.)
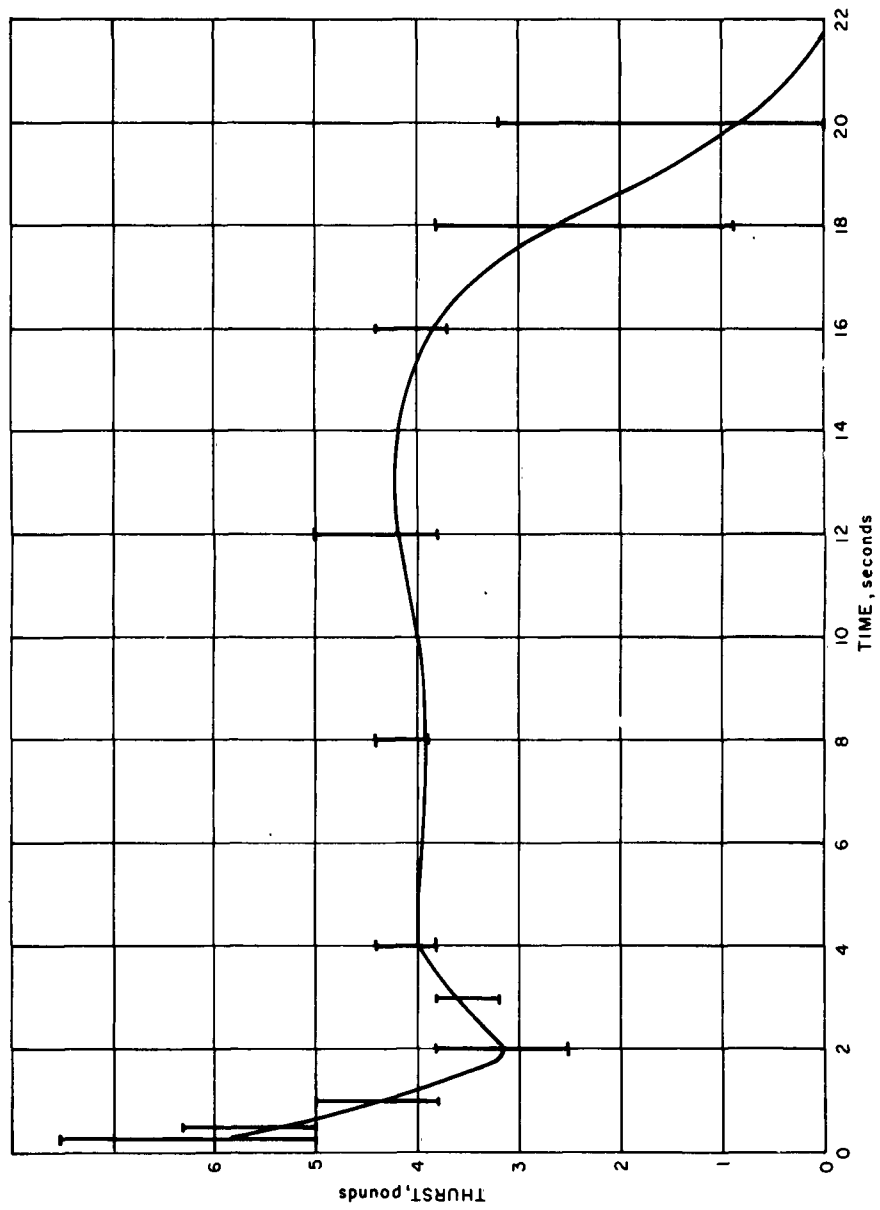
Figure 18 MOTOR THRUST VERSUS BURNING TIME, Al: CsNO$_3$
(SERIES I)
63-2779

THRUST, pounds

TIME, seconds

30 20 15 10 5 0

0 1 2 3 4 5 6 7 8 9
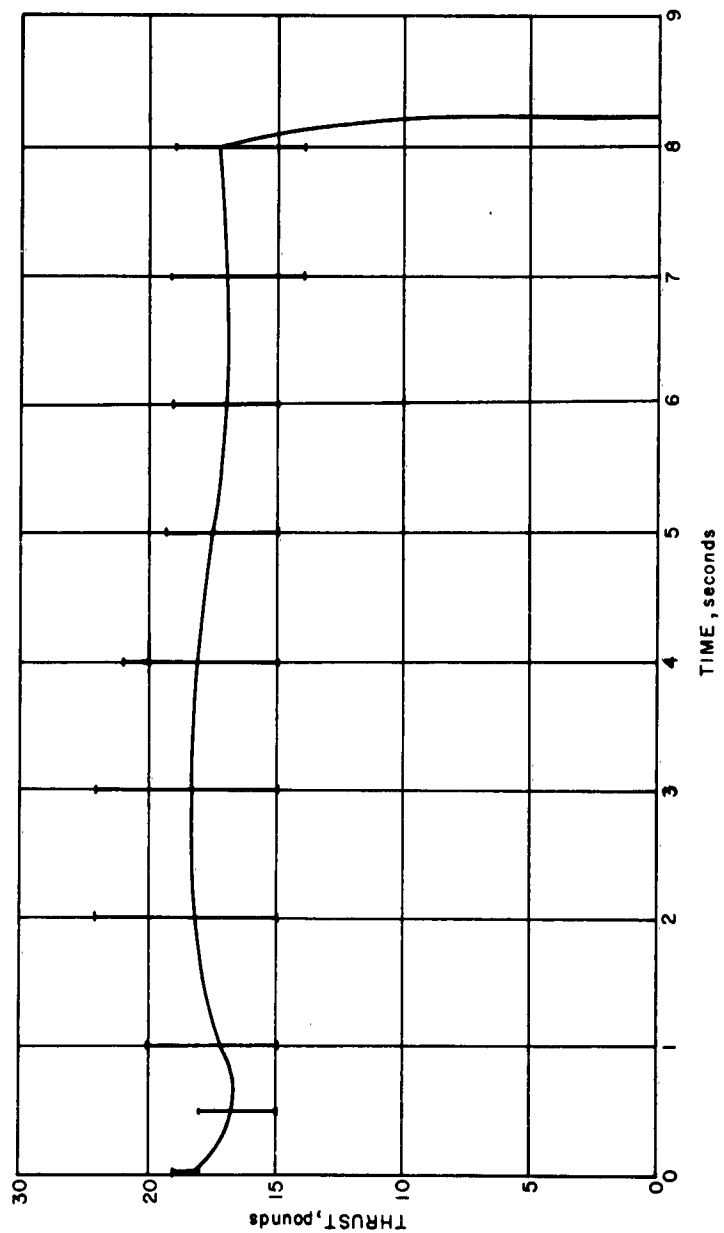
Figure 19 MOTOR THRUST VERSUS BURNING TIME, Al: $CsNO_3$

(SERIES II)

63-2778

-27-
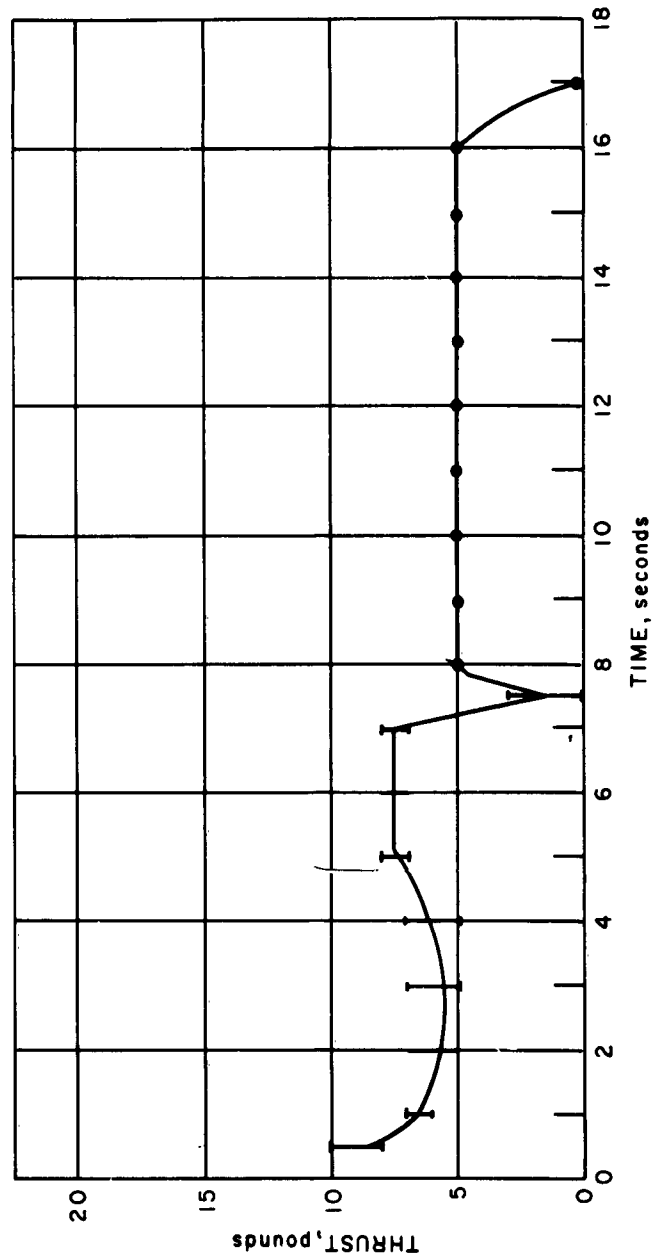
Figure 20 MOTOR THRUST VERSUS BURNING TIME, A1: KNO_3
(SERIES II)
63-2777
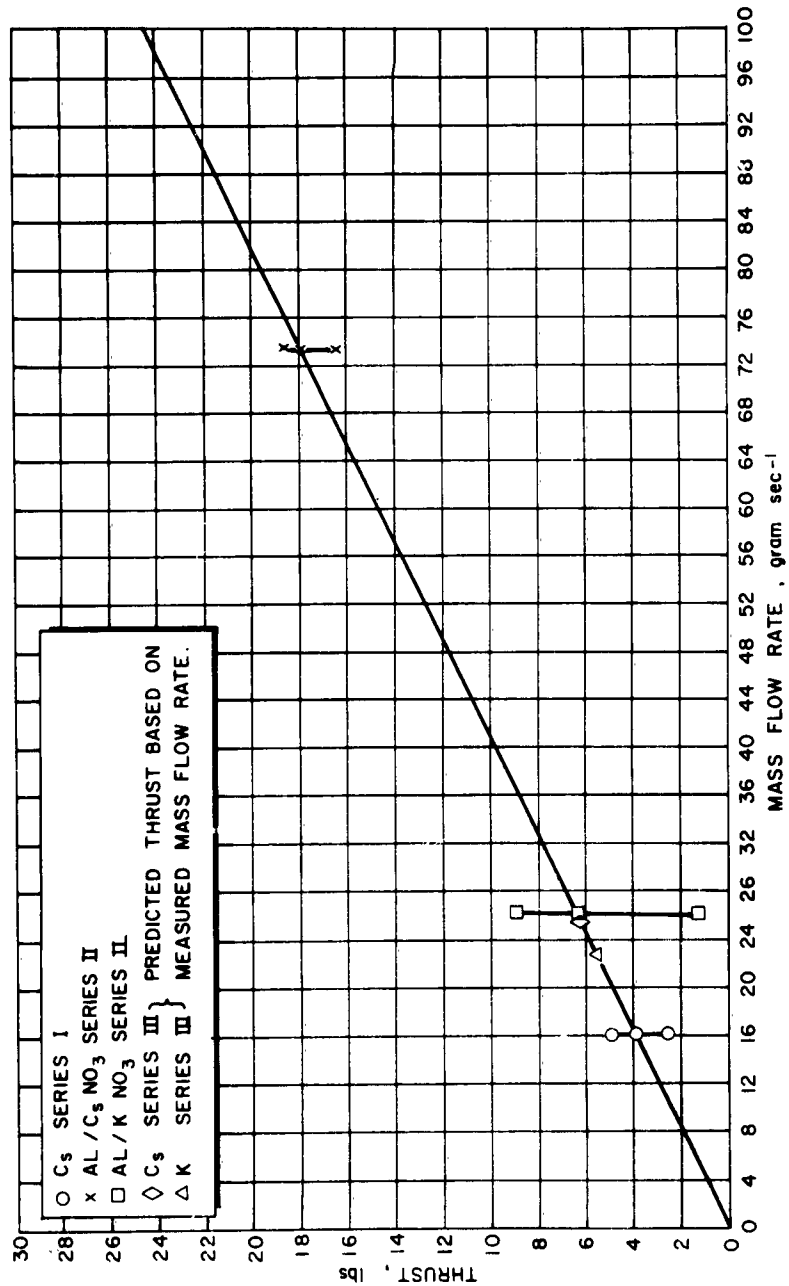
Figure 21 AVERAGE MOTOR THRUST VERSUS MASS-FLOW RATE FOR SERIES I
AND SERIES II MOTORS
(Series III points are based on measured average mass-flow rates.)
63-956

D. CHAMBER PRESSURE

It is informative to examine the pressure history of the chamber. The pressure was maintained at approximately 1.0 torr during the majority of test runs. This corresponds to an altitude of about 150,000 feet which is the lower altitude of interest for these motors. The high pumping rate of the steam ejector pump enabled the chamber pressure to remain relatively constant except during ignition. A typical trace is shown in figure 22.

Two additional pressures--20 torr and 100 torr--were utilized on two cesium and two potassium runs during the third series. Difficulties were encountered in maintaining a constant pressure during the run. In addition to this, the optical ports fogged rapidly, making observation of the plume impossible. Hence, interpretation of resultant data is extremely difficult.

E. NOZZLE OPERATION

An important factor in motor performance is the operation of the nozzle. In order to reduce thrust to a minimum and provide maximum plume expansion, the nozzle contained no expansion section. The material used had to withstand motor chamber temperatures of the order of 4000°K. Ideally, the material should have a low thermal conductivity so that the nozzle surface will operate hot, thereby avoiding condensation (slagging) of the molten Al_2O_3. Unfortunately, a nozzle operating under these conditions is subject to greater erosion, hence a compromise must be achieved. The first nozzles made of ATJ graphite exhibited severe erosion characteristics (figure 23). The nozzles used in the second series were of ATJ graphite with a tungsten insert. This insert considerably improved the erosion properties of the nozzle. It was found that heat-treating the tungsten further improved its ability to withstand erosion.

A different kind of nozzle fabricated with a molybdenum insert (figure 24) proved totally unsatisfactory. This nozzle was only used in the third series of potassium motors. Severe erosion occurred (figure 25). In one instance, the plume cut completely through the nozzle and the front steel plate. This released the motor pressure and the motor went out.

Throughout all motor runs, slag was more or less a problem. Tubular slag buildup around the orifice was experienced (figure 26). Very frequently, one side of the tube was cut open by the gas flow which was deflected by the remaining slag (figure 27). The central core of heavier-than-gas, molten Al_2O_3 continued through the slag tube and did not deflect. This permitted microwave attenuation measurements of Al_2O_3 separate from the gas flow.

It is quite likely that a puddle of slag formed in the burning chamber since the motor was fired at about 10 degrees declination. Photographic evidence shows slag running out and freezing on the lower side of the nozzle. Considerably

-30-

more erosion occurred on the lower side (figure 28). It is quite likely that this erosion was caused by an excess of molten aluminum (in the slag) chemically attacking the tungsten insert. The resulting compound is an intermetallic aluminum-tungsten mixture which has very weak structural properties. The slag was analyzed by X-ray diffraction and found to consist of $MgAl_2O_4$ (magnesium aluminate), Al (aluminum), $a-Al_2O_3$ (aluminum oxide), and small concentrations of Al_4C_3 (aluminum carbide).

F. CHEMICAL COMPOSITION OF PLUME

The combustion products resulting from burning a stoichiometric mixture of $CsNO_3$:Al are listed in table III. The majority of the gaseous products consist of N_2 and Cs. In addition, a large amount of molten Al_2O_3 is produced which contributes to the slagging problem. The reaction is very similar for KNO_3:Al with K being substituted for Cs in table III.

Note that no hydrogen is included in this reaction. A thermochemical program now in progress, but not yet available, includes the effects of hydrogen. Hydrogen may be introduced into the combustion process via burning of the organic inhibitor surrounding the grain, or because of the addition of organic binder to the grain. Carbon, which may be present due either to the nozzle or to the organic materials, is also included in the new calculations.

Spectroscopic examination of the plume did not reveal the presence of hydrogen lines. The spectrum was dominated by the visible cesium spectrum. Also, the dominant aluminum oxide (AlO) band head structures were observed. Of primary interest in the spectroscopic studies was cesium line broadening (Stark effect) due to electrons in the plume.

G. CENTRAL CORE OF THE PLUME

In order to examine the kind of solids in the plume, two kinds of particle catchers were fabricated. A stainless-steel pipe elbow, closed at one end, was employed both downstream (approximately 6 feet from the motor) and on the drop pendulum to collect sufficient material on which to perform X-ray and chemical analysis. Figure 29 shows the drop pendulum passing through the plume. The deflected gas flow prevented the obtaining of a distribution of solids in the core.

Initially, it was expected that the particles might be moving at supersonic velocities, thus, a smooth copper target was placed in the catchers to obtain some idea of the velocity by examining the size of microscopic impact craters. Results here indicate that the velocity was insufficient to cause any penetration of the particles into the copper. A reasonable estimate would place the velocity at a few hundred feet per second. The material collected was almost entirely Al_2O_3 and $y-Al_2O_3$, and the copper had the appearance of a surface flame-sprayed with this material. Very little crystalline structure was apparent from

TABLE III

COMBUSTION PRODUCTS FROM STOICHIOMETRIC

Al: $CsNO_3$

Species	Motor Pressure		14.7 psi (moles)
	1000 psi (moles)	121 psi (moles)	
O	5.367	8.486	11.186
N	0.075	0.048	0.027
e^-	1.236	1.801	2.435
Al	3.385	4.902	6.265
Cs^+	1.408	1.897	2.478
O^-	0.171	0.096	0.043
O_2	1.170	1.666	1.876
N_2	26.383	23.907	22.369
NO	2.353	2.049	1.574
AlN	0.001	--	--
AlO	3.761	4.985	5.520
Al_2O	1.434	1.845	2.017
Al_2O_3	0.403	0.425	0.365
Cs	51.917	47.771	43.830
Cs_2	0.935	0.122	0.016
Total Gas (moles)	99.999	100.000	100.001
Al_2O_3 (liquid	49.784	42.697	38.065
Temperature (°K)	4605.3	4130.0	3715.2
Mean Molecular Weight of Total Gas	86.59	80.65	76.50

X-ray diffraction measurements, and that which did appear was γ-Al_2O_3. This phase of aluminum oxide forms only when extremely rapid cooling has occured. The liquid-solid core is well defined down to about the 40-inch station where it tends to start spreading and diffusing. Figure 30 shows the central core of the plume. The shower of sparks resulted from molten slag creating a nozzle stoppage, and then being violently expelled. The temperature of the slag was relatively low and did not show up on the 0.4 to 0.5-micron film.

Attempts to measure the color temperature of the core were not successful due to the lack of a recording optical pyrometer. The manually operated instrument did not permit correct adjustment to be achieved in the burning time of the motor. This was particularly accentuated by the fact that the ports clouded somewhat after about 5 seconds of operation. The question of plume (primarily core) brightness is a difficult topic to discuss meaningfully without actual measurements. However, among five observers a qualitative value was agreed upon. The color-brightness characteristic of the plume, appears to the eye as being very similar to a tungsten photoflood lamp. The intensity of light along the region where the core is dominant appears to be not greater than that of a 500-watt photoflood for the $CsNO_3$ motors of series II. The other series were only about half as bright. The KNO_3 motors appeared to be about half of this maximum value also. Based on these estimates, the visible radiation is of the order of 40 watts/ster and 20 watts/ster respectively.

H. PLUME GEOMETRY

The presence of the central aluminum oxide core markedly alters the aerodynamic characteristics of the plume. The nozzle can no longer be regarded as simply an exit orifice. The relatively slow moving particles form a central region which effectively blocks the flow, thereby forming an annular orifice. Thus, the gas flow will be to a certain extent trapped in the matrix of slow-moving particles, and to a much larger extent will form a flow around the core.

The recompression shock is annular (figures 15 and 31). The pictures photographed by cameras located downstream from the motor show the annular shock more clearly. Figures 31a, b, c show similar photographs of the plume in three spectral ranges. The relative brightness in the different photographs is not significant since the film was not calibrated; however, each photograph shows the relative intensity at various locations in the plume for the given wavelength band.

The slag buildup has a very important influence on the plume geometry. The massive solids are undeflected in the plume, whereas irregularities due to slag will deflect the gas flow. In the extreme case shown in figure 27, the slag is in the shape of a slotted tube, thereby allowing the gas flow to be deflected to one side. Since the core no longer influences the flow, the recompression shock does not exhibit the annular characteristic (figure 32). Electron density measurements were made on such a core separated from the gaseous plume. No attenuation at the 40-inch station was observed with the 35 gc equipment indicating that the illumination is predominantly from heated solids rather than plasma.

-33-
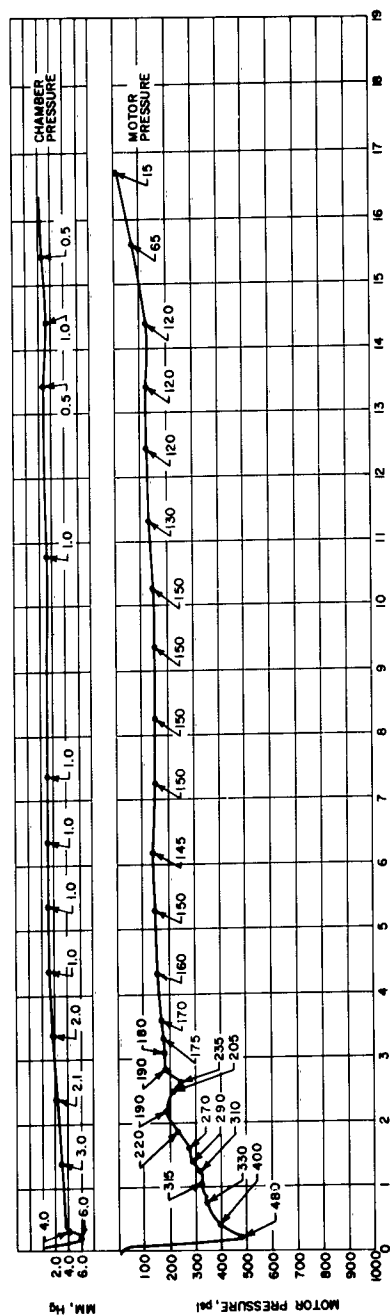
Figure 22 TYPICAL CHAMBER PRESSURE AND MOTOR
PRESSURE CHARACTERISTICS
63-957

-34-
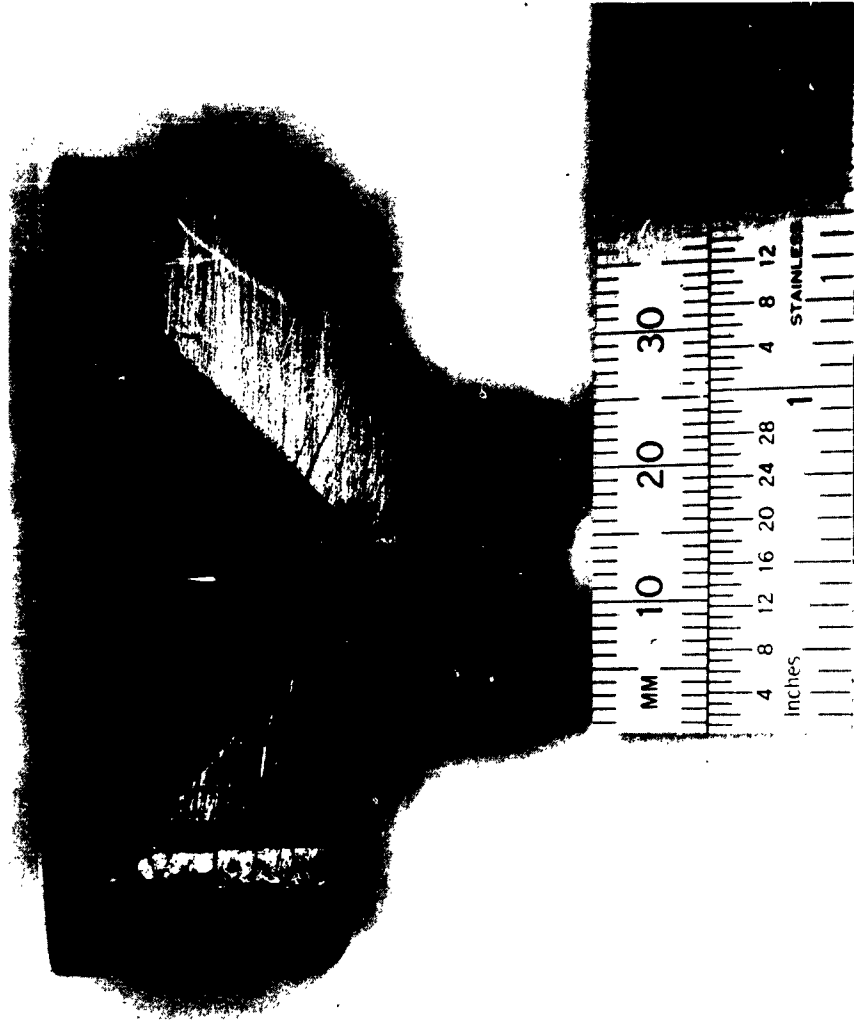
Figure 23 CROSS SECTION OF ATJ GRAPHITE NOZZLE USED IN SERIES I
(Solid material in orifice is slag)

Figure 24 MOLYBDENUM NOZZLE ASSEMBLY (AFTER FIRING) USED ON
SERIES III A1: KNO3 MOTORS
(Note erosion of nozzle core.)

-36-

Figure 25   MOLYBDENUM NOZZLE FAILURE USED ON SERIES II Al:KNO$_3$ MOTORS

Figure 26 SLAG BUILDUP AROUND Al: CsNO₃ MOTOR NOZZLE
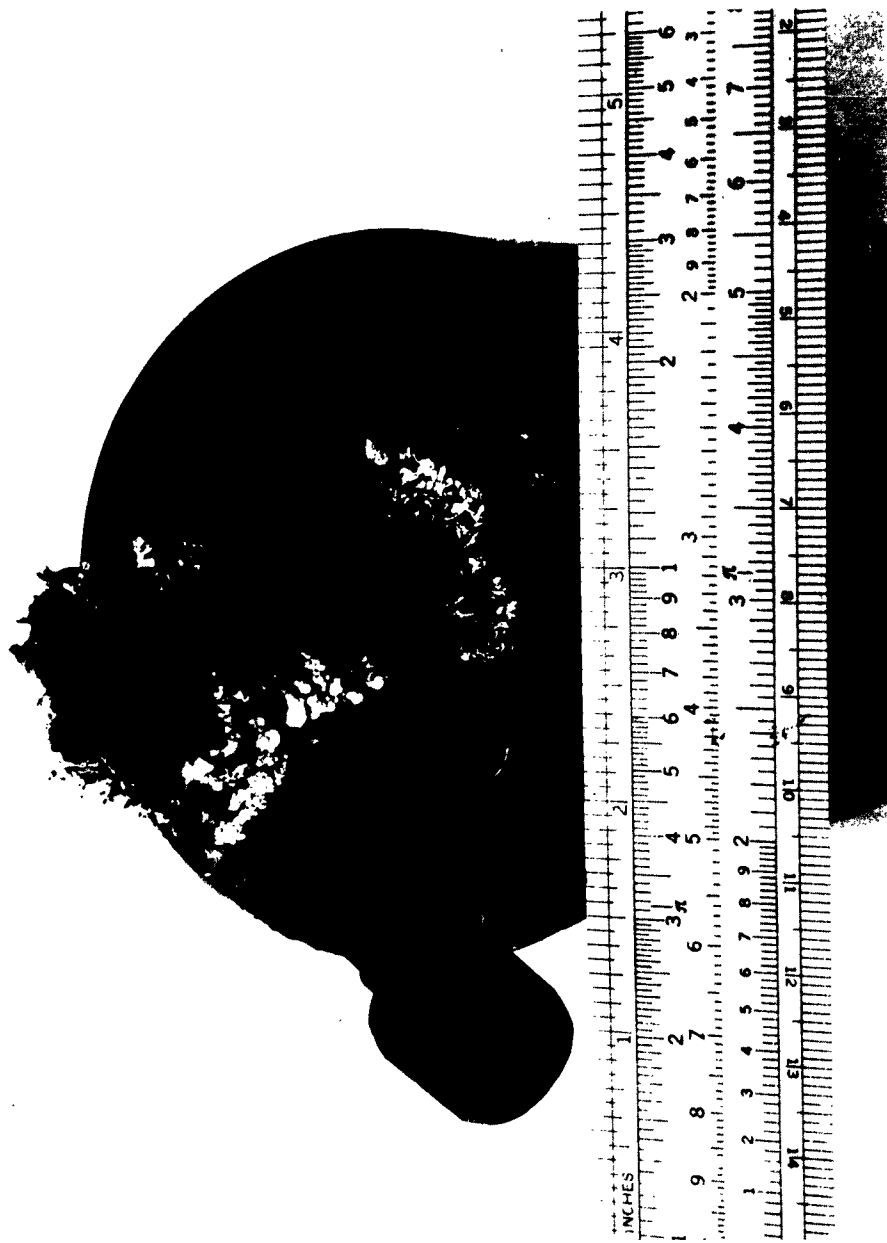
Figure 27 TUBULAR SLAG BUILDUP CUT OPEN ON ONE SIDE BY HOT GASES
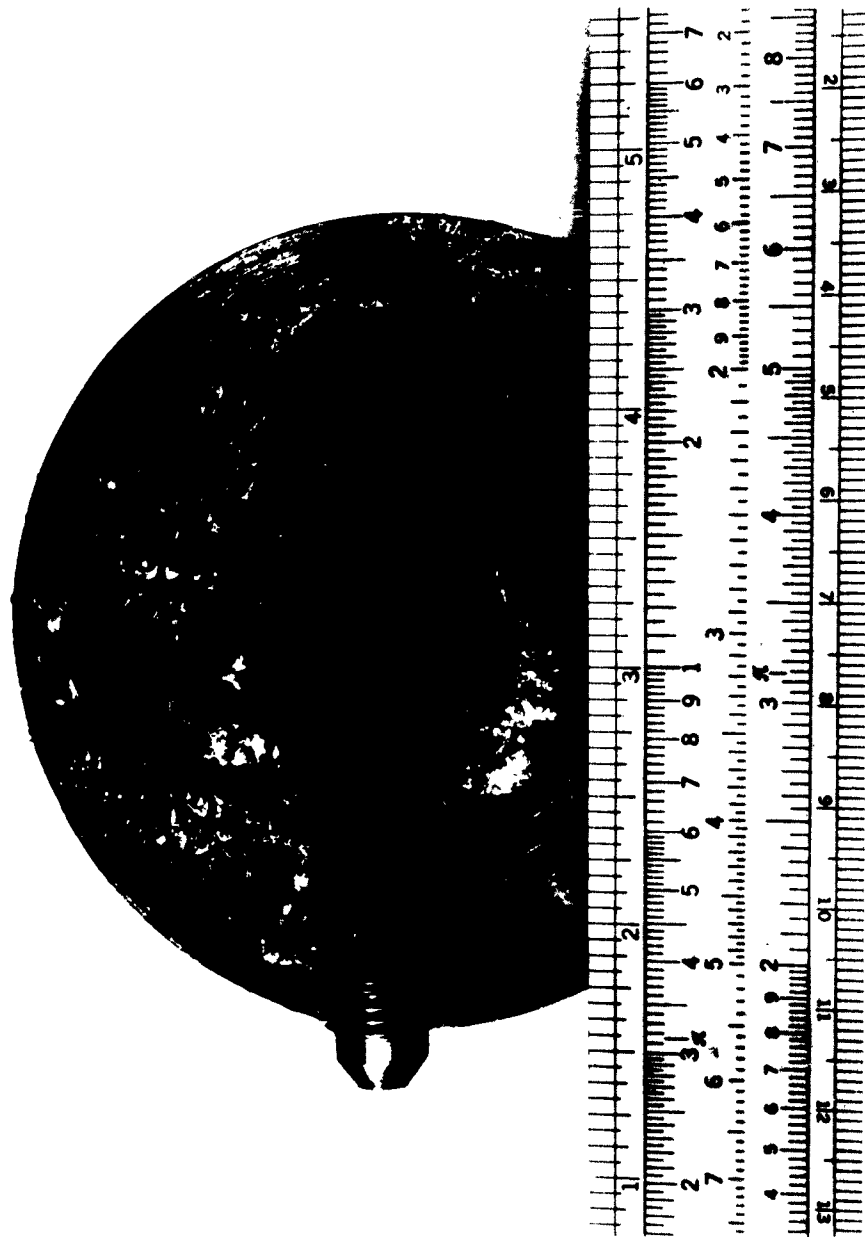
Figure 28 NOZZLE ORIFICE EROSION

Figure 29 HIGH-SPEED PHOTOGRAPH OF DROP PENDULUM AS IT PASSED
THROUGH THE PLUME
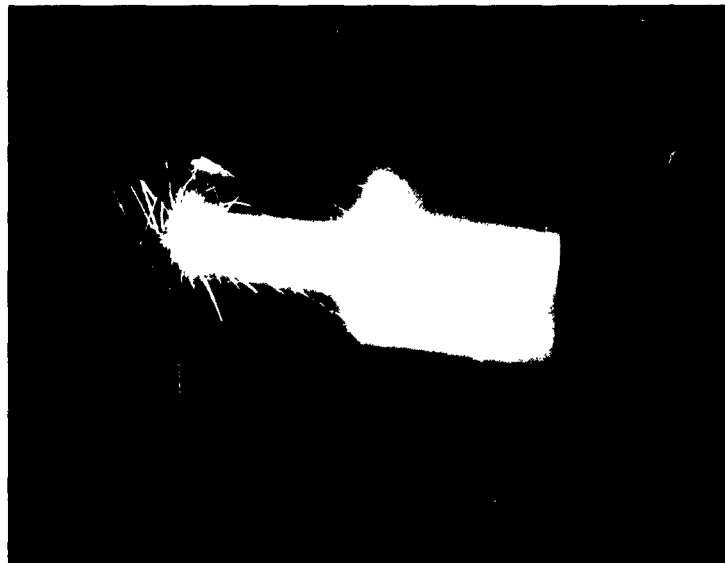
Figure 30 MOTOR OPERATION WHILE EXPELLING A SHOWER OF HOT SLAG SPARKS
(Note well defined central core containing solid materials.)
63-958

(a) 0.4 μ TO 0.5 μ

(b) 0.59 μ TO 0.68 μ

(c) 0.73 μ TO 0.87 μ
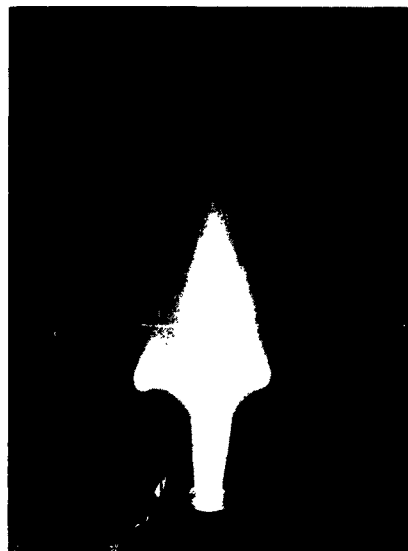
Figure 31 PLUME OF Al : Cs NO₃ MOTOR PHOTOGRAPHED IN THREE SPECTRAL RANGES

63-959

-43-

Figure 32 EFFECT OF SLAG-BUILDUP ON THE NOZZLE
(Notice the straight core of massive solids and
the deflected gas flow.)

I. PLASMA CHARACTERISTICS OF THE PLUME

1. Adiabatic temperature, density, and velocity calculation

Properties from adiabatic expansion consideration will be described next. This computation does not include the effect of the central core or the mixture of gases involved. However, it provides a first-order approximation of the flow conditions in the plume. The density in the plume, ρ_p, after expansion from motor chamber conditions P_c, ρ_c, T_c, is

$$\frac{P_c}{P_p} = \left(\frac{\rho_c}{\rho_p}\right)^\Gamma . \tag{1}$$

Expansion proceeds until the plume has equalized pressure with the ambient pressure; therefore

$$\rho_p = \rho_c \left(\frac{P_\infty}{P_c}\right)^{\frac{1}{\Gamma}} ; \tag{2}$$

similarly

$$T_p = T_c \left(\frac{P_\infty}{P_c}\right)^{\frac{\Gamma-1}{\Gamma}} . \tag{3}$$

The choice of Γ to use in the plume is uncertain and will undoubtedly vary from location to location in the plume, due to the lack of complete mixing of the various constituents and the degree of equilibrium. In order to examine the effect of Γ for typical operating conditions, the following values (from which table IV has been prepared) are assumed:

$$P_c = 7600 \text{ torr}; \quad T_c = 4200°K; \quad \frac{\rho_c}{\rho_0} \simeq 1 \text{ Amagat}$$

Using $\Gamma = 1.67$, a method of characteristics program was employed to determine plume boundary coordinates and thermodynamic properties. The external flow was taken to match conditions comparable to the NRL test. Since the program requires the flow to be supersonic, the runs terminated at shock wave locations. For the $P_\infty = 1$ torr case, this occurred at an axial distance of eight throat radii (figure 33). At 20 torr, the program dumped at 32 radii (figure 34). For the latter case, the flow had

TABLE IV

DENSITY AND TEMPERATURE IN THE PLUME

P_∞ (torr)		$\Gamma = 1.4$	$\Gamma = 1.5$	$\Gamma = 1.67$
1	ρ_p / ρ_o	1.3×10^{-3}	2.5×10^{-3}	4.7×10^{-3}
	$T(^\circ K)$	334	220	118
20	ρ_p / ρ_o	1.6×10^{-2}	1.9×10^{-2}	2.3×10^{-2}
	$T(^\circ K)$	750	590	390
100	ρ_p / ρ_o	4.5×10^{-2}	5.5×10^{-2}	7.4×10^{-1}
	$T(^\circ K)$	1330	1000	740

turned parallel to the jet axis and so represents an approach to final expansion. However, in the former case, the boundary was still at 30 degrees inclination and represents only partial expansion. The plume boundary for the 100-torr case is shown in figure 35.

A soft copper wire grid was placed in front of the motor during one run. The grid junctions, held together by soft solder joints, melted in the hot gas flow and permitted the soft wires to bend, thereby outlining the flow field. The calculated values of figure 33 are plotted on a photograph of the grid in figure 36, and extrapolated for the full 10 inches of the grid. The grid spacing here is 1/2 by 1 inch. The shock ring occurred beyond the grid.

Another type of grid, consisting of woven alternating wires of 0.020 inch tungsten and molybdenum (forming a 1- by 2-1/2-inch mesh), was designed to glow instead of bend. Thus the flow field can be more easily photographed as in figure 37. Unfortunately, the computed values for this flow cannot be easily plotted, since the photograph is overexposed near the nozzle, where the calculation is valid. Examination of figure 37 shows that the flow clearly separates into an outer, cool (i. e., nonradiating) skirt and an inner radiating region.

The aerodynamic characteristics of the plume can only be approximated, since the gas flow consists of a wide variety of dissimilar gases plus a central core of solids and liquids. Of utmost importance for plasma consideration is the distribution of the cesium or potassium. Cesium with an atomic weight of 133 (compared with the molecular weight of $N_2 = 28$ or $O_2 = 32$), will tend not to follow the streamlines of the lighter gases, hence heavier concentrations of cesium are to be expected in the central region. This is also true but to a lesser extent for potassium with an atomic weight of 39.

Operation of the motor at higher chamber pressure was difficult to observe. All of the photographic data was obtained during the first 2 or 3 seconds of operation before the ports clouded with smoke deposits. Since this is the time when the igniter is burning and the pressure is quite high, it is not truly representative of plume configuration when the grain is burning. The early plume at 20 torr is seen in figure 38. The plume is considerably foreshortened. An interesting double image of the plume can be noticed in this figure. The smaller reflection image (apparently reflecting from the port window) may be noted at the lower end of the plume and clearly shows a multiple annular shock structure. Confirming this, is figure 39, which was photographed through a neutral-density filter. Multiple recompression shock regions are apparent at this higher pressure compared with the single shock at 1 torr. Figure 40 shows operation in the 1st second of burning at 100 torr. The grainy appearance of the photograph is due to deposits on the port. The plume is further foreshortened from its appearance at 20 torr. The large amount of smoke produced is evident. Within 1 second, the plume was not visible through the port.

-47-

X/Re
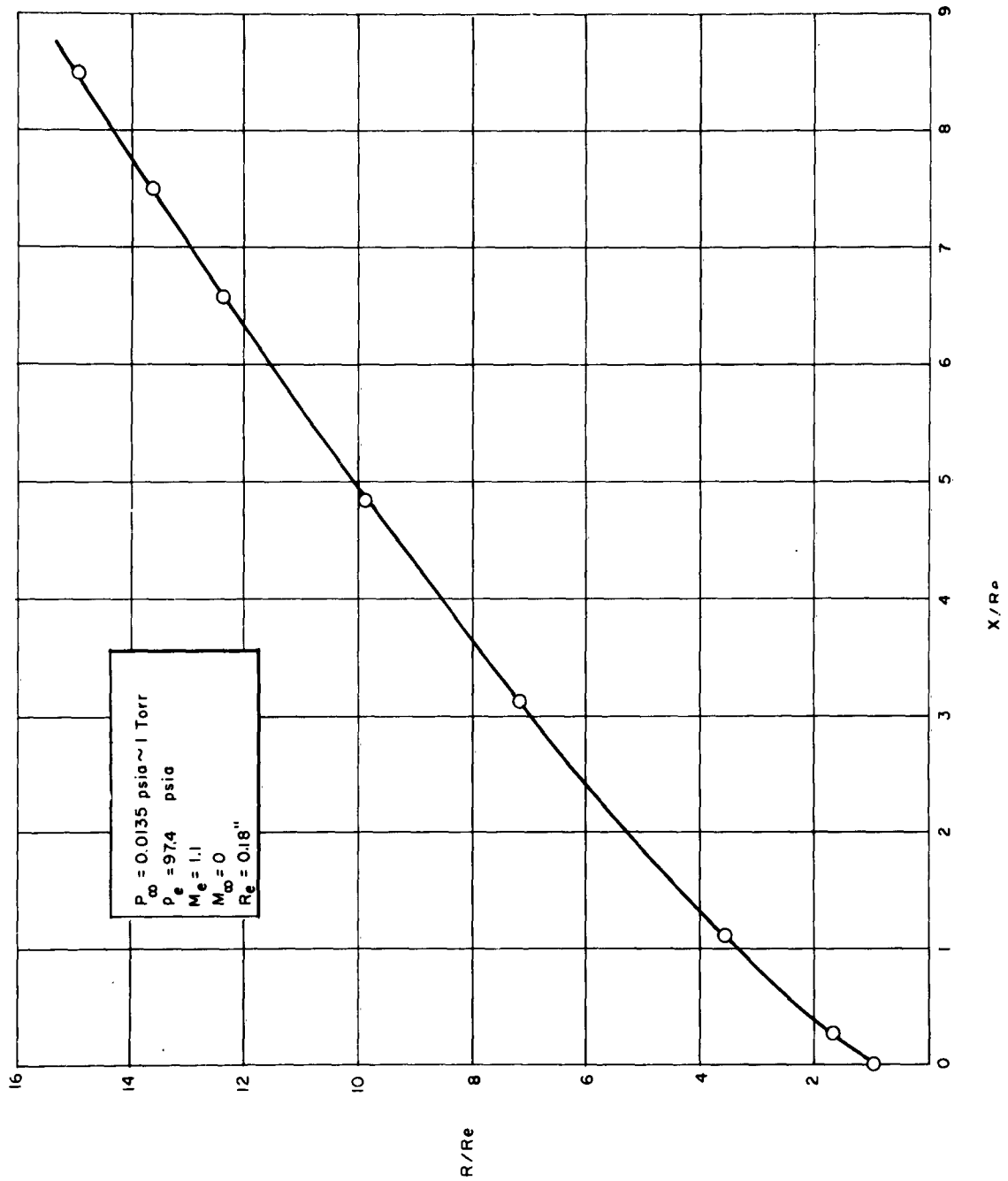
Figure 33 CALCULATED PLUME BOUNDARY AT 1 TORR BASED ON METHOD
OF CHARACTERISTICS PROGRAM
63-2771

P_∞ = 0.0135 psia ～ 1 Torr
ρ_e = 97.4 psia
M_e = 1.1
M_∞ = 0
R_e = 0.18"

R/Re
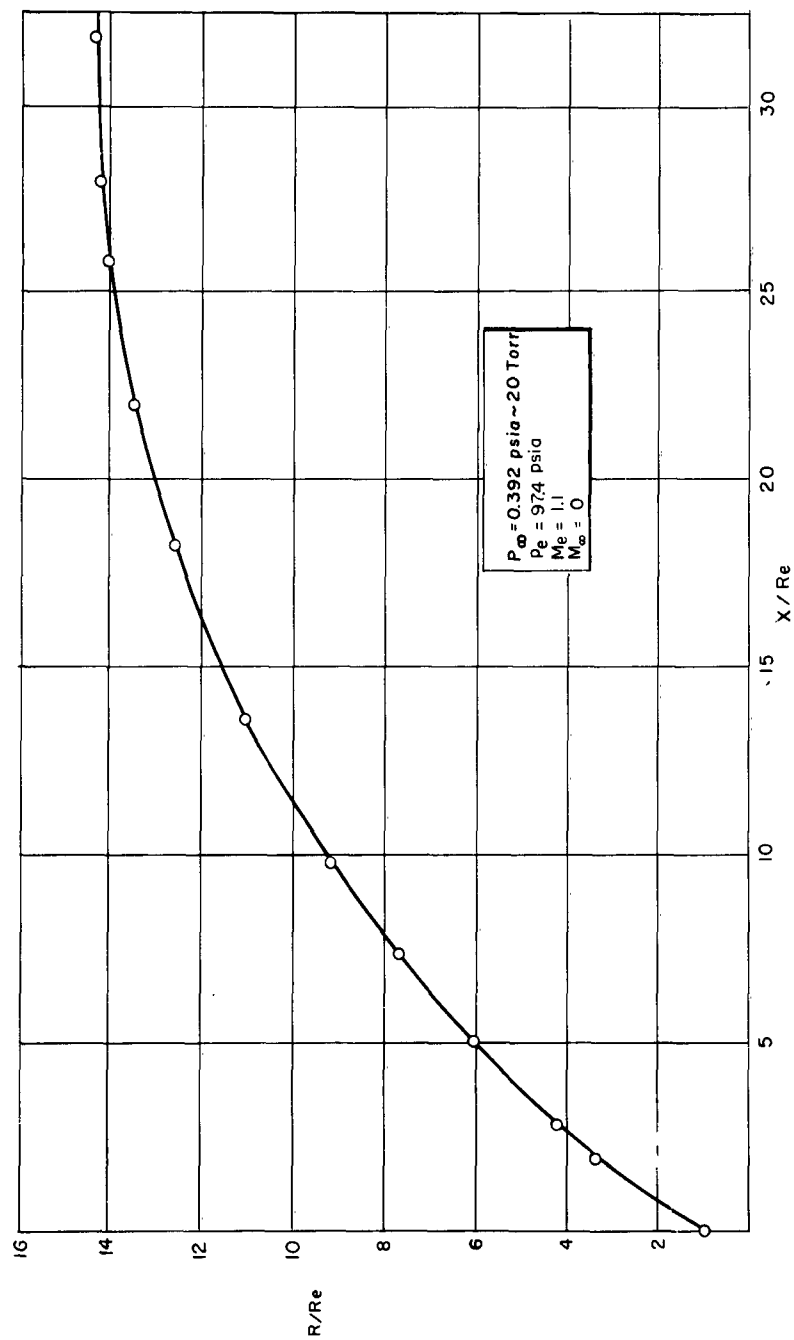
Figure 34 CALCULATED PLUME BOUNDARY AT 20 TORR BASED ON METHOD
OF CHARACTERISTICS PROGRAM

63-2769
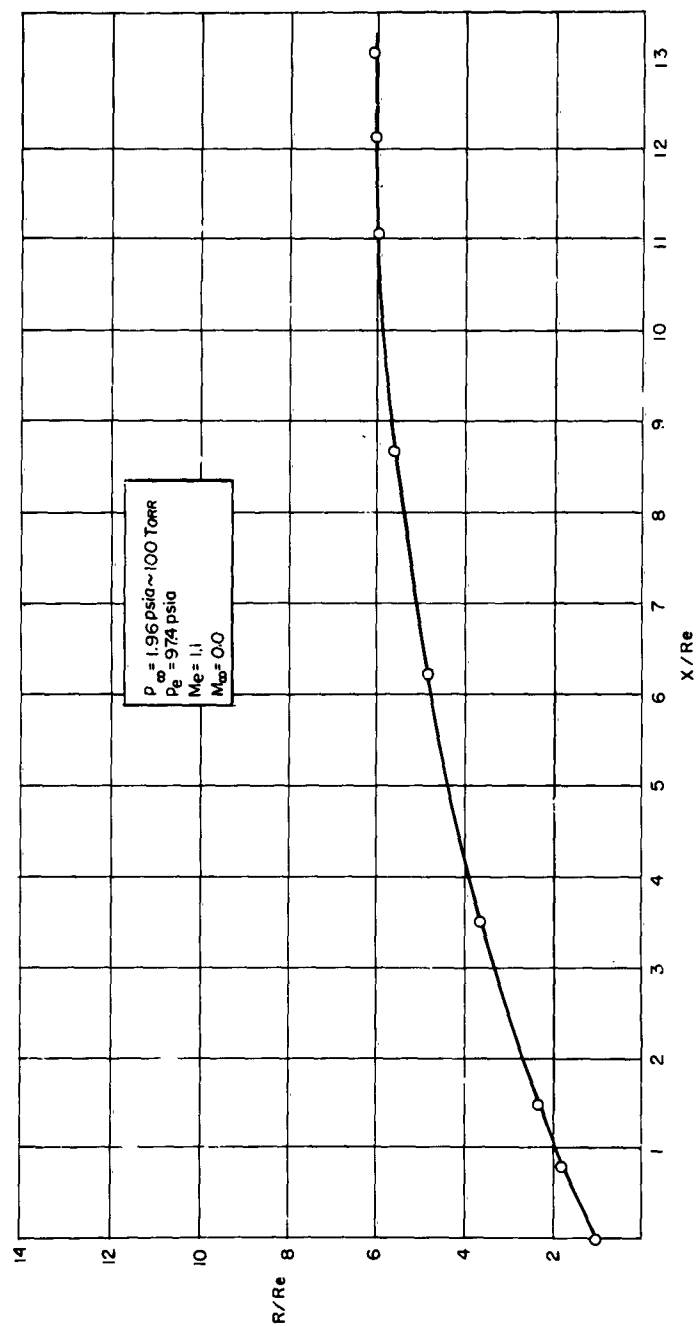
Figure 35 CALCULATED PLUME BOUNDARY AT 100 TORR BASED ON METHOD
OF CHARACTERISTICS PROGRAM
63-2770
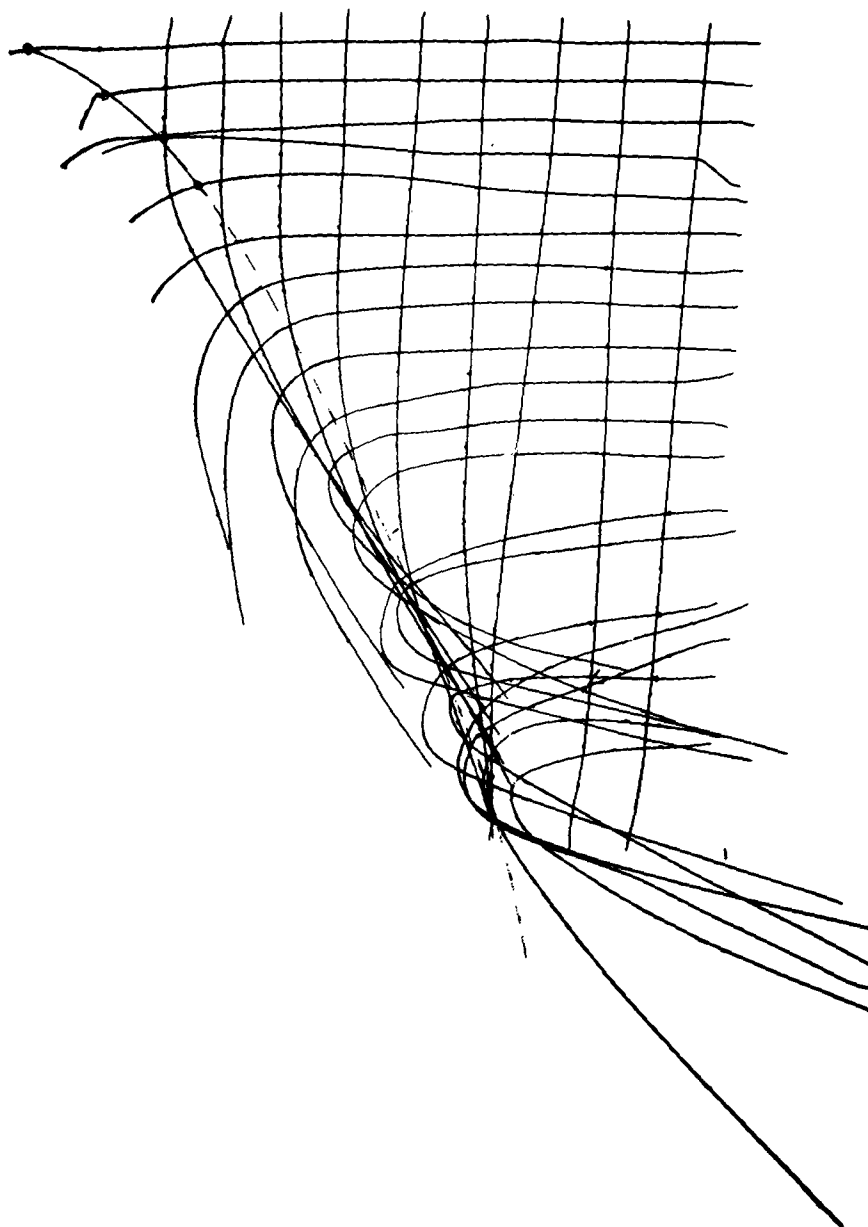
Figure 36 BENT-WIRE GRID OUTLINES THE FLOW FIELD AT 1 TORR
(Solid line is calculated boundary. Dotted line is an approximate
extrapolation; however, the plume would be expected to eventual-
ly turn parallel to the axis. The shock ring occurred to the left of
the grid and was approximately 12 inches in diameter.)
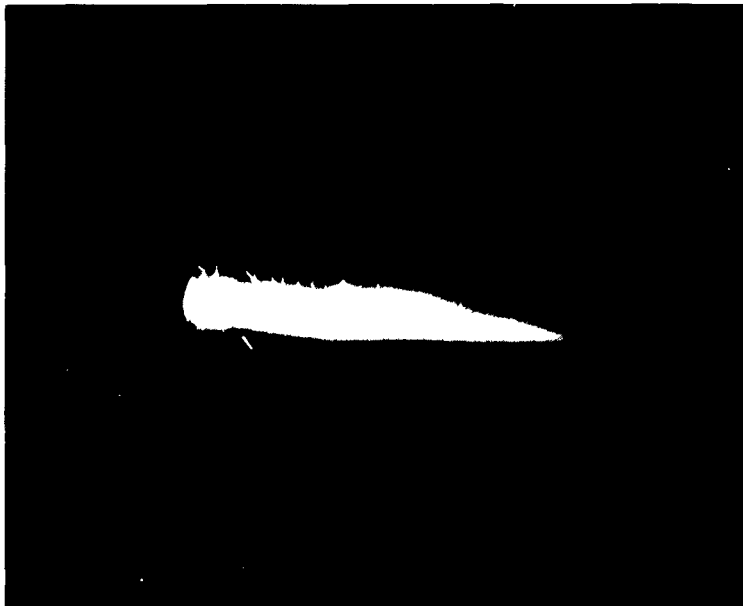
Figure 37 GLOWING TUNGSTEN-MOLYBDENUM GRID OUTLINES FLOW
FIELD AT TORR
Motion pictures taken with neutral density filters indicated that
tubular slag buildup on the nozzle had occurred thereby reducing
full plume expansion. (Plume diameter $\simeq$ 8 inches.)
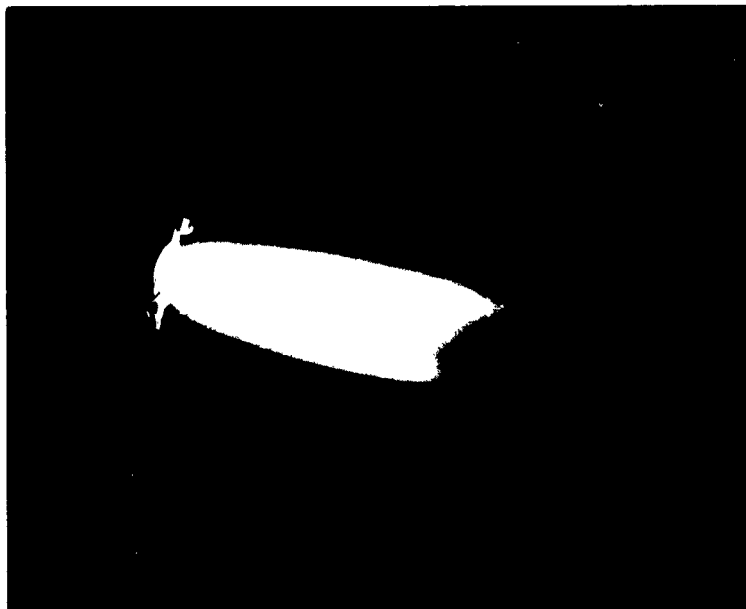
Figure 38 PLUME CONFIGURATION AT 20 TORR PRESSURE
Note reflected image from window port (lower end of
plume) which shows shock structure.
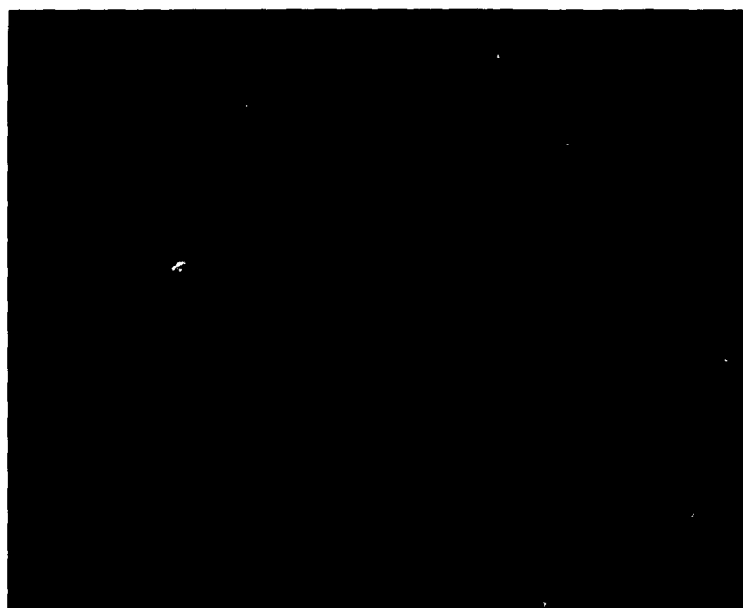
Figure 39 PLUME CONFIGURATION AT 20 TORR PRESSURE
(Photographed through neutral density filter to show
shock configuration.)

Figure 40 PLUME CONFIGURATION AT 100 MM PRESSURE DURING FIRST SECOND
(Note smoke which obscured port after first second of operation.)

Figure 40 PLUME CONFIGURATION AT 100 MM PRESSURE DURING FIRST SECOND
(Note smoke which obscured port after first second of operation.)

The flow velocity in the plume is obtained from the energy equation

$$h_c = h_p + \frac{u_p^2}{2} \simeq \frac{u_p^2}{2} \tag{4}$$

or

$$u_p \simeq (2 C_p T_c)^{1/2} \quad , \tag{5}$$

where

$$c_p = \Gamma c_v = \Gamma \frac{3}{2} \frac{R_o}{m} \quad . \tag{6}$$

Approximate values for the cesium plasma and potassium plasma are:

$$u_{cs} = 1.45 \times 10^5 \text{ cm/sec} = 4830 \text{ ft/sec} \tag{7}$$

$$u_k = 2.52 \times 10^5 \text{ cm/sec} = 8400 \text{ ft/sec} \tag{8}$$

where m is taken as 100 for the cesium plume and 33 for potassium plume, (note that the plume is a nonuniform mixture of gases, thus values of m can only be approximated). The effect of uncertainty in Γ on velocity is small and may be neglected.

2. Optical Measurements of Electron Density

In the course of the three test series, four different spectrographic instruments were used. Of the measurements, only those made in series III utilizing a laboratory-constructed grating instrument, with a dispersion of 26 A/mm, were of value in determining electron density. A word regarding the scanning spectrometer should be included, however. This instrument has much greater dispersion than the above mentioned instrument, but it achieves this at the expense of a very low scanning rate. Thus, where the time of operation was short and the possibility of unpredicted lines in the spectrum great, the instrument was found to be unsuitable.

The theory of line broadening due to electrons in a hydrogenic plasma is well known. Only recently, however, have the Stark constants for cesium lines been worked out. [1] Using these data and examining the lines which should exhibit the greatest broadening, no evidence of broadening could be clearly discerned. The spectrum was obtained 18 inches from the nozzle and approximately 2 inches off axis (near the edge of the central core). The following lines which exhibit considerable broadening were chosen for examination.
-56-

Line (Å)	Width at $n = 10^{16}$ cm^{-3} (Å)
6629	51.7
6586	51.7
6326	137.0
5073	199.0
5042	365.0

The Stark effect is linear; thus an electron density of 10^{14} cm^{-3} would result in a line broadening 10^{-2} of the listed values. The limit of resolution of the spectrograph and densitometer is approximately 0.5 A; thus line broadening of less than this value, occuring for electron densities in the region of 10^{14} cm^{-3}, could not be measured. Unfortunately, a few lines which might be broad enough to be measured at 5×10^{13} cm^{-3} were so faint that instrument noise (emulsion grain and scanner noise), prevented the obtaining of resolutions greater than about 1A, for these lines. No broadening was observed in the measured lines; thus it is concluded that electron densities greater than 10^{14} cm^{-3} were not observed at this location. Electron density values less than this were not measurable by this technique.

3.   Microwave Measurements of Electron Density

The use of microwaves as a nondisturbing plasma probe is well known. Of the several techniques which may be employed, only a focused-beam transmission system permits measurements without interfering with the aerodynamic flow pattern of the plume, yet with sufficient resolution to permit measurement of gradients. The basic system was described earlier in this report. In an attempt to measure as dense a plasma as possible, a 35-gc system was employed in series I. This system exhibited considerable frequency drift and was not satisfactory in obtaining a detailed plasma density profile of the plume since it was uncertain whether attenuation change was due to the plume attenuation or frequency drift. Thermal drift did not prevent determining the approximate amount of attenuation due to plasma , since the thermal drift curve was gradual throughout the run, resulting in a sloping instead of constant base line. The second series employed a 70-gc system which also exhibited the same undesirable characteristics as the 35-gc equipment. Two runs in the second series were performed at 35 gc after readjusting the 35-gc system slightly, with somewhat improved results over the first series.

Inherent difficulty in both systems resulted from the slow scan rate of the servo-operated system. It should be noted that instability in the plume due to slag formation and nozzle erosion caused serious errors in the attempt to measure the electron density profile in the plume with a slow scan system. Scan time for the plume should be fast relative to instability times in the plume, to ensure that changes in attenuation are due to plume gradients.

For the third series, a 23.5-gc system which was known to be exceptionally stable was used with good results. The reliable data and the aforementioned motor oscillator, which permitted a rapid plume scan rate, allowed a detailed analysis of plume data. The drift problem in addition to the slow scanning rate of the first two series of tests, do not warrant the same detailed analysis; therefore, only an average value of electron density has been computed for the second series.

The analysis of the propagation of electromagnetic waves through a homogeneous plasma is well known. Analysis is most conveniently carried out in terms of the parameters

$$\gamma = \frac{\nu}{\omega} \tag{9}$$

and

$$\eta = \frac{\omega_p^2}{\omega^2} = 8.1 \times 10^7 \frac{N}{f^2} \tag{10}$$

Of prime concern is the attenuation constant for the electromagnetic wave in terms of these two parameters. Depending upon the magnitude of γ and η relative to unity, various regions can be outlined in a map plotting α, γ and η. The regions of interest in this mapping are $\gamma \leq 1$ and $\eta < 1$. The attenuation constant is given by the following relations:

$$\alpha = 8.6 \frac{\omega}{2c} \gamma\eta \quad db/m \quad (\gamma < 1, \ \eta < 1) \tag{11}$$

$$\alpha = 8.6 \frac{\omega}{2c} \frac{\gamma\eta}{(1 + \gamma^2)} \quad db/m \quad (\gamma \cong 1, \ \eta < 1). \tag{12}$$

Figure 41 is a graph of these equations, over the region where the measurements were performed.[2]
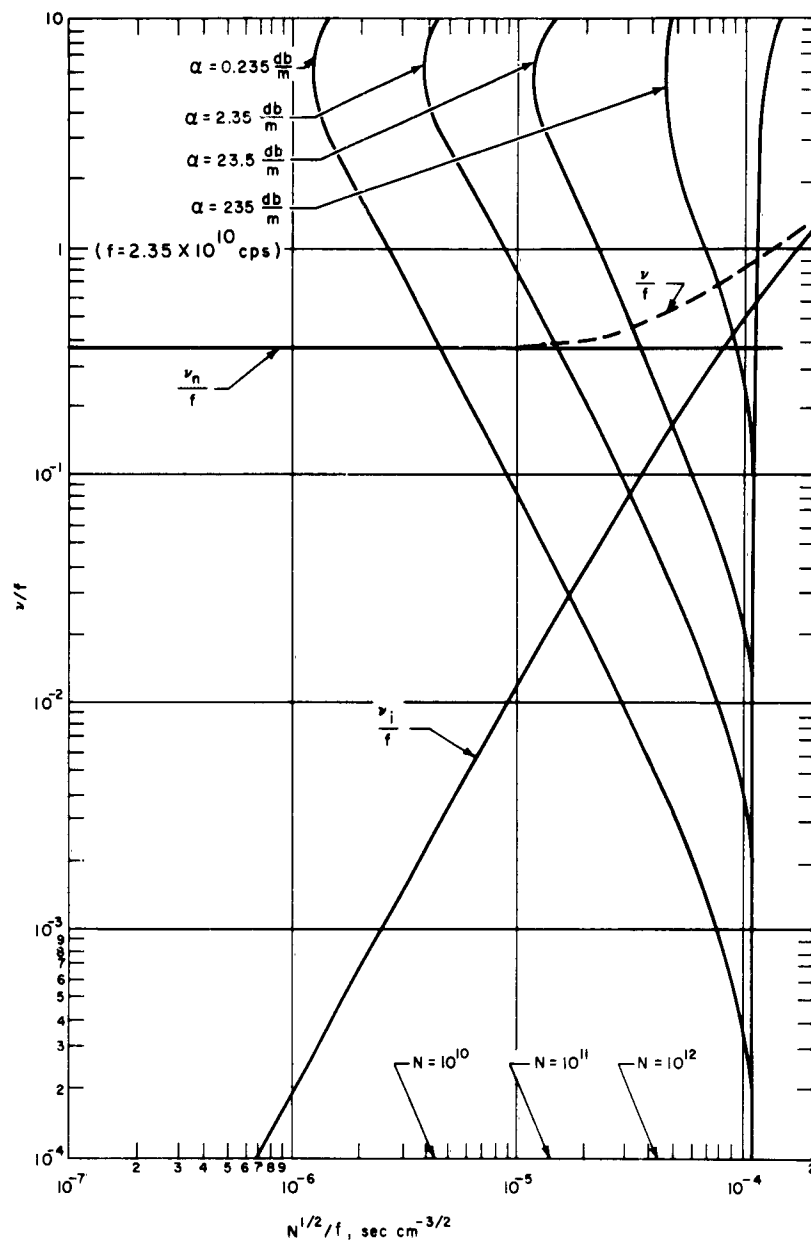
Figure 41 COLLISION FREQUENCY VERSUS SQUARE ROOT OF ELECTRON
DENSITY FOR VARIOUS ATTENUATION CONSTANTS
(All variables are normalized with respect to frequency.
Collision frequency for collisions between electrons and electrons,
ν_n ; Electrons and ions, ν_i ; and $\nu = \nu_n + \nu_i$ are also plotted.)

It becomes immediately apparent that two unknowns are involved in determining the attenuation constant -- collision frequency and electron density. However, only one measurement has been made; therefore, one or the other of these must be assumed known. Of these, the electron density is more sensitive to pressure and temperature variations than is collision frequency, hence the approach here is to estimate the collision frequency in the plume.

There are two types of collisions that may be important; those involving electrons and ions and those between electrons and neutral atoms or molecules. The total collision frequency is given by[3]

$$\nu = \nu_i + \nu_n \quad .$$ (13)

Where

$$\nu_i = \frac{5.5 N}{T^{3/2}} \ln \left(\frac{280 T}{N^{1/3}} \right)$$ (14)

$$\nu_n = \bar{v} \sum_j n_s Q_s \quad .$$ (15)

In order to apply these formulas, the gas density and temperature must be determined. This at best can only be approximated since the large expansion at the nozzle has a tendency to freeze the flow. On the other hand, the flow will return to equilibrium downstream from the shock region and may be heated by solids in the flow. The status of the frozen flow-equilibrium question cannot be ascertained at the measuring stations, but these extremes do provide upper and lower bounds on values of collision frequency. Also of significance is the circularity of the solution involving computation of the electron-ion collision frequency; i.e., the electron density (equal to the the ion density) must be known before the ion-collision frequency can be determined, but this cannot be known until the electron density is computed, based on a knowledge of the collision frequency. This dilemma can be resolved in terms of providing an upper limit to the collision frequency (and correspondingly from equations (11) and (12) a lower limit to the electron density) based on the aerodynamic characteristics and the limits set by the measured attenuation in the plume.

To maximize ν_i (equation 14) it is assumed that equilibrium exists and that the flow has expanded and cooled to ambient temperature. A reasonable estimate for this temperature is 250°K, based on equilibrium expansion from the combustion chamber to an ambient pressure of 1 torr (see table IV). It seems unlikely that the temperature is actually that low at the measuring stations, since the solids in the core are still luminous (thereby assuring considerable heat exchange in the central region) and the ambient gas temperature in the

chamber rises to about 400 °K during the run. Table V lists values of ν_i for various assumed values of N, up to the upper limit set by spectrographic measurements.

TABLE V

ELECTRON-ION COLLISION FREQUENCY

N (cm^{-3})	ν_i (sec^{-1})
10^{10}	4.8×10^7
10^{11}	3.8×10^8
10^{12}	2.7×10^9
10^{13}	1.6×10^{10}
10^{14}	5.7×10^{10}

These data are plotted in figure 41. Note that electron-ion interactions are important only near the upper limit of electron density.

The electron-neutral collision frequency is less temperature-sensitive than the electron-ion collision frequency.

$$\nu_n = \bar{v} \sum_j n_s Q_s \propto P T^{-\frac{1}{2}}$$

The species present in the plume in sufficient quantity and with a large enough collision cross section (Q) to be considered are O, O_2, N_2, NO, and Cs. The values of Q and the quantity of each are listed in table VI. The mean thermal velocity is computed on the basis of equilibrium T = 250 °K. The previous comments on the assumed value of T also apply to this computation.

TABLE VI

ELECTRON-NEUTRAL COLLISIONS

Species	η $(10^{15}\ cm^{-3})$	Q $(10^{-15}\ cm^2)$	$\bar{v}$ $(10^7 cm\ sec^{-1})$	ν_n $(10^7\ sec^{-1})$
O	4.8	1.5	1.0	7.2
O_2	0.9	0.4	1.0	0.4
N_2	13.4	0.7	1.0	9.4
NO	1.1	0.8	1.0	0.9
Cs	26.5	34.0	1.0	900.0

The values listed in table VI are also approximately valid for potassium, except that Q has a larger value by about 20 percent, leading to an increase in ν_n by this amount.[4]

The electron-neutral collision frequency for cesium is plotted in figures 41. Note that ν_n is dominant until a = 2.35db/m. However, a reasonable assumption is that ν_i is negligible in the region a = 2.35db/m, since the $T^{-3/2}$ dependency will greatly reduce ν_i if a value of T greater than 250 °K were used. For this reason, electron-density calculations are based on ν_n .

Electron densities in the plume were only determined for an ambient test chamber pressure of 1 torr. Data at higher test chamber pressures were ambiguous due to the uncertainty of plume configuration, caused by the aforementioned fogging of the camera ports.

The microwave attenuation data records total attenuation through the plume as a function of distance from the center. The attenuation scale on the recorder is nonlinear and is calibrated in 3-db steps prior to each run. The propagation path through the cylindrical plasma is along the diameter, when the plume is centered with respect to the microwave lens. When the plume is not centered, the path is foreshortened along a chord through the plasma. Oscillating the motor so that the plume is swept past the lens permits measuring the attenuation along all chords from the center to the outer edge. Furthermore the radial symmetry of the plume can be evaluated. The oscillation rate of the motor was such that two or three complete sweeps were obtained during the motor burning time. However, the raw data present attenuation on a time scale which is nonlinear with

respect to displacement of the propagation path from the center of the plume (figure 42). Hence, these data must first be reduced to a plot of total attenuation versus radius. These data are shown for the cesium motors at the 40-inch and 50-inch stations in figures 43 and 44. Data taken at the 60-inch station showed no significant attenuation, while at the 20-inch station, total attenuation was observed in the central region of the plume. The ambiguous values of attenuation at the 40-inch station occur due to the fact that a transition from the first channel (0 to 9 db) to the second channel (9 to 18 db) occurs in the central region of the plume. The characteristic noise observed with this type of measurement, when the higher gain channel was in use, gives rise to spurious response in this channel; thus, the upper and lower limits are included here, so that the effect of this error may be evaluated. Figure 45 shows photographs of oscilloscope traces of the modulation envelope (square wave) received through the plasma as the plasma becomes more dense. Notice the build-up of noise on the square wave which gives rise to the spurious response of the system. Such ambiguity did not occur for the lower attenuation values at the 50-inch station (figure 43). Again, the same characteristics are observed for the potassium plumes at the 20- and 40-inch stations (figures 46 and 47).

The local attenuation constant a is obtained by the graphical solution of Abel's integral.[5] These results are plotted in figure 48 for the cesium plumes and in figure 49 for the potassium plumes. Figure 50 permits comparison of a for the cesium and potassium plumes at the 40-inch station.

The attenuation constant depends on both the electron density and the collision frequency. However, both of these quantities are completely controlled in the plume by the distribution of the alkali metal. Thus, the shape of the a profile in the plume gives a qualitative picture of this distribution. Both N and ν are linearly dependent on the cesium (or potassium) gas density; therefore,

$$a \propto \rho_{alk}^2$$

In order to include this effect in computing N, the collision frequency ν_n was assumed to have a distribution varying as $a^{1/2}$ where the computed value of ν_n in table VI represents the median value. At the peak value of a, ν_n is taken as twice the median value. Although these assumptions are to an extent artificial, they do include characteristic features of the plasma and provide a more realistic N profile than would an assumption of uniform ν_n. These values of ν_n are plotted in figures 51 to 53. The same median value of ν was used for both Al:CsNO3 and Al:KNO3 plumes. The greater plume radius and lower density of potassium discounted its higher cross-section value, which would otherwise lead to about a 20 percent larger value of ν. The corresponding N profiles are plotted in figures 54 to 56.
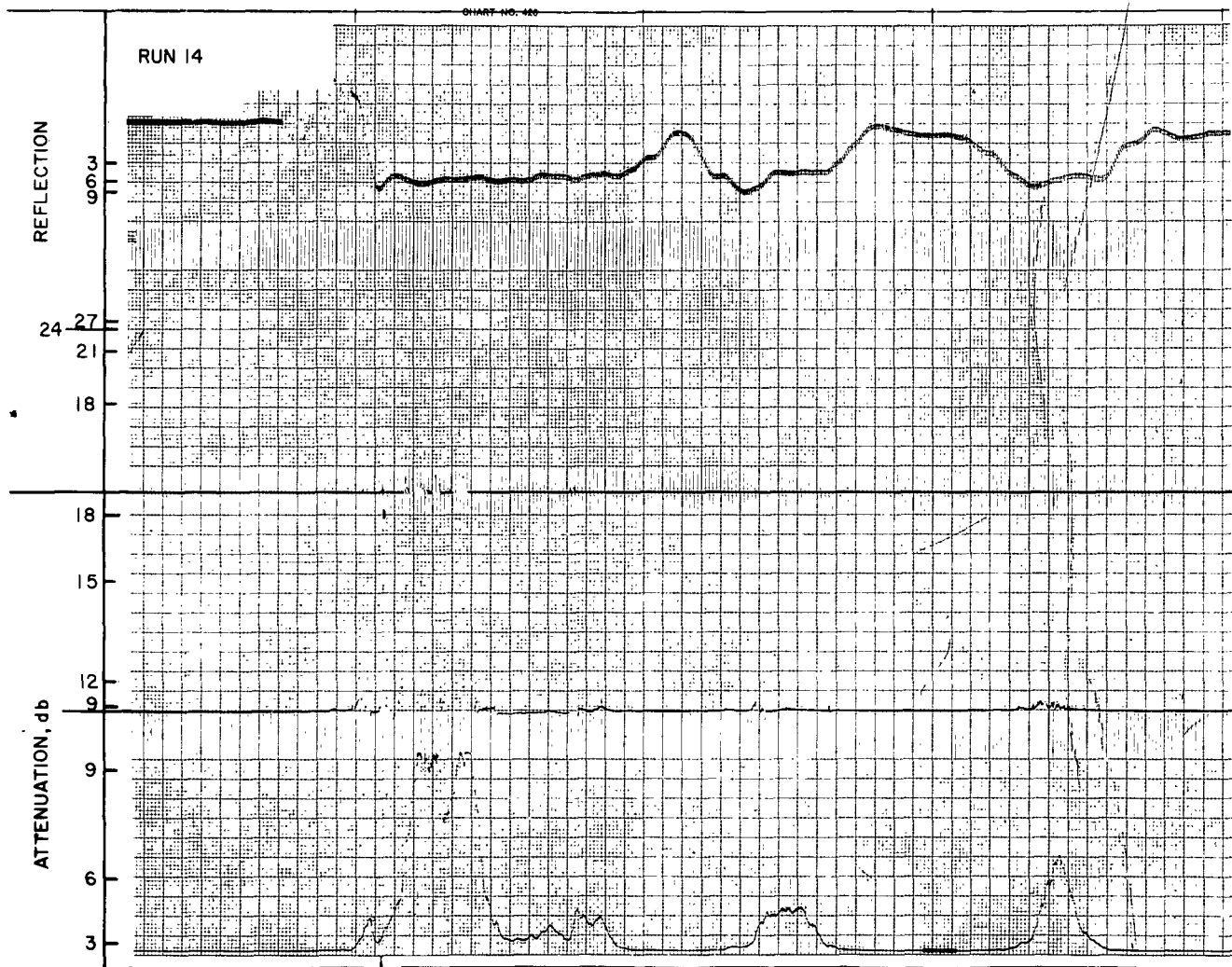
Figure 42 TYPICAL ATTENUATION T[
(Lower channel records 0 to 9 db; sec
to 18 db; third channel records 18 to 2
records reflection signal. Ignition app
uation at beginning of trace. Asymme
plume deflection which can be ascertai
63-2793

TYPICAL ATTENUATION TRACE THROUGH PLUME
channel records 0 to 9 db; second channel records 9
; third channel records 18 to 22 db; upper channel
reflection signal. Ignition appears as large atten-
t beginning of trace. Asymmetry is due to slight
eflection which can be ascertained from motion pictures.)
63-2793
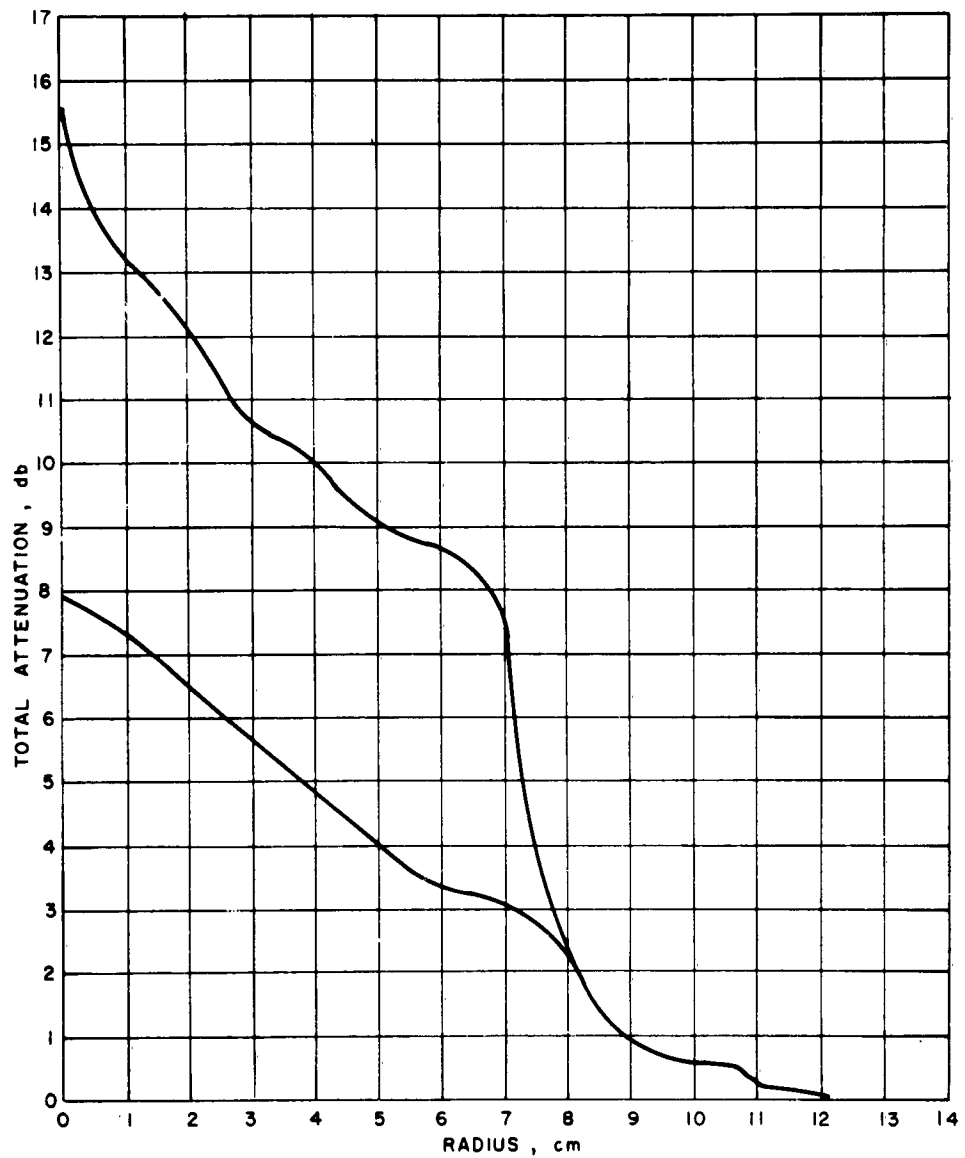
Figure 43 TOTAL ATTENUATION THROUGH Al:CsNO3 PLUME VERSUS
RADIAL DISTANCE (40-INCH STATION)
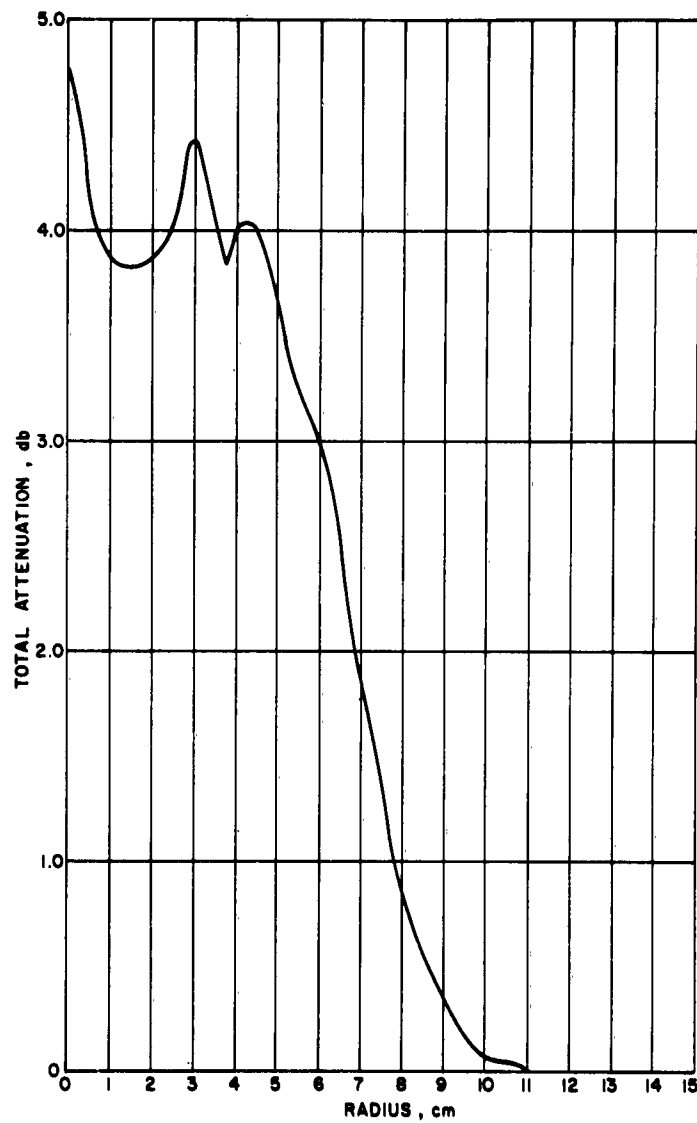
Figure 44 TOTAL ATTENUATION THROUGH Al:CsNO₃PLUME VERSUS
RADIAL DISTANCE (50-INCH STATION)
63-962
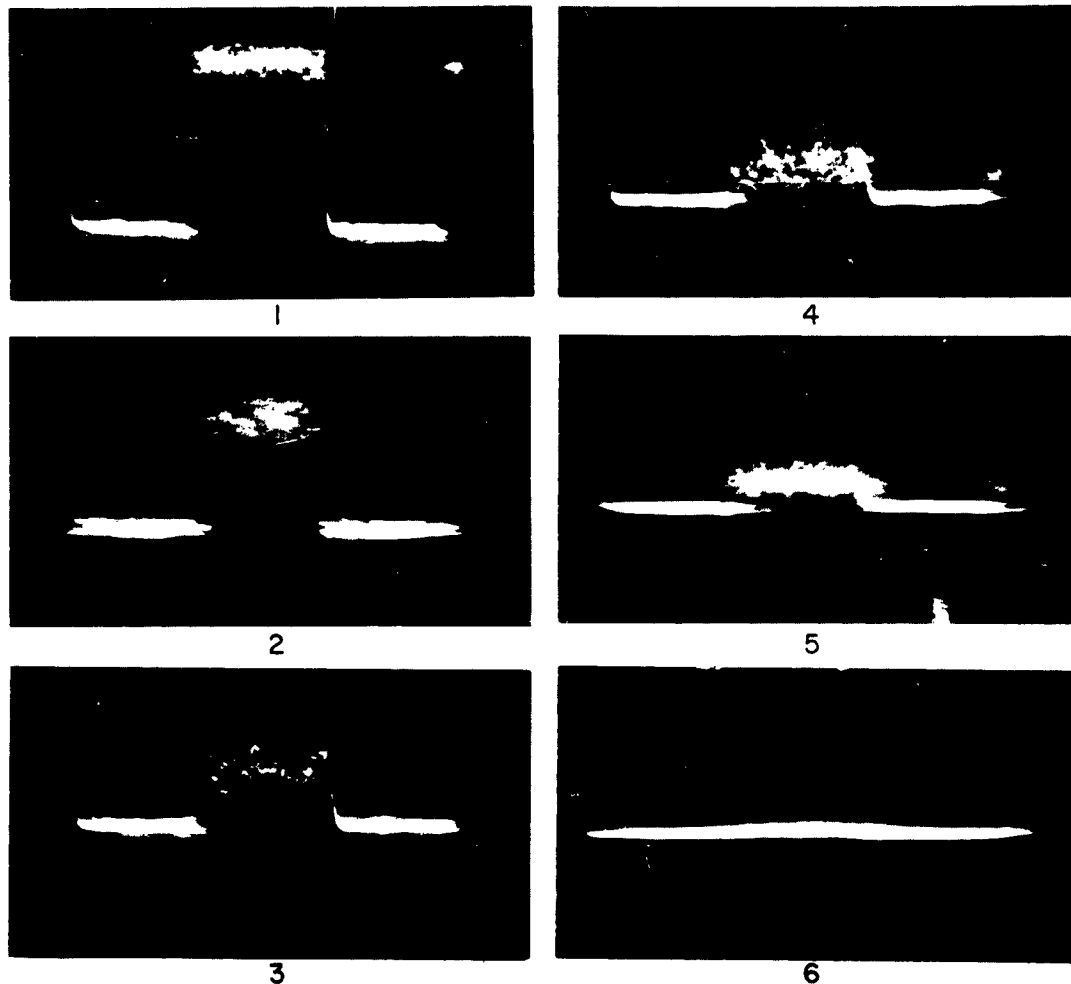
Figure 45   MODULATION ENVELOPE OF RECEIVED 23.5 gc SIGNAL AS
PLASMA BECOMES OVERDENSE
(Note noise level on signal which is characteristic of
solid propellant motor measurements.)
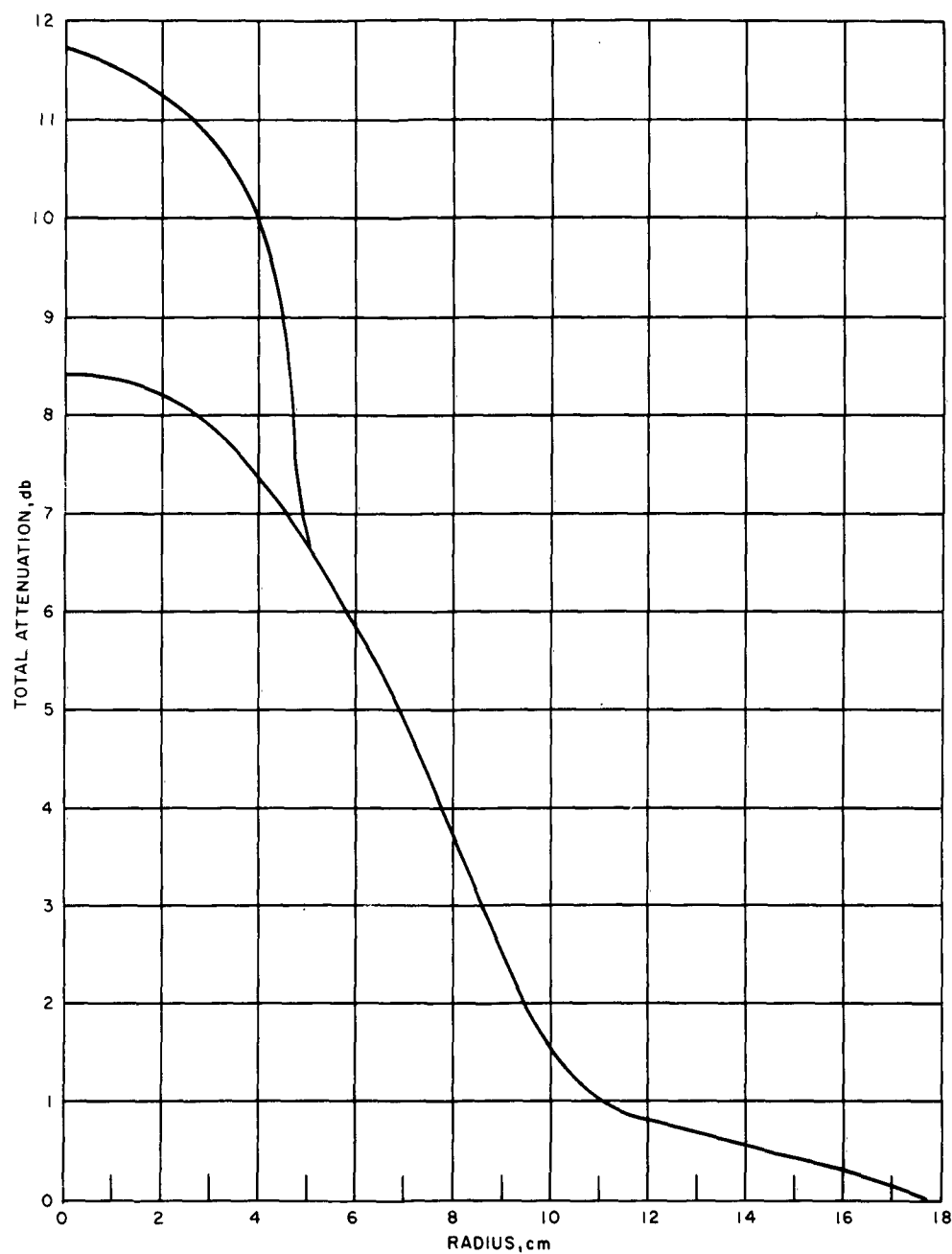
Figure 46 TOTAL ATTENUATION THROUGH Al:KNO$_3$ PLUME VERSUS
RADIAL DISTANCE (20-INCH STATION)
63-2772
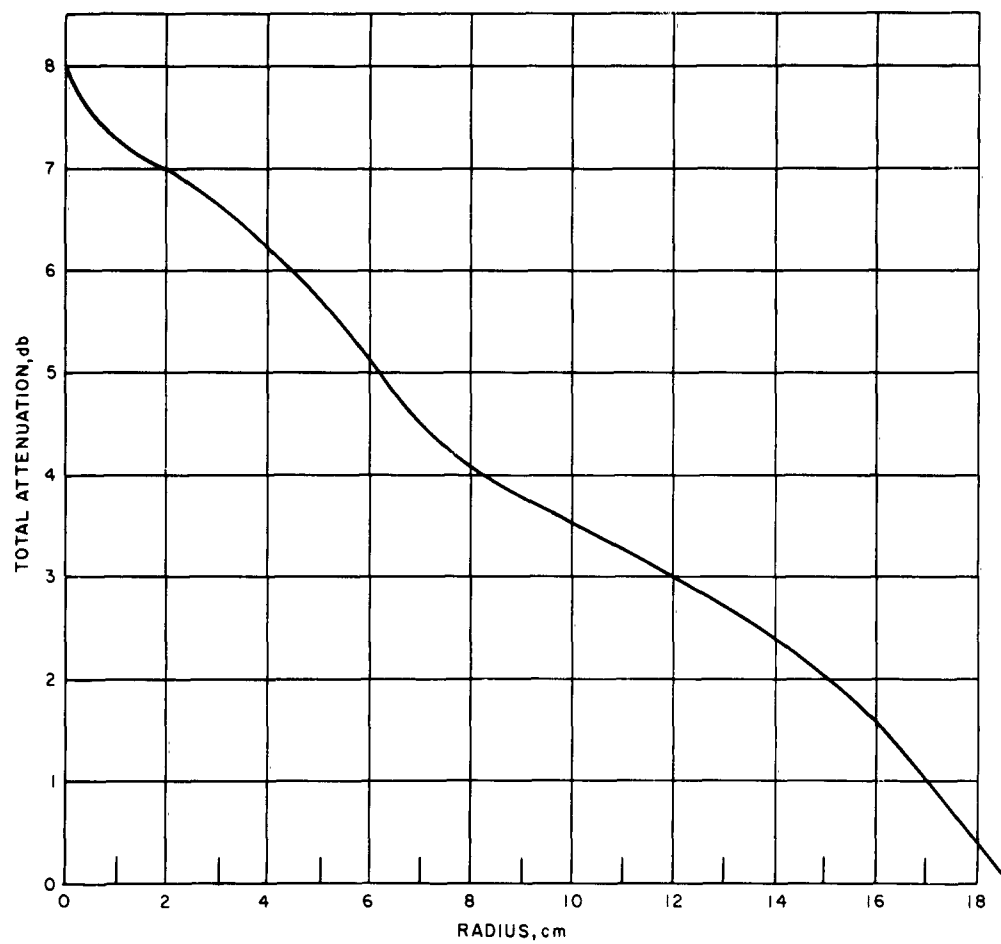
Figure 47   TOTAL ATTENUATION THROUGH Al:KNO$_3$ PLUME VERSUS
RADIAL DISTANCE (40-INCH STATION)
63-2773
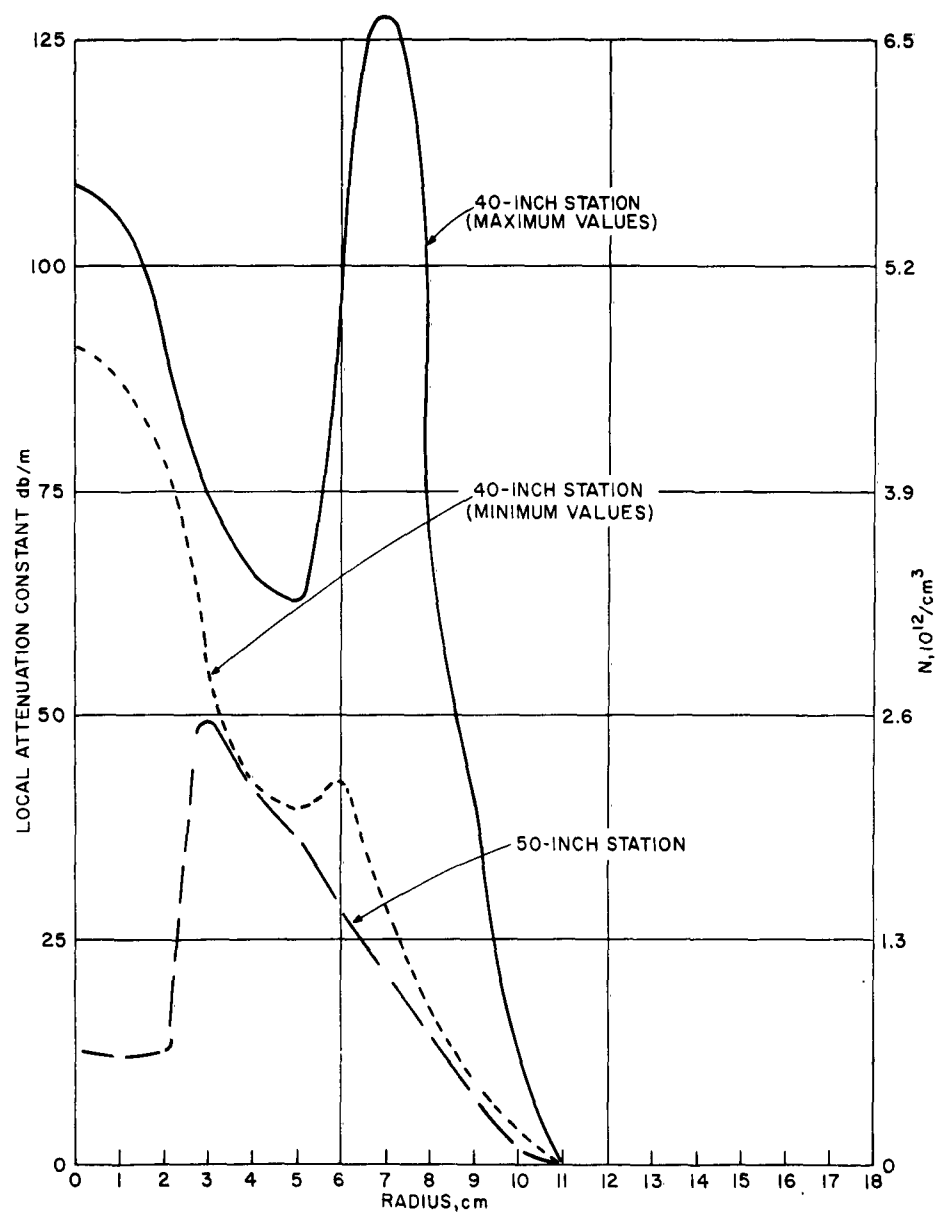
Figure 48   LOCAL ATTENUATION CONSTANT IN Al:CsNO$_3$ PLUME VERSUS
RADIUS AT 40-INCH STATION AND 50-INCH STATION
(Electron density scale on right is based on constant ν .)
63-2774

-70-
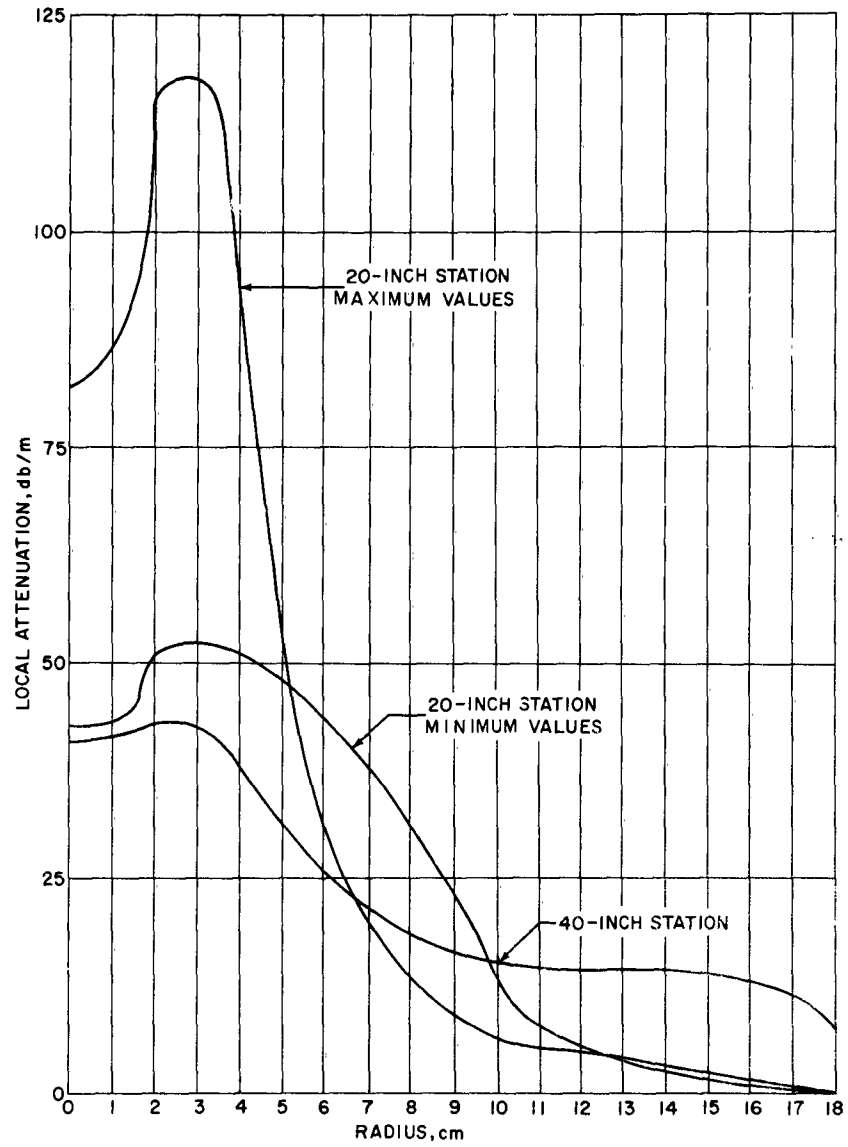
Figure 49 LOCAL ATTENUATION CONSTANT IN Al: KNO_3 PLUME VERSUS
RADIUS AT 20-INCH STATION AND 40-INCH STATION
(Electron density scale on right is based on constant ν.)
63-2775

-71-
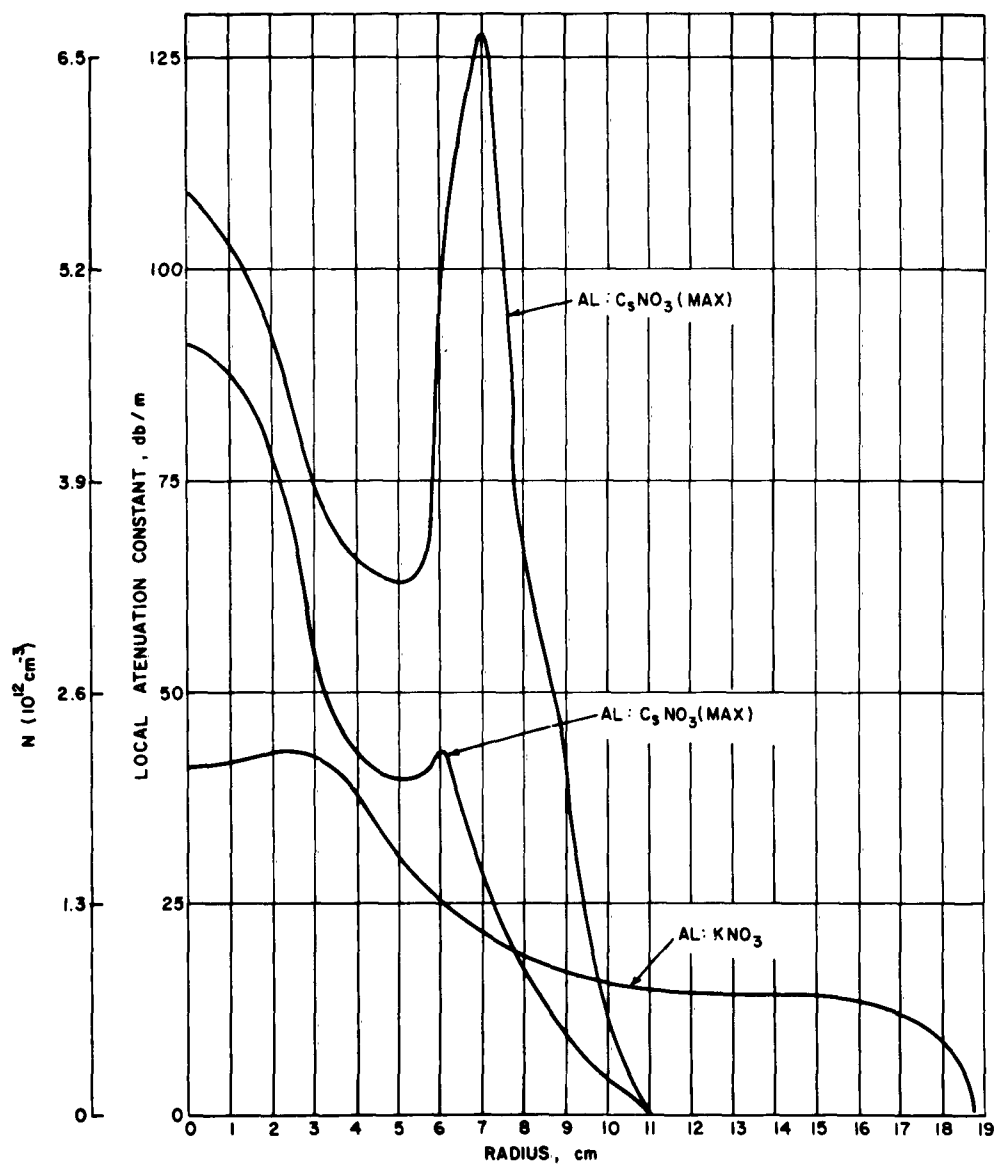
Figure 50 COMPARISON OF LOCAL ATTENUATION CONSTANT VERSUS
RADIUS FOR Al: CsNO$_3$ AND Al: KNO$_3$ PLUMES AT 40-INCH STATION
(Electron density scale on right is based on constant collision frequency.)
63-964

-72-
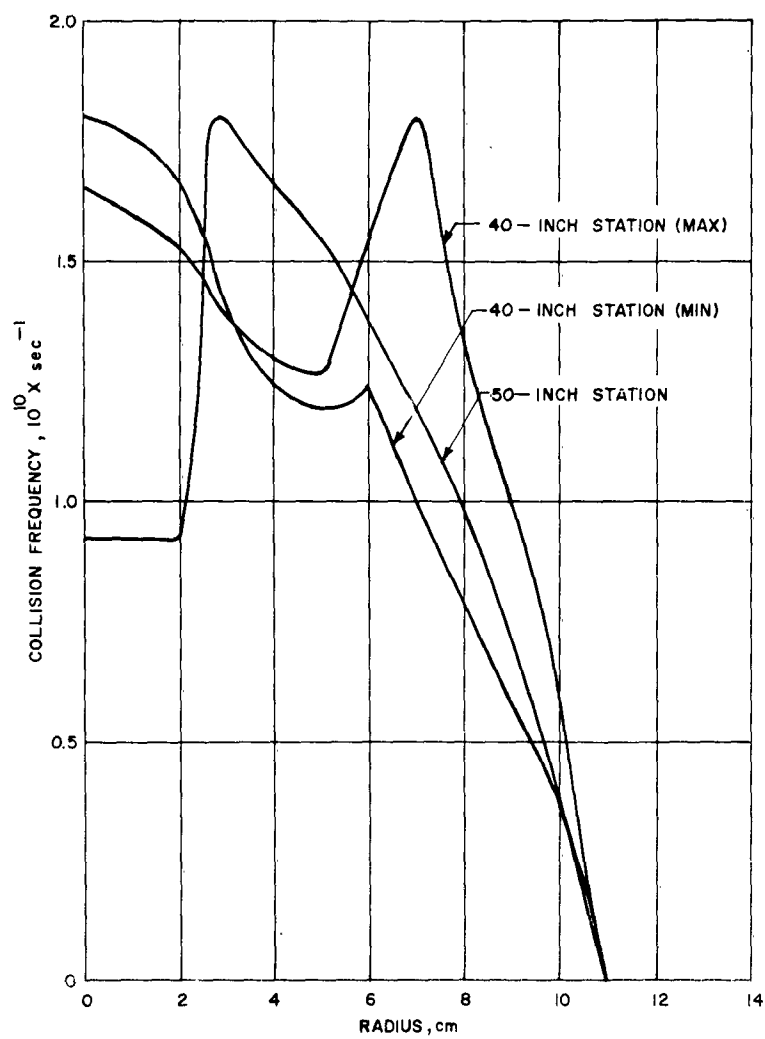
Figure 51 COLLISION FREQUENCY VERSUS RADIUS FOR Al:CsNO₃ PLUME
(See text for assumptions.)
63-965
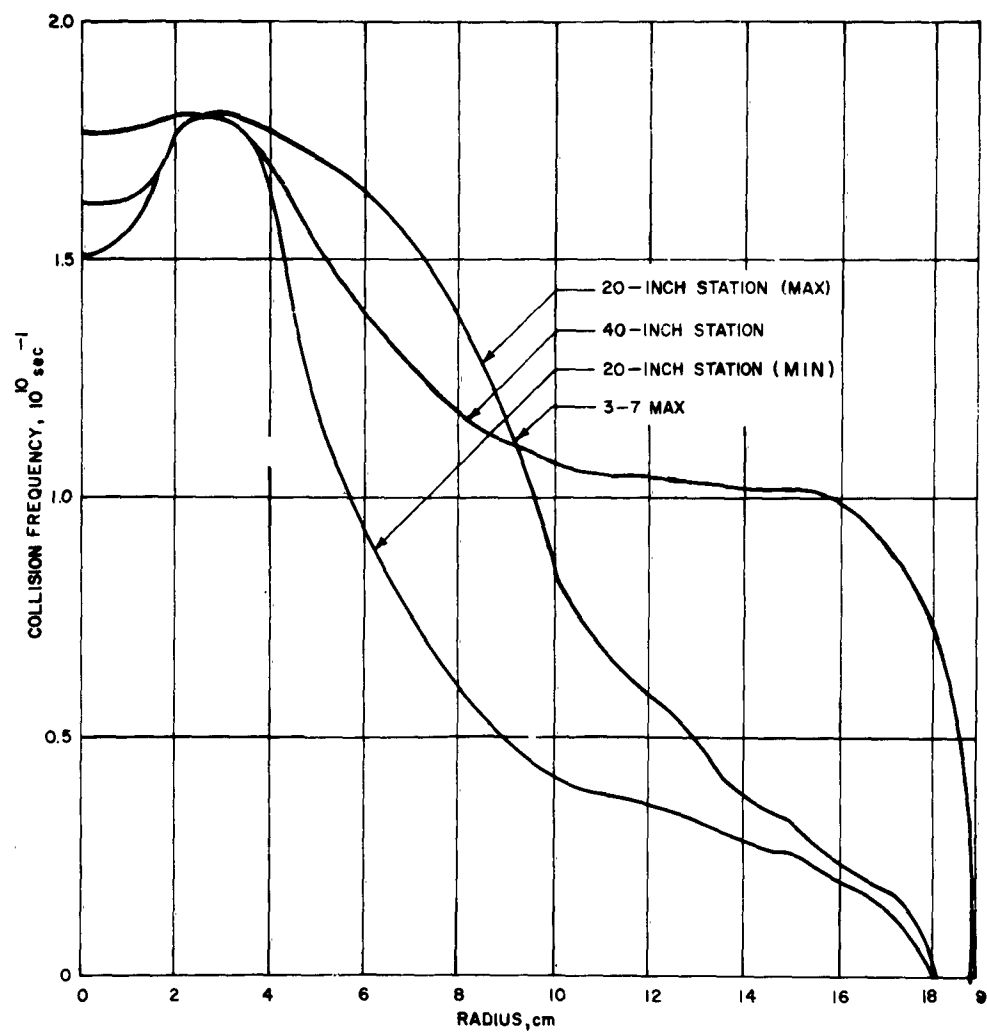
Figure 52 COLLISION FREQUENCY VERSUS RADIUS FOR Al: KNO$_3$ PLUME
(See text for assumptions.)
63-966
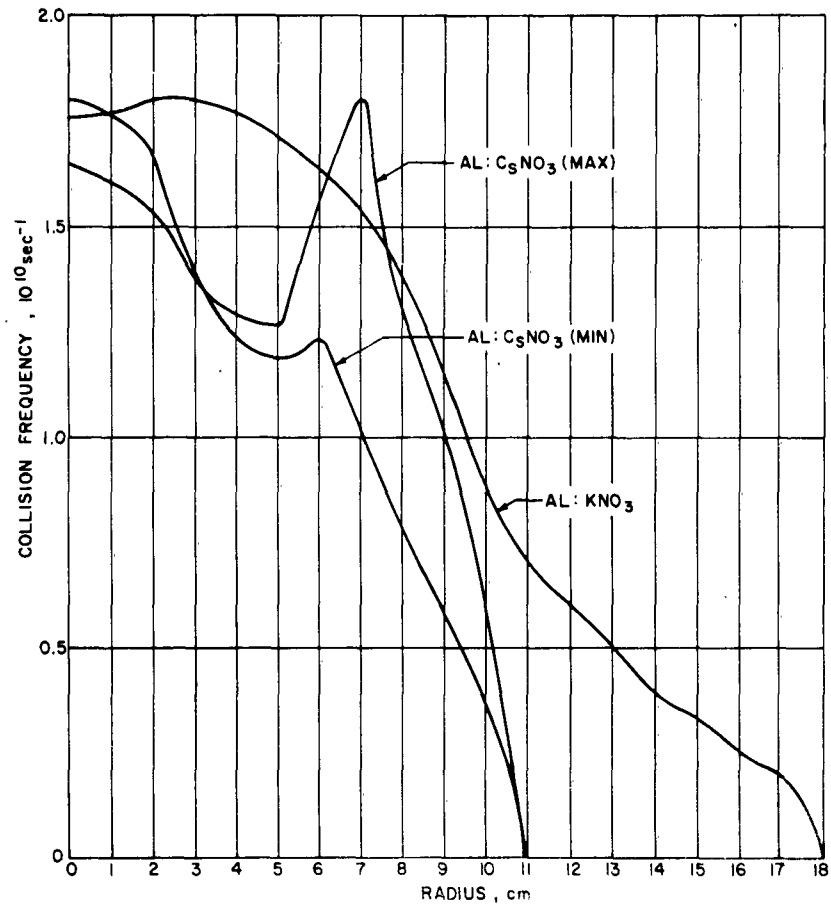
Figure 53 COMPARISON OF COLLISION FREQUENCY AT 40-INCH STATIONS
FOR Al: $CsNO_3$ AND Al: KNO_3 PLUMES
(See text for assumptions.)
63-967
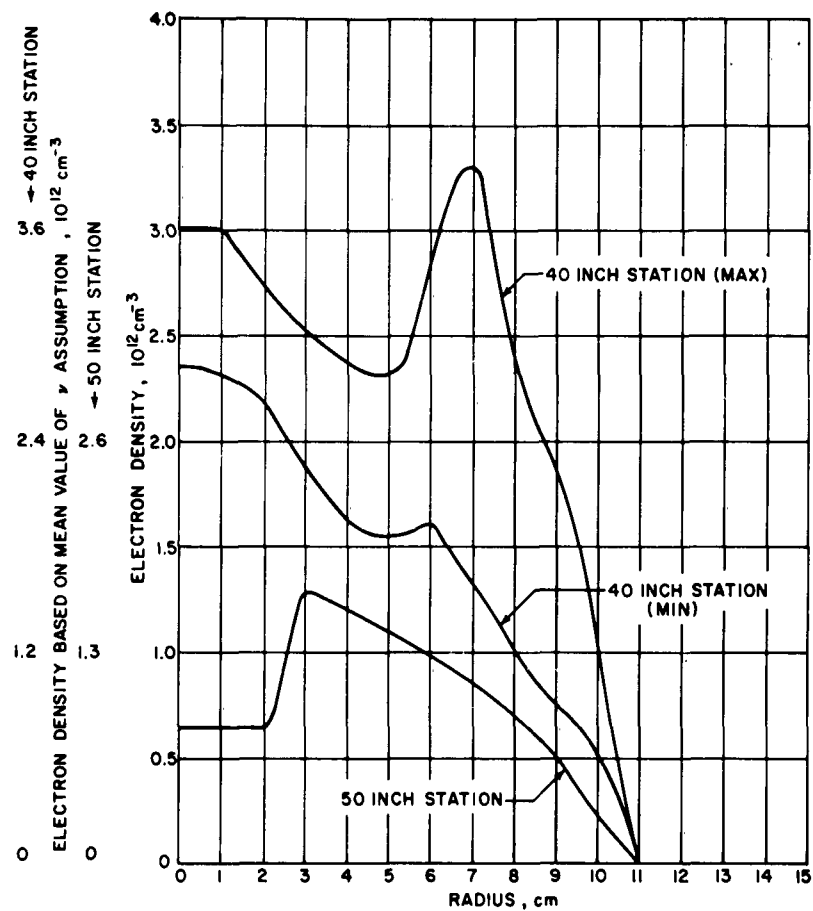
Figure 54 ELECTRON DENSITY VERSUS RADIUS FOR Al: CsNO3 PLUME
(Left scale is based on median ν assumption; right
scales on mean ν assumption.)
63-968
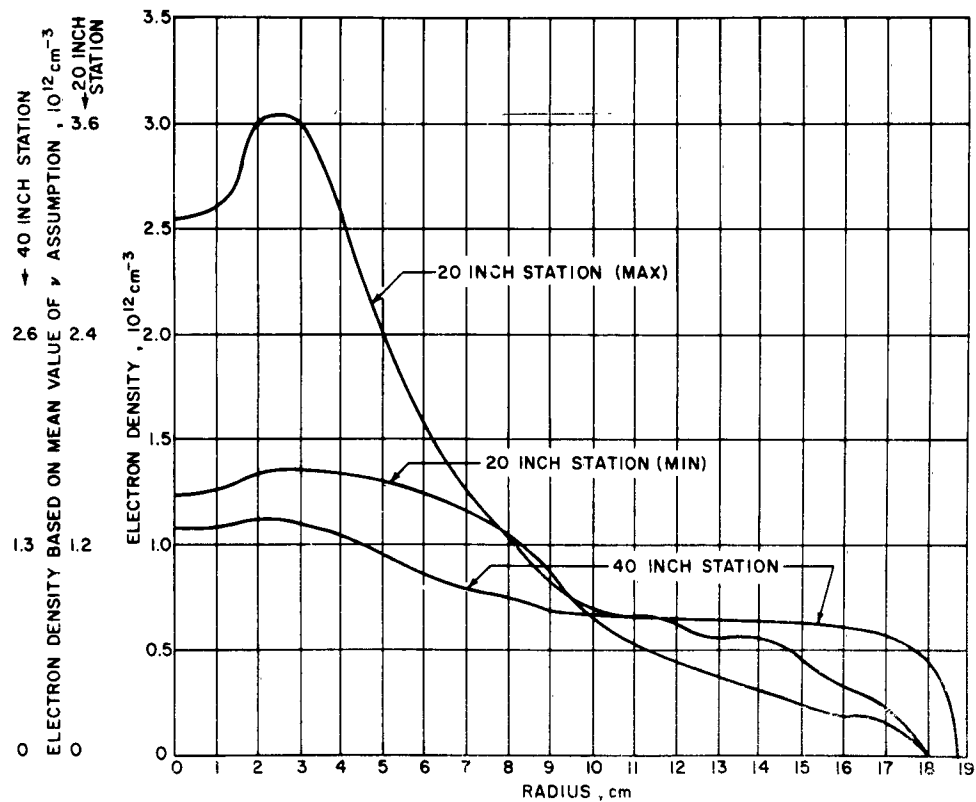
Figure 55 ELECTRON DENSITY VERSUS RADIUS FOR Al: KNO$_3$ PLUME
(Left scale is based on median ν assumption; right
scales on mean ν assumption.)
63-969
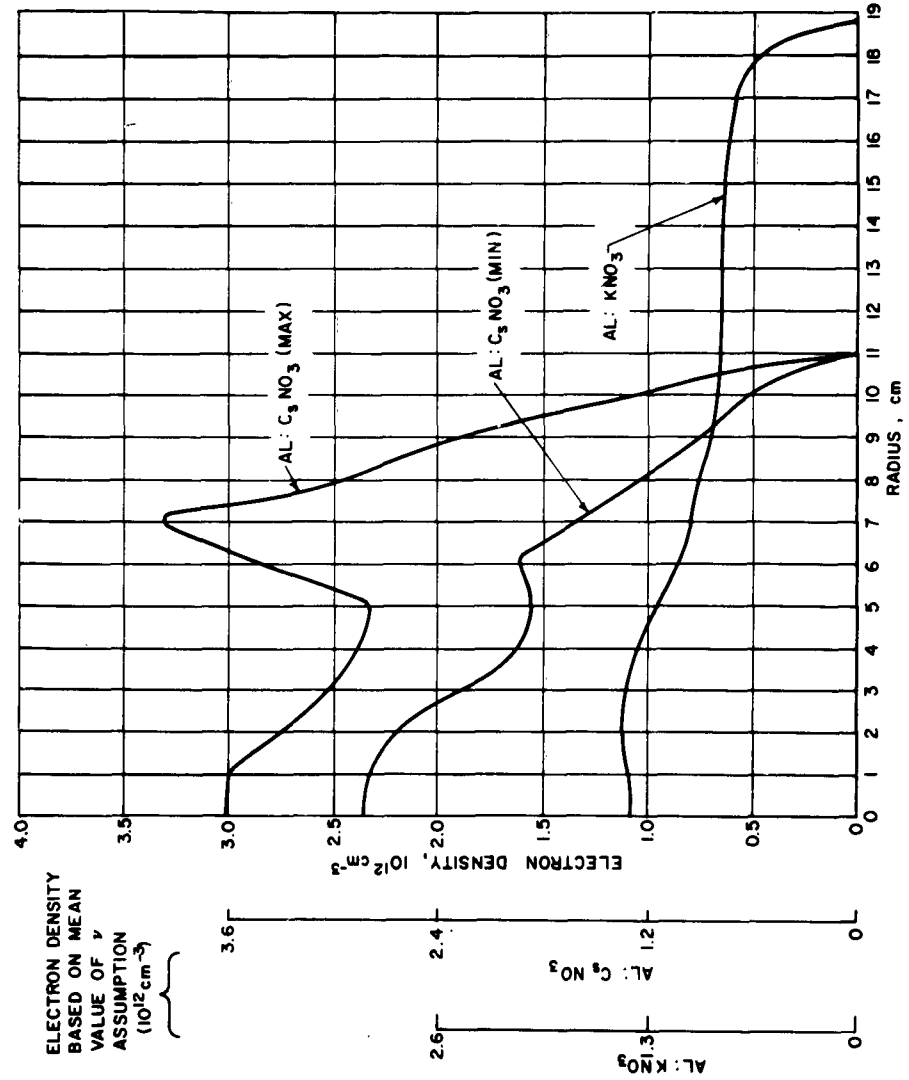
Figure 56 COMPARISON OF ELECTRON DENSITY VERSUS RADIUS FOR
Al: CsNO₃ AND Al: KNO₃ PLUMES
63-970

If a constant ν_n were used, the profile would correspond directly to the α profile. For comparison, an electron-density scale is placed on the right of figures 47, 48, and 49, based on a constant $\nu_n = 9 \times 10^9$ sec^{-1}.

In assuming a collision frequency of 9×10^9 sec^{-1} as the median value, undue emphasis is placed on the peak value of ν_n. This tends to raise the collision frequency and, correspondingly lower N. If 9×10^9 sec^{-1} is taken as the mean value instead, the corresponding electron density is somewhat higher and is shown plotted on the right scales of figures 54 to 56.

In comparing the electron-density values at the 40-inch station (figure 56) it is difficult to decide whether the difference observed is significant, where different motors of dissimilar plume characteristics are being compared. For example, the cesium plume appears to have an electron density roughly three times that of the potassium plume. However, the total number of electrons may well be the same, since the potassium plume occupies a volume roughly three times greater than the cesium plume.

The effect of geometry on electron density must not be underestimated. Assuming an initial electron density, expansion will reduce this number in addition to the effects of recombination. From geometry considerations only, the density will vary inversely as the plume radius squared. Thus, when comparing the Al: $CsNO_3$ plume with the Al: KNO_3 plume, the peak concentration of cesium in the central region may well cause significantly greater electron densities to be observed, when contrasted with the situation of a relatively uniform potassium distribution. Since the measuring system responds to only a finite range of values of N (figure 41), the location in the plume of electron densities of measurable value will vary depending upon plume configuration.

An interesting approximation results from examing the values of electron density obtained. If only an "average" value is of interest, without concern for the plume profile, the peak value of total attenuation (measured along the plume diameter), divided by the diameter, will yield a value of attenuation constant which when substituted in equation (11) (along with the collision frequency), will yield a reasonable "average" electron density. This procedure is used in reducing the data from series II tests listed in table VII.

The effect of removing the binder from the Al: $CsNO_3$ is to raise the electron density at the 40-inch station (lines 3 and 4). This is as expected and points out the probable effects of organic material in the motors. Note here that a greater $\bar{N}$ is achieved at a somewhat lower motor pressure. Significant electron density is recorded at the 70-inch station at the higher motor pressure (line 1 and 4). At lower motor pressures, the electron

density is below the threshold of the microwave measurement at the 70-inch station. Comparison of data between the 40- and 70-inch stations for Al: CsNO3 (lines 1 and 3) is ambiguous, since lower values of $\bar{N}$ are to be expected further away from the motor, particularly in veiw of the motor pressures. This reflects the uncertainty of the instrumentation accuracy in series II.

TABLE VII

SERIES II AVERAGE ELECTRON DENSITY DATA

Station (inches)	Measuring Frequency (gc)	Motor Type	Motor Pressure (psi)	Ambient Pressure (torr)	Total Attenuation (db)	Plume Diameter (meter)	$\bar{\nu}$ (sec^{-1})	$\bar{N} \times 10^{12}$ (cm^{-3})
70	70	Al:CsNO3 (Binder)	300	1	5	0.36	10^{10}	3.1
40	70	Al:KNO3 (Binder)	150	1	$\lesssim 1$	0.36	10^{10}	9.6
40	35	Al:CsNO3 (Binder)	400	1	~ 12	0.36	10^{10}	2.0
40	70	Al:CsNO3	300	1	11	0.36	10^{10}	6.4

4.   Recombination Rate

The loss of electrons in the plasma may be due to attachment or recombination. One or the other of these processes may predominate; however, it is undoubtedly true that both processes are occurring. A plot of N^{-1} versus time will yield a straight line if recombination is present. The slope of this line is the recombination rate. However, attachment may also result in a straight line plot. Therefore, the dominant loss mechanism is not uniquely established, and an "effective" recombination rate (or electron loss rate) R will result. This measurement, a very difficult one under ideal conditions, has yielded values of R for pure cesium ranging over five orders of magnitude, although the accepted value for these conditions is of the order of 10^{-11} cm^3 sec^{-1}.[6-8] These experimental values for pure cesium are of limited validity in the motor plume, since effective recombination is seriously modified by the presence of impurities and temperature. The most valid value for R is that experimentally measured in the motor plume.

The range of distances from the motor, where valid cesium plume measurements can be made, is from 30 to 50 inches. For the potassium motor, it is from 20 to 40 inches. Unfortunately, electron density data exist only at two pôints in these ranges; hence, it is necessary to assume a straight line dependence between N^{-1} and t. The time that the flow takes between measuring stations is based on the aerodynamic calculation of the flow ·

velocity. (See equations (4) to (8)). Thus, cesium will have a flow velocity of approximately 4830 ft/sec and for potassium, u = 8400 ft/sec. This corresponds to a time between 10-inch measuring stations of 0.173 msec for cesium and 0.098 msec for potassium.

The effective recombination rates for the two types of plume are plotted in figure 57. Note that a larger recombination rate is characteristic of both the center of the cesium plume, where interaction with contaminants tends to increase the electron removal rate, and again at the outer edge of the plume, where turbulent mixing with the static air in the chamber again causes the effective recombination rate to rise. The potassium plume does not show this sort of characteristic, indicating that the potassium may be distributed throughout the plume. The potassium data were not carried out to the edge of the plume since the data became ambiguous. The dominant loss mechanism is uncertain since neither the chemistry nor the thermodynamics in the plume are well known. A comprehensive survey of measurements and comparison with theory are presented in appendix B.

5. Sources of Error

The effect of approximating the collision frequency is an important consideration in evaluating the accuracy of the electron density. Examination of figure 41 reveals that the lowest electron density is achieved at a value of ν/f = 6, for any measured value of a. Thus as a increases, the collision frequency may also increase such that for the highest values of a measured ($a \simeq 127$ db/m), and the critical value of ν, the lower electron density limit is approximately 5×10^{11} cm^{-3}. It should be noted, however, that the temperature was so chosen in estimating ν, that both ν_n and ν_i were increased. Furthermore, using this value of a as the average value, and including the radial distribution of a in the ν distribution, further maximized ν. Thus, all the evidence indicates that values of ν used in these calculations are too high by roughly one-half order of magnitude and this means that the calculated values of electron density are more nearly representative of minimum values.

Error is introduced via the recording system, in measuring the total attenuation through the plume. This occurs as the attenuation increases (thereby requiring a higher gain channel to detect the signal), and the noise level from the plasma causes spurious responses. This is first seen in the peak values of the 40-inch cesium data and the 20-inch potassium data where the extreme values are plotted. It is seen that attenuation error affects the electron density results linearly. In the high-attenuation region, this uncertainty amounts to a factor of 2.
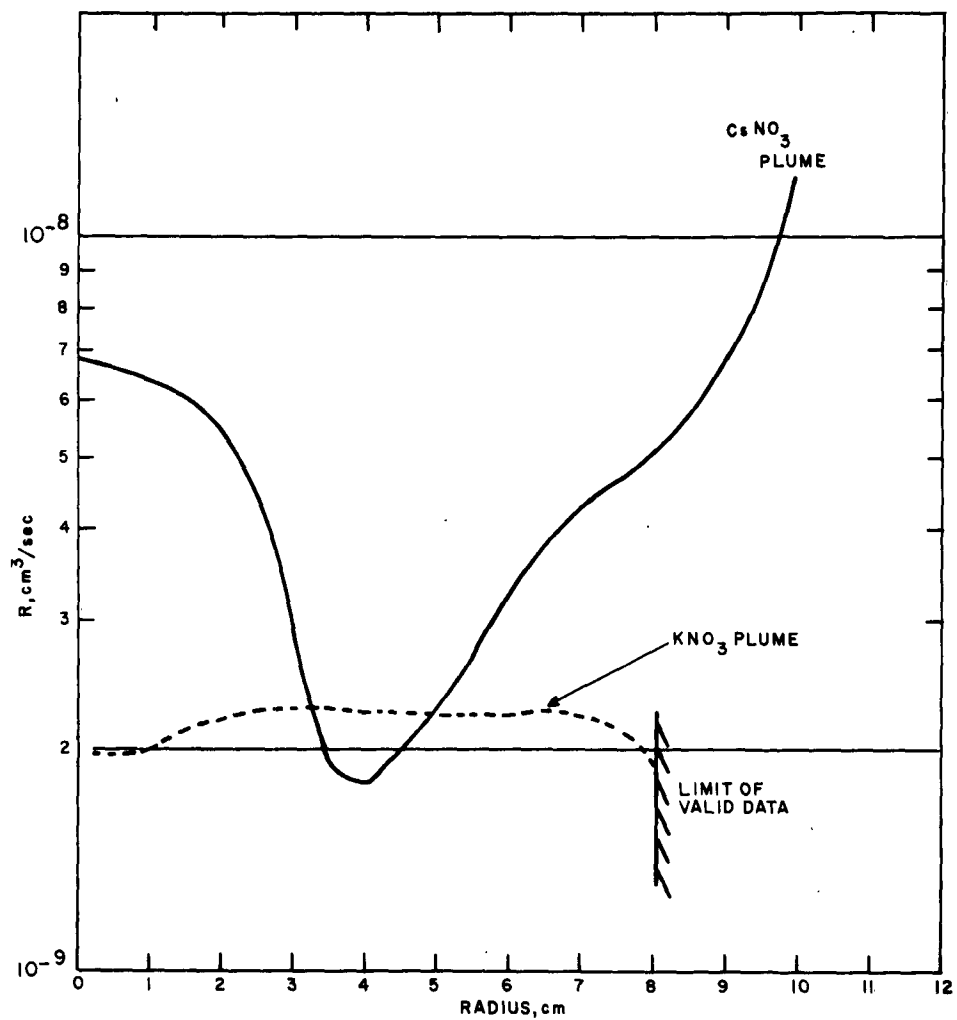
Figure 57 EFFECTIVE RECOMBINATION RATE VERSUS PLUME RADIUS FOR
Al: $CsNO_3$ AND Al: KNO_3 PLUMES
63-2776

System errors are generally less than 3 db and tend to go below this at low attenuation values. This error arises from the limitations involved in a focused-beam system. The lens system serves to focus the electromagnetic energy thereby achieving spatial resolution. Unfortunately, this places the plasma in the near field of the horn-lens system, where the impedance of the plasma boundary couples to the antennas, thereby changing the power radiated from the transmitting system. In an effort to determine the magnitude of this effect, directional couplers were inserted in the transmitting line to sample the reflected signal. The results were spurious, although in general a decrease in reflected signal was observed. This may be explained in either of two ways. The largest amount of reflected signal without plasma originated at the detector; hence, insertion of lossy plasma first attenuated the signal on its way to the detector, and again attenuated the reflected signal as it returned to the transmitting horn and directional coupler. This, however, neglects the reflections which will occur at boundaries in the plasma. These reflections will reinforce or cancel depending upon their phase relations. Since several boundaries exist, some sharp and some graded, the magnitude and phasing of the various reflected waves will depend on both the geometry and steepness of these boundaries. These factors are completely unpredictable since the plasma plume changes with time, and slight changes may produce large phasing effects. Since the reflected signal was approximately 20 db less than the transmitted signal without plasma between the horns, it is doubtful that this reflected signal is of great significance.

In order to estimate the magnitude of this error, an equivalent system was set up to operate at 9 gc, utilizing focused horns. The performance of this system was equivalent to that of the 23.5-gc system except that the focal spot was larger. To substitute for the plasma, two 2-inch planar sheets of microwave absorber (rubberized hair) were assembled, such that the absorbtivity was graded from a minimum value at the outside edges to a maximum value in the center, returning to the minimum value at the far side. Attenutation measurements made at a variety of locations in the beam, and at angles not exceeding 15 degrees off the normal to the beam axis, were consistent, ranging from 29 to 32 db. The reflected signal tended to vary widely, both increasing and decreasing depending upon location and angle of absorber.

Another error which is of importance only when the plasma is near plasma resonance, or the sweep of the plasma past the horns permits grazing incidence, as when the beam reaches the edge of the plume, is that caused by refraction. Energy may be scattered and so lost to the system, causing a higher attenuation reading than might otherwise be the case. Alternatively, the beam might be defocused, again causing an apparent increase in attenuation. This may account for the ambiguous data at the edge of the Al:KNO$_3$ plume. Fortunately both of these effects tend to be minimized; firstly, because the plasma is considrably less dense at the edges where the grazing incidence may occur, hence it does not strongly interact with

-83-

the wave; secondly, even in the most dense plasma regions in the center, approach to plasma resonance quickly creates very large attenuations leading to other, more serious errors. The system rapidly records maximum attenuation, indicating that a higher frequency system must be used. An estimate of the focusing problem is contained in appendix A.

The focal spot-size is approximately 1.5 λ (1.9 cm at 23.5 gc). Thus, spatial resolution is limited by this amount, and radial distances are not known to an accuracy greater than ±8 percent for the cesium motors and ±5 percent for the potassium motors.

The errors introduced by the graphical techniques utilized to obtain electron density have not been analyzed in detail, but an estimate by others indicates that an error of 15 percent is likely.[9]

The overall error in electron density resulting from system operation (excluding the uncertainty of collision frequency), appears not to exceed 75 percent of the peak value determined from the upper values of attenuation data. Where ambiguity does not exist (at lower attenuation values), the limit of error is of the order of 25 percent of the determined value.

IV. CONCLUSIONS

These tests evaluated the operating characteristics of solid-propellant motors in a static environment. Conventional rocket motor properties such as thrust, burning rate, smoothness of burning, mass flow, chamber pressure, and nozzle operation, were all readily determined by conventional observations and measurements.

Analysis of the plume chemistry and aerodynamics is a vastly more difficult problem. Basically, it consists of a mixed flow of different gases and liquid droplets which cool to a solid phase. The solids provide a nozzle blockage which alters the aerodynamic flow, as evidenced by the peculiar annular shock. The dominant optical radiation is from the cesium line spectrum and the aluminum oxide spectrum. A successful potassium spectrum was not obtained. Solids collected from the plume indicated predominantly, $\gamma - Al_2O_3$ with a minimum of crystalline structure in the residue. The large amounts of alkali metal in the plume dominate both the aerodynamic properties and the chemistry. In the case of cesium, the excessive atomic weight, compared with other species, causes a large concentration in the center of the plume with much less at the outer edges, when compared with potassium. However, plume geometry is uncertain, due to both slagging of the nozzle and plume composition.

Measurements of electron density in the plume definitely indicate values of less than 10^{14} cm^{-3} at 20 inches from the motor, with best values of the order of 10^{12} cm^{-3} in the 40- to 60-inch region for cesium and this value of N in the 20- to 40-inch region for potassium. The shorter plume (from an electron-density point of view) for potassium may be due to the fact that the equivalent quantity of potassium occupies a larger volume in the plume (with correspondingly lower density), than does the cesium.

The recombination rate for the cesium plume is higher than measurements based on pure cesium would predict. This is undoubtedly due to contamination by other combustion products which generally tend to raise recombination rates. Values range between 10^{-9} cm^3 sec^{-1} and 10^{-8} cm^3 sec^{-1}. The rate is higher in the center and edge, where one would expect largest contamination. The potassium plume exhibits a reasonably uniform recombination rate over the portion of the plume where measurements were valid, further confirming the distribution argument.

The data obtained on these tests are valid for initial engineering efforts. However, as designs are improved, more detailed measurements will be required. Significant improvement can be obtained in future tests by restricting plume measurements to that area where valid data can be obtained, and performing detailed measurements along the axis at several frequencies simultaneously. In this way, not only can redundant data be obtained, but also it will be possible to more accurately define the collision frequency.

V. REFERENCES

1. Griem, H. R., Stark Broadening of Isolated Spectral Lines from Heavy Elements in a Plasma, to Be Published.

2. Balwanz, W. W., Interaction Between Electromagnetic Waves and Flames, Part 6, NRL Report 5388 (September 1959).

3. Ginzberg, V. L., Propagation of Electromagnetic Waves in a Plasma, Gordon and Breach, New York (1961).

4. Brown, S. C., Basic Data of Plasma Physics, Technology Press of MIT, and John Wiley and Sons, Inc., New York (1959).

5. Freiser, H., Optical and Photographic Investigation of the Flame, Germany Archiv. No. 38/lgk, translated by General Electric Company, Data Folder 85514 (March 1947), ASTIA Doc. 57721.

6. Wada, J. Y., and R. C. Knechtli, Generation and Application of Highly Quiescent Cesium Plasma in Steady State, Proc. IRE (December 1961).

7. D'Angelo, N., Recombination of Ions and Electrons, Phys. Rev. 121 (1961), p. 505.

8. Kuckes, Motley, Hinnov, Herschberg, Recombination in a Helium Plasma, Phys. Rev. Letter, 6, (1961), p. 337.

9. Friedman, R., et al, Study of Electron Generation by Solid Propellant Technique, Atlantic Research Corporation (21 September 1962).

APPENDIXES

A. RAY TRACING THROUGH A PLASMA CYLINDER

B. RECOMBINATION RATES IN THERMAL PLASMAS

APPENDIX A

1. Introduction and Summary

The plume of motor is roughly cylindrical, and the analysis of microwave transmission measurements through a plasma plume necessitates a knowledge of the scattering of microwaves from a cylindrical dielectric. This is a difficult problem, but some insight can be gained by tracing rays through a cylinder, using the simplified assumptions of ray optics. Two cases are treated: 1) a beam focused off the center of the plume along the optical axis, and 2) a beam focused off the center of the plume perpendicular to the optical axis.

2. Index of Refraction

The propagation constant k for a plane wave propagating in a homogeneous neutral plasma has been derived in many sources: [A-1]

$$E = E_o \exp i (kx - \omega t)$$

$$k^2 = \left(\frac{\omega}{c}\right)^2 \left[1 - \frac{\omega_p^2}{\omega^2 + \omega_g^2} + \frac{i \, \omega_g \, \omega_p^2}{\omega \, (\omega^2 + \omega_g^2)}\right] \quad,$$

where

ω_p = plasma frequency

= $5.63 \times 10^4 \sqrt{n_e}$ in rad/sec

n_e = electron density in electrons/cc

ω = signal frequency

ω_g = collision frequency.

The phase constant β is given by $|\text{Re } k|$:

$$\beta = \frac{\omega}{c} \, \frac{1}{\sqrt{2}} \left[1 - \frac{\omega_p^2}{\omega^2 + \omega_g{}^2} + \sqrt{\left(1 - \frac{\omega_p^2}{\omega^2 + \omega_g^2}\right)^2 + \left(\frac{\omega_g \, \omega_p^2}{\omega \, (\omega^2 + \omega_g^2)}\right)^2}\right]^{1/2}$$

The classical index of refraction n derived from the phase velocity is given by:

$$n = \frac{c \, \beta}{\omega}$$

[A-1] Stratton, J.A., Electromagnetic Theory, McGraw-Hill, New York (1941). p 326.

Figures A-1 and A-2 give the index of refraction for various electron densities and collision frequencies. [A-2]

3. <u>Plume Off Center along Optical Axis</u> (figure A-3)

Consider the case where there is a beam focused a distance b from the center of the plume. θ is the cone angle with respect to the optical axis of a ray focused at b.

4. <u>Refraction at First Boundary</u>

In figure A-3

    C   is the center of the circle

    ϕ is the angle of incidence at T

    ϕ' is the angle of refraction

    f   is the focus of the beam

    θ' is the angle at which the beam diverges

    r   is the radius of plasma cylinder.

In $\triangle$ TCF

$$\frac{\sin \phi'}{f} = \frac{\sin (\pi - \theta')}{r} \quad \text{or} \quad f = \frac{r \sin \phi'}{\sin \theta'} \tag{A-1}$$

Using Snell's Law,

$$\sin \phi' = \frac{1}{n} \sin \phi . \tag{A-2}$$

Substituting (A-2) in (A-1)

$$f = \frac{r}{n} \frac{\sin \phi}{\sin \theta} . \tag{A-3}$$

In $\triangle$ bTC

$$\frac{\sin (\pi - \theta)}{r} = \frac{\sin \phi}{b} \quad \text{or} \quad \sin \phi = \frac{b}{r} \sin \theta . \tag{A-4}$$

―――――――――

[A-2] Balwanz, W.W., Interaction Between Electromagnetic Waves and Flames, Part 6, Theoretical Plots of Absorption, Phase Shift, and Reflection.

Substituting (A-4) in (A-3),

$$f = \frac{b}{n} \frac{\sin \theta}{\sin \theta'} \qquad\qquad\qquad\qquad (A-5)$$

In $\triangle bTf$,

$$(\pi - \theta') + \theta + \phi' - \phi = \pi \quad \text{or} \quad \theta' = \theta + \phi' - \phi . \qquad (A-6)$$

To sum up;

$$f = \frac{b}{n} \frac{\sin \theta}{\sin \theta'} \qquad\qquad\qquad\qquad (A-7a)$$

where

$$\theta' = \theta + (\phi' - \phi) \qquad\qquad\qquad\qquad (A-7b)$$

$$\sin \phi = \frac{b}{r} \sin \theta \qquad\qquad\qquad\qquad (A-7c)$$

$$\sin \phi' = \frac{b}{nr} \sin \theta . \qquad\qquad\qquad\qquad (A-7d)$$

5. Refraction at Second Boundary

In figure A-3

β is the angle of incidence at T'

β is the angle of refraction

θ'' is the cone angle at which the beam diverges from the plasma

f' is the apparent focus of the divergent beam.

In $\triangle T'Cf'$

$$\frac{\sin \theta''}{r} = \frac{\sin \beta'}{f'} \quad \text{or} \quad f' = \frac{r \sin \beta'}{\sin \theta'} \qquad (A-8)$$

Using Snell's Law

$$\sin \beta' = n \sin \beta \qquad\qquad\qquad\qquad (A-9)$$

Substituting (A-9) in (A-8),

$$f' = rn \ \frac{\sin \beta}{\sin \theta''} \qquad . \qquad \text{(A-10)}$$

In $\Delta T'Cf$

$$\frac{\sin \beta}{f} = \frac{\sin \theta'}{r} \text{ or } \sin \beta = \frac{f}{r} \sin \theta' \qquad \text{(A-11)}$$

Substituting (A-11) in (A-10)

$$f' = fn \ \frac{\sin \theta'}{\sin \theta''} \qquad . \qquad \text{(A-12)}$$

In $\Delta f T'f'$

$$\theta' + (\beta - \beta') + (\pi - \theta'') = \pi \text{ or } \theta'' = \theta' + \beta - \beta' \quad . \qquad \text{(A-13)}$$

To sum up,

$$f' = fn \ \frac{\sin \theta'}{\sin \theta''} \qquad , \qquad \text{(A-14a)}$$

where

$$\theta'' = \theta' + (\beta - \beta') \qquad \text{(A-14b)}$$

$$\sin \beta = \frac{f}{r} \sin \theta' \qquad \text{(A-14c)}$$

$$\sin \beta' = \frac{fn}{r} \sin \theta' \qquad \text{(A-14d)}$$

Combining the results for the two surfaces, equations (A-7a-d) and (A-14a-d),

$$f = b \ \frac{\sin \theta}{\sin \theta''} = \qquad \text{distance of apparent focus from center of plume,} \qquad \text{(A-15a)}$$

where

θ is the incident cone angle

θ'' is the divergent cone angle given by

$$\theta'' = \theta + (\phi' - \phi) + (\beta - \beta') \quad , \qquad \text{(A-15b)}$$

-92-

where

$$\sin \phi = \left(\frac{b}{r} \sin \theta \right) \tag{A-15c}$$

$$\sin \phi' = \frac{1}{n} \left(\frac{b}{r} \sin \theta \right) \tag{A-15d}$$

$$\sin \beta' = \frac{1}{\sin [\theta + (\phi' - \phi)]} \left(\frac{b}{r} \sin \theta \right) \tag{A-15e}$$

$$\sin \beta = \frac{1}{n \sin [\theta + (\phi' - \phi)]} \left(\frac{b}{r} \sin \theta \right) . \tag{A-15f}$$

6. Sample Calculation (figure A-4)

As an example of the preceding, a sample calculation has been made for the following assumed conditions: a beam, focused at $\flat$ where $\frac{b}{r} = 0.1$, incident at an angle $\theta = 30$ degrees and signal frequency $= 23.5$ gc; $\left(\frac{\omega_g}{\omega} \right) \ll 1.$

TABLE A-1

VALUES OF SAMPLE CALCULATION

n_e (cm^{-3})	n	θ'' (divergent angle)	$\dfrac{\sin \theta}{\sin \theta''}$
10^{11}	0.9927	30° 04'	0.998
5×10^{11}	0.9630	30° 20'	0.990
10^{12}	9244	30° 42'	0.979
2×10^{12}	0.8421	31° 36'	0.954
3×10^{12}	0.7509	32° 48'	0.923
4×10^{12}	0.6468	34° 34'	0.881
5×10^{12}	0.5225	37° 41'	0.818
6×10^{12}	0.3572	45° 29'	0.704
6.5×10^{12}	0.2343	54° 34'	0.614
6.86×10^{12}	0.05	complete reflection	-
6.877×10^{12}	0	-	-

7. Plume Off Center Perpendicular to the Optical Axis (figure A-5)

This case is of particular interest when the plume is being scanned by a focused microwave system. In general, complete ray tracing is difficult. For the general case, it is fairly straightforward to calculate the angle of incidence of a ray, θ', as a function of the distance of the focus from the plume center, b, by the cone angle θ, and the polar angle ϕ.

In the two triangles in the plane of a and b,

$$a = \sqrt{r^2 - (b + f \cos \phi)^2} \quad .$$

(A-16)

In containing a and c,

$$c = \frac{a}{\cos \theta} \quad ;$$

(A-17)

using (A-16)

$$c = \frac{\sqrt{r^2 - (b + f \cos \phi)^2}}{\cos \theta} \quad ;$$

(A-18)

also,

$$f = c \sin \theta \quad ;$$

(A-19)

using (A-18),

$$f = \sqrt{r^2 - (b + f \cos \phi)^2} \ \tan \theta \quad ,$$

(A-20)

which provides a quadratic equation for $\dfrac{f}{r}$:

$$\left(\frac{f}{r}\right)^2 (1 + \cos^2 \phi \tan^2 \theta) + 2\left(\frac{f}{r}\right)\left(\frac{b}{r}\right) \cos \phi \tan^2 \theta \ - \left(1 - \left(\frac{b}{r}\right)^2\right) \tan^2 \theta = 0 \quad .$$

(A-21)

In Δ containing f and d and ϕ,

$$d = f \sin \phi \quad .$$

(A-22)

In Δ containing b, d, e, using (A-22)

$$e^2 = b^2 + f^2 \sin^2 \phi \quad .$$

(A-23)

In Δ containing c, r and e,

$$\cos \theta' = \frac{r^2 + c^2 - e^2}{2\, rc} \qquad .$$

<div align="right">(A-24)</div>

Using equations (A-19 and (A-24)

$$\cos \theta' = \frac{\left(\frac{f}{r}\right)^2 (1 - \sin^2 \phi\, \sin^2 \theta) + \sin^2 \theta \left(1 - \frac{b}{r}\right)^2}{2\left(\frac{f}{r}\right)\sin \theta}$$

<div align="right">(A-25)</div>

Using the value of $\dfrac{f}{r}$ from equation (A-21), this is an equation for θ'.

Two limiting cases given greatly simplified results:

a. $\theta = 0$ degrees (figure A-6)

By a derivation similar to case 1:

In figure A-5,

$$f' \quad = \quad \frac{b \cos \theta}{\cos \theta''} \quad = \text{distance of apparent focus from the center of}$$

the plume

<div align="right">(A-26a)</div>

where

θ is the incident cone angle

θ'' is the divergent cone angle given by

$$\theta'' = \theta - (\phi' - \phi) - (\beta - \beta')$$

<div align="right">(A-26b)</div>

where

$$\sin \phi = \left(\frac{b}{r}\, \cos \theta\right)$$

<div align="right">(A-26c)</div>

$$\sin \phi' = \frac{1}{n} \left(\frac{b}{r}\, \cos \theta\right)$$

<div align="right">(A-26d)</div>

$$\sin \beta' = \frac{1}{\cos (\theta - (\phi' - \phi))} \cdot \frac{b}{r}\, \cos \theta$$

<div align="right">(A-26e)</div>

$$\sin \beta = \frac{1}{n}\, \frac{1}{\cos (\theta - (\phi' - \phi))}\, \frac{b}{r}\, \cos \theta$$

<div align="right">(A-26f)</div>

Note that in this case the divergent cone angle is less than the incident cone angle for $n < 1$.

The cone angle at which complete reflection occurs at the first boundary is given by equation (14) when (n assumed to be less than 1)

$$\sin \phi = 1 = \frac{1}{nr} \, \underline{b} \cos \theta$$

$$\text{or} \cos \theta = \frac{n}{b/r} \quad .$$

(A-27)

b. $\theta = 90$ degrees (figure A-6)

As a limiting case of the general derivation for case 2,

$$\cos \theta' = \sqrt{1 - \left(\frac{b}{r}\right)^2} \, \cos \theta$$

(A-28)

Complete reflection occurs at $\sin \theta' = n$ or

$$\cos \theta = \sqrt{\frac{1-n^2}{1 - \left(\frac{b}{r}\right)^2}}$$

(A-29)

For

$$\theta = 0 \text{ reflection occurs when } \frac{b}{r} = n$$

(A-30)

For

$$b = 0 \text{ reflection occurs when } \cos \theta = \sqrt{1-n^2}$$

(A-31)

8. Cone Angles for Complete Reflection (figure A-6)

The cone angle at which complete reflection occurs is shown versus the fractional distance of the focus from the center of the plume for various electron densities in two cases: $\phi = 0$ degrees for the upper half of the graph, and $\phi = 90$ degrees, the lower half of the graph. Note that the scale of θ is inverted in the lower half of the graph. The two graphs are plotted together in this fashion for ease in identifying the region of complete reflection, which is to the lower right of any curve. Note that the results are symmetric in θ and b for both cases. The electron densities given are computed for the case $\left(\frac{\omega_g}{\omega}\right) \ll 1$

and a signal frequency of 23.5 gc. This graph may be applied to the general case by referring to the corresponding indices of refraction in table A-1.

9. Regions of Complete Reflection (figure A-7)

Qualitative sketches of the region of complete reflection are shown. The points of intersection of the curves with the axis are given by equations (13) and (15). The remainder of the curves are an estimate of the expected form of the solution of equation (11) for constant θ' (determined by n) and $\frac{b}{r}$. The graphs are best visualized as looking down a cone of rays focused at the center of each graph.

Figure A-1 INDEX OF REFRACTION FOR VARIOUS ELECTRON DENSITIES
AND COLLISION FREQUENCIES
63-2786
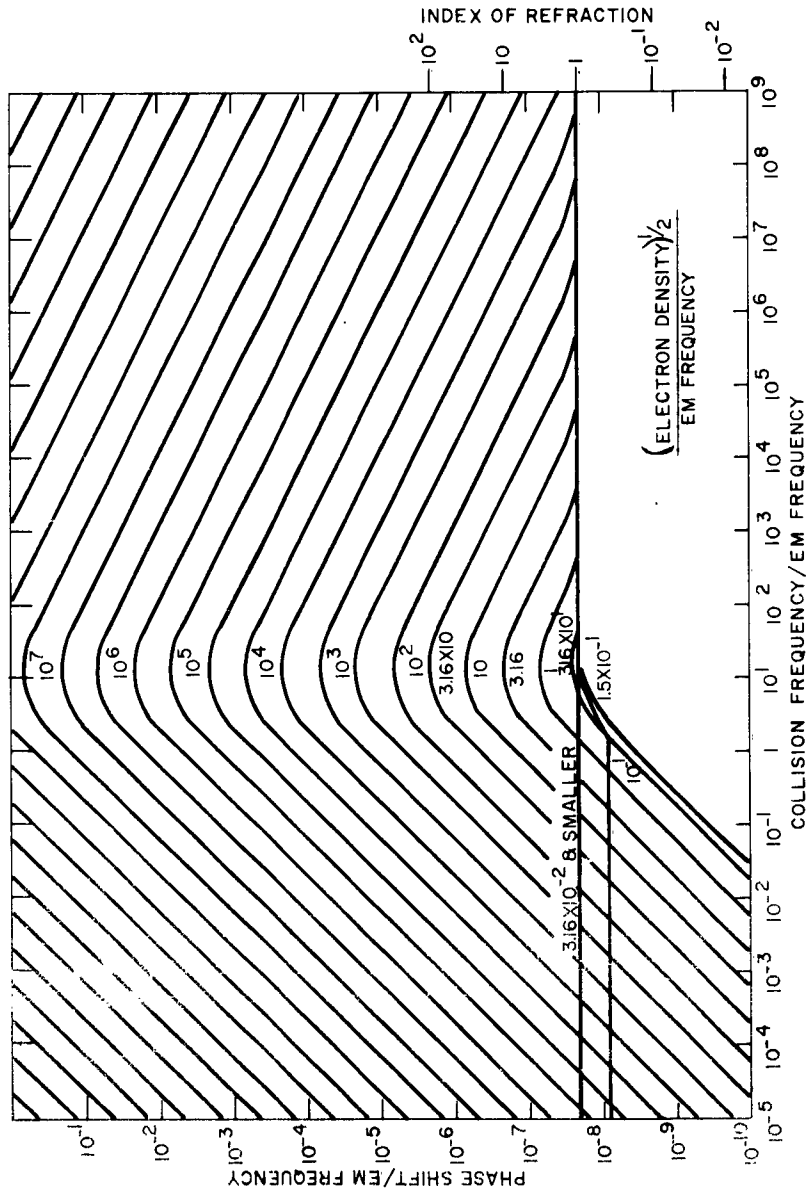
Figure A-2 INDEX OF REFRACTION FOR VARIOUS ELECTRON DENSITIES
AND COLLISION FREQUENCIES
63-2787
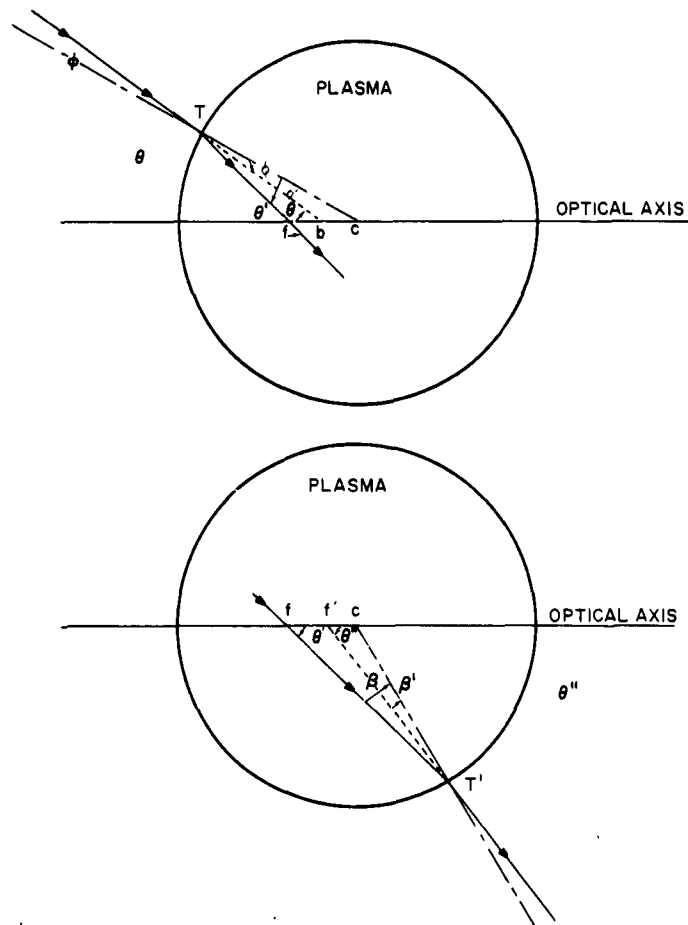
Figure A-3 PLUME OFF CENTER ALONG OPTICAL AXIS
63-2788
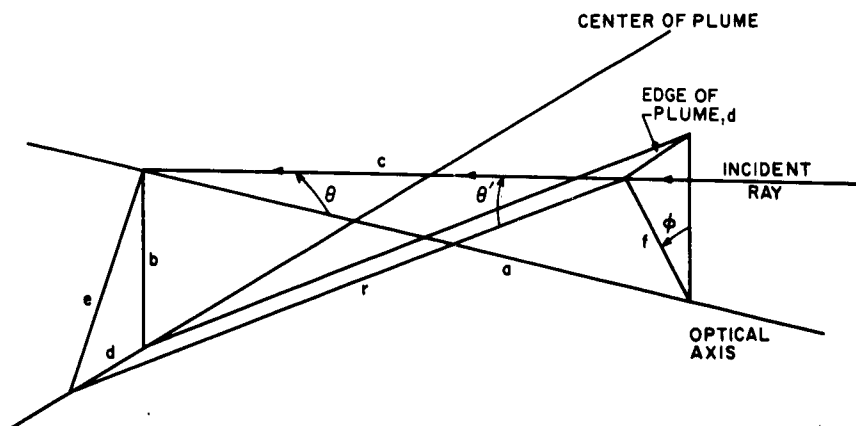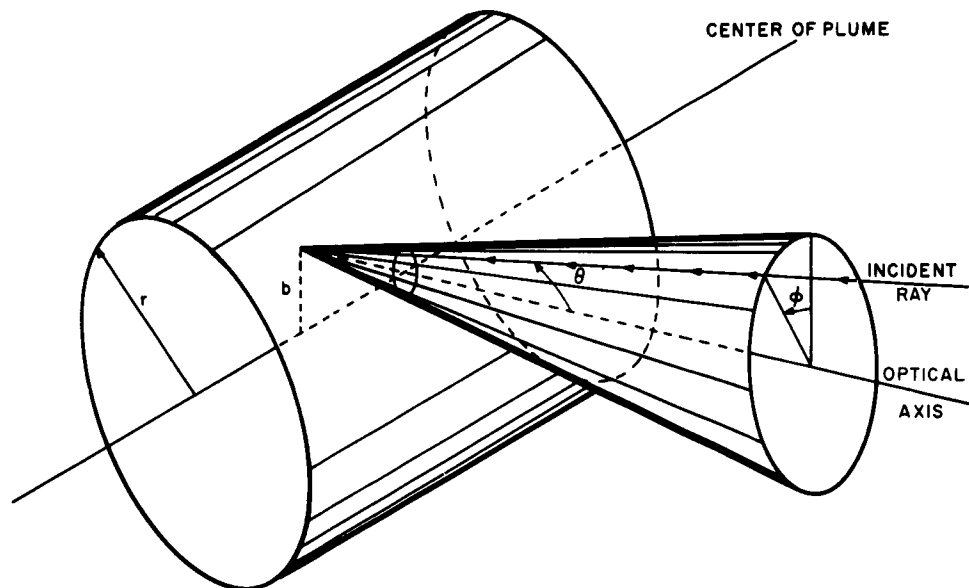
Figure A-4 PLUME OFF CENTER PERPENDICULAR TO THE OPTICAL AXIS
63-2789
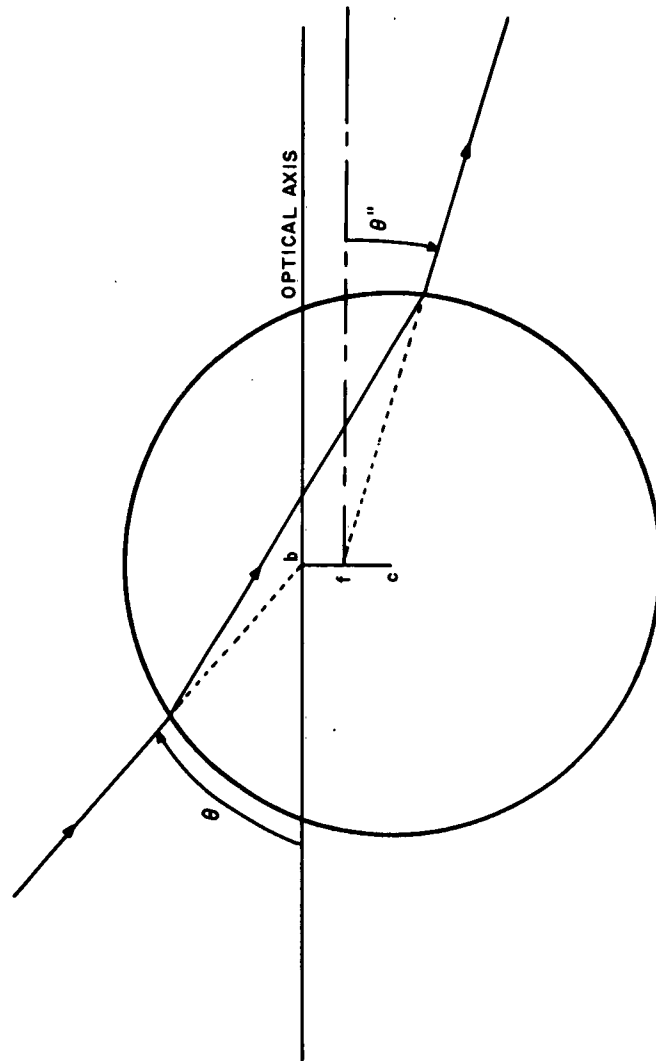
Figure A-5 PLUME OFF CENTER PERPENDICULAR TO OPTICAL AXIS. $\phi = 0°$

63-2790
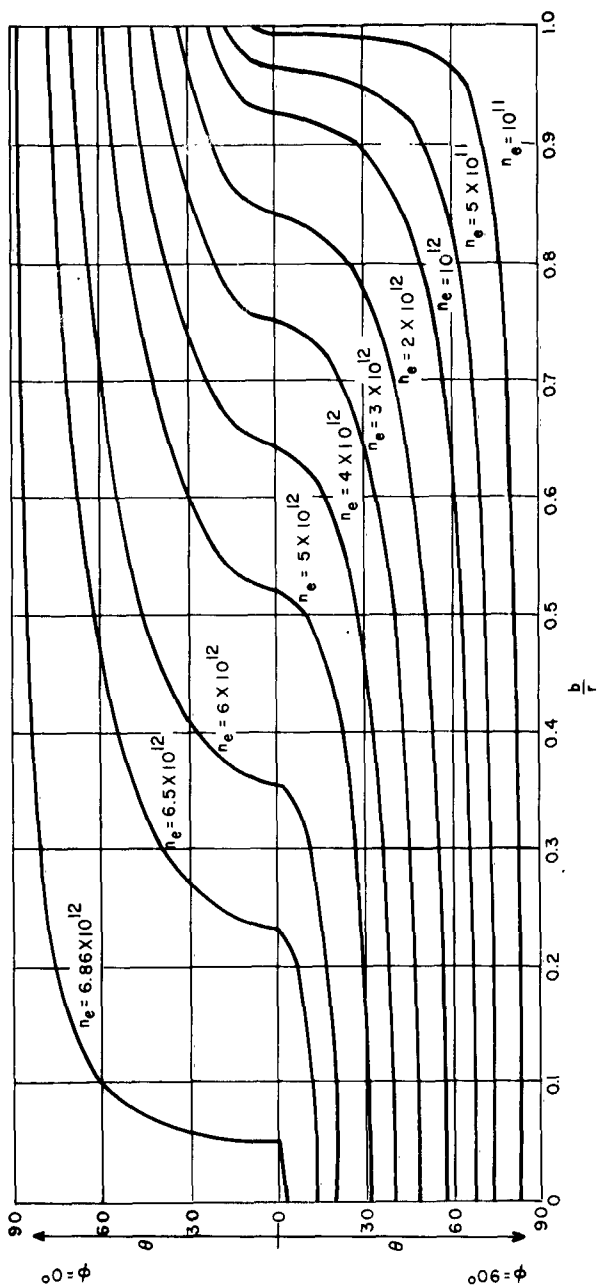
Figure A-6 CONE ANGLES FOR COMPLETE REFLECTION
63-2791

n= 0.7   n=0.3

$\frac{b}{r}$ = 1

$\frac{b}{r}$ = 0.7

$\frac{b}{r}$ = 0.3

$\frac{b}{r}$ = 0
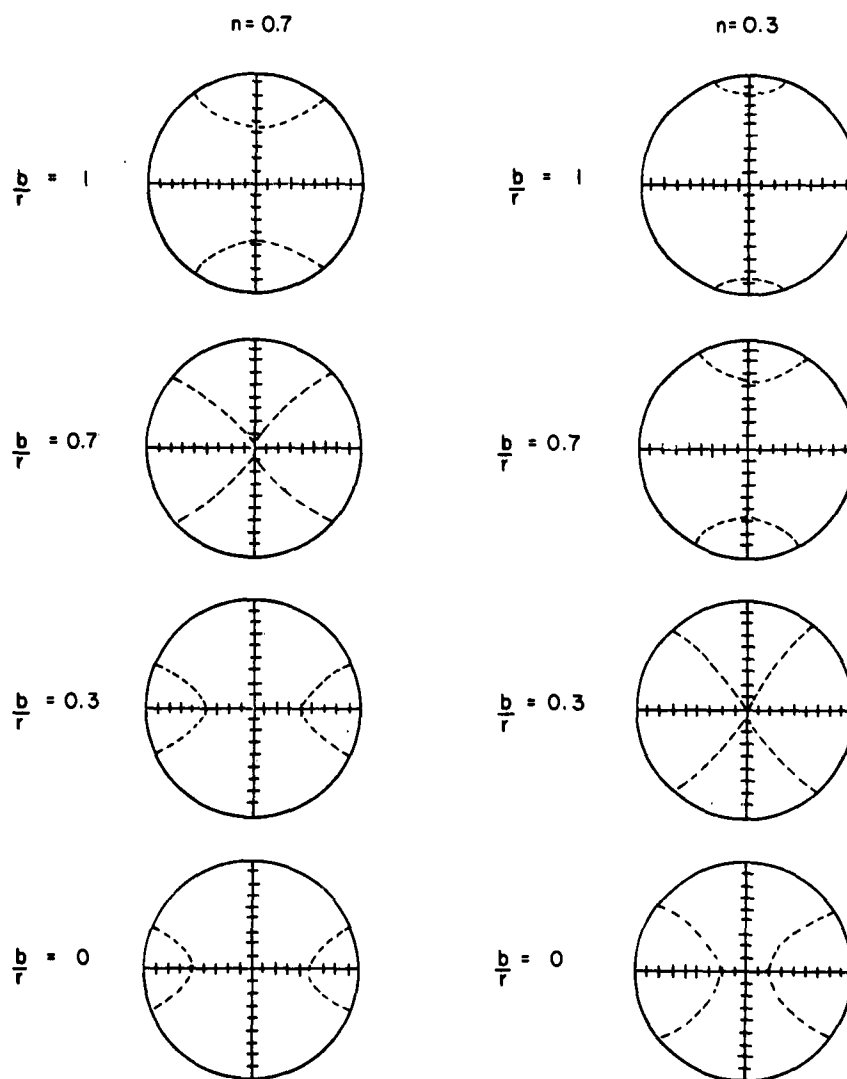
Figure A-7 REGIONS OF COMPLETE REFLECTION
63-2792

APPENDIX B

RECOMBINATION RATES IN THERMAL PLASMAS

The rate of cleanup of electrons in the expanding plasma is determined by recombination and diffusion rates. For the ion-generator experiments, in the region of laboratory measurement, diffusion need not be considered, since diffusion times are longer than the millisecond flow time. Electron-ion recombination processes have been investigated by several observers (see references). For alkali ions, recombination rates are found to be several orders of magnitude slower than for recombination in air, or hydrocarbon flame measurements. This is attributable to the difference in mechanism. The alkali ion process is a three body reaction:

$$e^- + e^- + A^+ \to A + e^- ,$$
(B-1)

while the typical complex ion recombination is a dissociative system,

$$NO^+ + e^- \to N + O$$
(B-2)
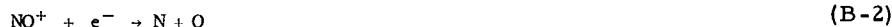
The latter type of reaction proceeds faster, since only two body collisions are necessary to effect recombination. This effect is dramatically demonstrated in the measurements of ionization in alkali metal seeded flames. King[1] showed in hydrocarbon-air flames that the recombination coefficient decreased to

10^{-10} $\dfrac{cc}{ion-sec}$ from 10^{-7} $\dfrac{cc}{ion-sec}$, when cesium and potassium metal salts were added to the flame. This confirmed earlier observations by Sugden and Knewstrubb[2] using sodium and lithium salts.

Thus, the phenomena of slow recombination in thermal alkali, metal plasma has been confirmed and reconfirmed using many different types of apparatus including flames, arc discharges, plasma beams, rocket motors, and cold plasma machines. In table B-I are listed the measured or calculated rates of recombination from seven of these sources. Where possible, the electron temperature and density are shown. As indicated, most of the results tabulated are for cesium and/or potassium plasma; however, the D'Angela[3] (calculated) hydrogen ion and Kuckes, et al[4], helium ion recombination rates are also included. These latter results are presented by the authors with a quantitative model based on electron-electron-ion recombination, with radiative cascading between excited states. In this model, both temperature and ion density dependence of the recombination process are developed. The applicability of this model to the cesium ion recombination process is subject to criticism. However, the electron-electron-ion recombination step appears attractive, and an attempt was made to correlate the measured rates on that basis.

TABLE B-1

COMPARISON OF PUBLISHED RECOMBINATION RATES

Observer	Reference	Gas	Electron Density n_e (cm⁻³)	Electron Temperature T_e (°K)	Recombination Rate α $\left(\dfrac{cm^3}{electron\text{-}sec}\right)$	Normalized Rate Coefficient α_0	Method
Mohler	7	Cs	10^{12}	1200°	$3.4(10^{-10})$	$10.5(10^{-15})$	Plasma arc
Wada and Knechtli	5	Cs	$4(10^{12})$	2000°	$3(10^{-11})$	$1.7(10^{-15})$	Cold plasma device
D'Angela and Rynn	6	Cs K	$5(10^{11})$	2300°	$3.5(10^{-10})$	$50(10^{-15})$	Q-Machine (cold plasma device)
I. R. King	1	Cs K	-	1970°	$3.5(10^{-10})$		Propane air flame positive ion probe
D'Angela (calculated)	3	H	$10^{13} \rightarrow 10^{12}$	$1000° \rightarrow 10,000°$	$(10^{-10}) \rightarrow$ $2.5(10^{-13})$	$0.64(10^{-15})$ $1.6(10^{-15})$	Theoretical
Kuckes, et al.	4	He		~250°	(10^{-9})	$4.5(10^{-15})$	Plasma decay helium afterglow in stellarator
Avco NRL	This report	Cs K	10^{12}	500°		$0.63(10^{-15})$ $3.6(10^{-15})$	Rocket motor

The stated reaction velocity equation from Kuckes, et al: is given by:

$$\frac{dn_e-}{dt} = -(4.5)\ (10^{-15})\ \left(\frac{300}{T}\right)^{2.5}\ N_e-^{2.5}\quad \frac{\text{electron}}{cc}\ \left(\frac{1}{\text{sec}}\right) \tag{B-3}$$

Or, written in the form of a second order process:

$$\frac{dn_e-}{dt} = -\left[(4.5)\ (10^{-15})\ \left(\frac{300}{T}\right)^{2.5}\ \sqrt{n_e-}\right]\ n_e^2- \quad . \tag{B-4}$$

The second order rates given by the respective authors have been correlated on the basis

$$a = a_o\ \left(\frac{300}{T}\right)^{2.5}\ \sqrt{n_e-} \tag{B-5}$$

or

$$a_o = \frac{a}{\sqrt{n_e-}}\ \left(\frac{T}{300}\right)^{2.5} \quad . \tag{B-6}$$

This "normalized" rate coefficient, a_o, is shown itemized in table B-I. The ratio of maximum to minimum values $\dfrac{a_o\ (\text{max})}{a_o\ (\text{min})} \sim 80$ is comparable to the nonnormalized $\dfrac{a\ (\text{max})}{a\ (\text{min})}$. Uncertainties in experimental technique are responsible for some of these variations. Note that the Wida-Knechtli[5] measurement differs from the D'Angela-Rynn[6] value of a by only a factor of 3 although the ion densities differ by a factor of 40. These two normalized rates differ by a factor of 50.

Without the D/Angela-Rynn value, $\dfrac{a_a\ (\text{max})}{a_o\ (\text{min})} = 15$.

The flame measurements of King may be influenced by hydroxide formation. The chemistry of cesium ion cleanup can be expressed by the following rate equation:

$$\frac{d[C_s+]}{dt^m} = -k_1\ [e^-]\ [C_s+]\ [M]\ -k_2\ [C_s+]\ [OH-]\ [M]\ , \tag{B-7}$$

or

$$\frac{d[C_s+]}{dt} = -\{k_1\ [e-]\ [M]\ +\ k_2\ [OH^-]\ [M]\ \}\ [C_s+]\ . \tag{B-8}$$

Thus, in the flame, one cannot be certain that the measurement of ion concentration decay yields the electron ion-recombination rate. However, it is clear that the faster process will dominate. So that if $[e^-] \sim [OH^-]$, $k_1 \leq k_2$. So that the flame measurement provides an upper bound on the electron ion recombination rate.

REFERENCES

1. King, I. R., Recombination Rates of Alkali Metal Ions, J. Chem. Phys. 36, 553, (1962).

2. Knewstrubb, P., and T. Sugden, Observations on the Kinetcs of the Ionization of Alkali Metals in Flame Gases, Trans. Faraday Soc., 54, 372 (1958).

3. D'Angelo, N., Recombination of Ions and Electrons, Phys, Rev., 121, 505 (1961).

4. Kuckes, A., R. Motley, E. Hinnov, and J. Hirschberg, Recombination in a Helium Plasma, Phys. Rev. Letters, 6, 337 (1961).

5. Wada J., and R. Knechtli, Generation and Application of Highly Ionized Quiescent Cesium Plasma in Steady State, Proc. IRE (December 1961).

6. D'Angelo N., and N. Rynn, Diffusion and Recombination of a Highly Ionized Cold Plasma in a Magnetic Field, Phys, Fluids, 4, 1303 (October 1961).

7. Mohler, F. L., J. Research NBS, 19, 447, 559 (1937).

DISTRIBUTION

Addressee	No. of Copies
AFBSD, Attn: BSYDF, Lt. K. Jefferson	2
AFBSD, Attn: BSTRA	1
AFBSD, Attn: BSRA, Capt. Lauritsen	1
AFSSD	
AF Unit Post Office	
Los Angeles, California	
Attn: Capt. Lewis, SSTRE	1
Aerospace Corporation	
San Bernardino, California	
Attn: H. Claflin	29
ARPA	
Washington, 25, D.C.	
Attn: Lt. Col. McNamee	1
ARPA	
Washington, 25, D.C.	
Attn: C. E. McLain	1
ASD	
Wright-Patterson AFB, Ohio	
Attn: D. L. Schmidt, ASRNC-2	1
AFCRL	
L. G. Hanscom Field	
Bedford, Massachusetts	
Attn: N. W. Rosenberg, CRZAC	1
SAC (DORQ)	
Offutt AFB, Nebraska	1
AEDC (AES)	
Tullahoma, Tennessee	1
AMC (ORDAB-HT)	
Redstone Arsenal	
Huntsville, Alabama	
ATIC (AFCIN-4BLA)	1
Wright-Patterson AFB, Ohio	1
AUL	
Maxwell AFB, Alabama	1
Chief, DASA	
Washington, 25, D. C.	1
NASA, Ames Research Center	
Moffett Field, California	1
NASA, Lewis Research Center	
Cleveland, Ohio	1

Addressee	No. of Copies
NASA, Langley Research Center Virginia	1

Department of the Navy
  Washington 25, D. C.
  Attn: SP-272
	1

Central Intelligence Agency
  Washington, D. C.
  Attn: OCR-Std
	2

BAMIRAC, University of Michigan
  Ann Arbor, Michigan
  Attn: R. Nichols
	1

Batelle Memorial Institute Columbus, Ohio	1

Bendix Systems Division
  Ann Arbor, Michigan
  Attn: M. Katz
	1

General Applied Science Laboratory Attn: M. Bloom	1

General Electric Company
  3198 Chestnut Street
  Philadelphia, Pennsylvania
	1

Hughes Aircraft Company
  Culver City, California
  Attn: E. Chrisler
	1

Kaman Nuclear
  Garden of the Gods Road
  Colorado Springs, Colorado
  Attn: A. P. Bridges
	1

Lincoln Laboratory, M.I.T.
  Lexington 73, Massachusetts
  Attn: F. McNamara
	1

Los Alamos Scientific Laboratory Los Alamos, New Mexico	1

The RAND Corporation
  Santa Monica, California
  Attn: C. Gazley
	1

UCRL, "A" Division Livermore, California	1

Addressee	No. of Copies
Defense Documentation Center	
Arlington Hall Station	
Arlington 12, Virginia	10
Lincoln Laboratory, M.I.T.	
Lexington, Massachusetts	
Attn: V. A. Nedzel	1
Lincoln Laboratory, M.I.T.	
P.O. Box 4188	
Norton Air Force Base, California	
Attn: J. Vernon	1
Central Files	1
Document Control	5
Research Library	106

DDC-

mined. Electron densities of the order of 10^{12} cm^{-3} and recombination rates of the order of 10^{-8} cm^3 sec^{-1} were measured.

DDC-

Avco Corporation, Research and Advanced
Development Division, Wilmington, Massachusetts.
PLASMA PROPERTIES IN THE PLUME OF SOLID-PRO-
PELLANT MOTORS CONTAINING CsNO$_3$ and KNO$_3$ by
K. Baldwin, J. Eckerman, R. Williamson and R. Buck.
15 July 1963. 124 p. incl. illus. (Technical Memorandum
RAD-TM-63-14) Contract AF04(694)-239.

Unclassified report

Three series of tests were conducted at the Naval Research
Laboratory high-altitude chamber to measure the perfor-
mance of Al:CsNO$_3$ and Al:KNO$_3$ solid-propellant rocket
motors. Motor operating parameters were measured.
The plume was probed with a microwave system to measure
the electron density at an ambient pressure of 1 torr. The
plume electron density profile as a function of radius and
the recombination rate as a function of radius was deter-

1.	Rocket motors -- Propellants
2.	Propellants -- Rocket motors
3.	Rocket motors -- Solid propellants
4.	Rocket motors -- plasma properties
I.	Baldwin, K.
II.	Eckerman, J.
III.	Williamson, R.
IV.	Buck, R.
V.	Avco Research and Advanced Development Division
VI.	Series
VII.	Title